

REPUBLIQUE ALGERIENNE DEMOCRATIQUE ET POPULAIRE

MINISTRE DE L'ENSEIGNEMENT SUPERIEUR ET DE LA RECHERCHE SCIENTIFIQUE

UNIVERSITE M'HAMED BOUGARA-BOUMERDES



Faculté des sciences

Thèse de Doctorat

Présentée par :

LIMAM Saida

Filière : Physique

Spécialité : Sciences des matériaux

**Montage de spectromètres de positron : application à
l'études des matériaux sous irradiation**

(CR39 irradié par particules alpha-exemple d'étude)

Devant le jury composé de :

Mme	TALA-IGHIL ZAIR	Razika	Prof	UMBB	Présidente
Mr	GUITTOUM	Abderrahim	Directeur de recherche	CRNA	Directeur
Mr	AOUAROUNE	Tahar	Prof	UMBB	Co- Directeur
Mr	GUERBOUS	Lakhdar	Directeur de recherche	CRNA	Examineur
Mr	GUERFI	Tarek	Prof	UMBB	Examineur
Mr	HAZEM	Rafik	Prof	UMBB	Examineur

Année Universitaire 2023/2024

PEOPLE'S DEMOCRATIC REPUBLIC OF ALGERIA
MINISTRY OF HIGHER EDUCATION AND SCIENTIFIC RESEARCH

UNIVERSITY M'HAMED BOUGARA-BOUMERDES



Faculty of Sciences
Doctoral Thesis

Presented by

LIMAM Saida

Major : Physics

Option : Materials Sciences

**Positron Annihilation Spectroscopy Mounting :
Application In Irradiated Materials**

Alpha Irradiated CR39-case of study

Thesis committee :

Mme	TALA-IGHIL ZAIR	Razika	Prof	UMBB	Chairman
Mr	GUITTOUM	Abderrahim	Research director	CRNA	Supervisor
Mr	AOUAROUNE	Tahar	Prof	UMBB	Co- supervisor
Mr	GUERBOUS	Lakhdar	Research director	CRNA	Examiner
Mr	GUERFI	Tarek	Prof	UMBB	Examiner
Mr	HAZEM	Rafik	Prof	UMBB	Examiner

*Positron Annihilation Spectroscopy Mounting: Application In Irradiated
Materials*

March 13, 2024

Abstract

Positron Annihilation Spectroscopy (PAS) is a nuclear technique dedicated to the study of the nanoscopic properties of materials as well as the defects induced following irradiation. Several positron techniques exist in research laboratories: measurement of the positron lifetime, positron spectroscopy by Doppler broadening and the positron accelerator. These techniques are complementary and provide different information resulting from the interaction of positrons with the material. In this thesis work, we propose to create two sets of spectroscopic chains. The first chain concerns the positron lifetime measurement spectrometer (PALS : positron annihilation lifetime spectroscopy) using detectors based on fast scintillators. For the second chain, it will be the Doppler broadening spectroscopy (DBS) positron spectrometer based on a Germanium detector. For the second phase of this thesis work, we propose to study, by PALS and DBS, the effect of alpha irradiation on the CR39 polymer. CR39, polyallyldiglycol carbonate, is in the form of an amorphous polymer. In particular, it plays a unique role as a solid-state nuclear track detector (SSNTD). The CR39 stands out for its remarkable ability to effectively capture and preserve charged particles, particularly alpha particles, in the form of latent tracks. The relationship between the tracks formed and the irradiation conditions will be studied. This analysis is of particular importance in the context of alpha particle spectroscopy and dosimetry.

Key words : positron spectroscopy, PALS, DBS, alpha irradiation, CR39

Résumé

La spectroscopie d'annihilation du positron (PAS, Positron Annihilation Spectroscopy) est une technique nucléaire dédiée à l'étude des propriétés nanoscopiques des matériaux ainsi que les défauts induits suite à des irradiations. Plusieurs techniques de positron existent dans les laboratoires de recherches : la mesure du temps de vie du positron, la spectroscopie de positron par élargissement Doppler et l'accélérateur de positron. Ces techniques sont complémentaires et permettent d'avoir des informations différentes qui résultent de l'interaction des positrons avec le matériau. Dans ce travail de thèse, on propose de réaliser deux montages de chaînes spectroscopiques. La première chaîne concerne le spectromètre de mesure du temps de vie du positron (PALS : positron annihilation lifetime spectroscopy) en utilisant des détecteurs à base de scintillateurs rapides. Pour la deuxième chaîne, il s'agira du spectromètre de positron par élargissement Doppler (Doppler broadening spectroscopy, DBS) basé sur un détecteur de Germanium. Pour la suite de ce travail de thèse, on se propose d'étudier, par PALS et DBS, l'effet des irradiations alpha sur le polymère CR39. Le CR39, carbonate de polyallyldiglycol, se présente sous la forme d'un polymère amorphe. Il joue notamment un rôle unique en tant que détecteur de traces nucléaires à l'état solide (SSNTD). Le CR39 se distingue par sa remarquable capacité à capturer et préserver efficacement les particules chargées, notamment les particules alpha, sous forme de traces latentes. La relation entre les traces formés et les conditions d'irradiations sera étudiée. Cette analyse revêt une importance particulière dans le contexte de la spectroscopie et de la dosimétrie des particules alpha.

Mots clés : spectroscopie de positron, PALS, DBS, irradiation alpha, CR39

الملخص

التحليل الطيفي للإبادة البوزيترونية (PAS) هو تقنية نووية مخصصة لدراسة الخواص النانوية للمواد بالإضافة إلى العيوب الناجمة عن التشعيع. توجد العديد من تقنيات البوزيترون في مختبرات الأبحاث: قياس عمر البوزيترون، التحليل الطيفي البوزيتروني عن طريق توسيع دوبلر ومسرّع البوزيترون. هذه التقنيات متكاملة وتوفر معلومات مختلفة ناتجة عن تفاعل البوزيترونات مع المادة. في هذه الأطروحة، نقترح إنشاء مجموعتين من السلاسل الطيفية. تتعلق السلسلة الأولى بمطياف قياس عمر البوزيترون (PALS): التحليل الطيفي لمدى عمر إبادة البوزيترون) باستخدام كاشفات تعتمد على وميض سريع. بالنسبة للسلسلة الثانية، سيكون مطياف البوزيترون الموسع دوبلر (DBS) يعتمد على كاشف الجرمانيوم. بالنسبة للمرحلة الثانية من هذه الأطروحة، نقترح دراسة تأثير تشعيع ألفا على البوليمر CR39، بواسطة PALS و DBS و CR39، بولي أليل ديجليكول كربونات، موجود في شكل بوليمر غير متبلور. على وجه الخصوص، فإنه يلعب دورًا فريدًا باعتباره كاشف المسار النووي للحالة الصلبة (SSNTD). يتميز CR39 بقدرته الرائعة على التقاط الجسيمات المشحونة والحفاظ عليها بشكل فعال، وخاصة جسيمات ألفا، في شكل مسارات كامنة. سيتم دراسة العلاقة بين المسارات المتكونة وظروف التشعيع. ولهذا التحليل أهمية خاصة في سياق التحليل الطيفي لجسيمات ألفا وقياس الجرعات.

Dedication

الى قمر ازمانى ونور ظلماتى الى سيدى محمد صلى الله عليه وسلم

Acknowledgements

First of all I offer my deepest thanks to God, "Praise be to God"

This thesis would not have been possible without the invaluable resources, facilities, and technical support of the Nuclear Research Center of Algiers (CRNA). I wish to extend my gratitude to the Nuclear Research Center of Algiers for providing me with the opportunity to carry out this research. I am deeply grateful to the entire staff of CRNA, particularly the researchers and engineers of the Department of Physics, for their encouragement, guidance, and technical assistance.

I would like to thank my thesis supervisor Dr. GUITTOUM Abderrahim, Research Director at CRNA, for supervising and proposing such an interesting and challenging topic, as well as his availability despite his many responsibilities, which reflects his scientific competence and rigor. I would also like to express my appreciation to the members of my thesis committee; I thank Mme. TALA-IGHIL ZAIR Razika, professor at the University of Boumerdes, for honoring me by presiding over the jury of this thesis. I would like to express my gratitude to Mr. Guerfi Tarek , professor at the University of Boumerdes and Mr. Hazem Rafik, professor at the University of Boumerdes, and Mr. Guerbous Lakhdar, Research Director at CRNA, for agreeing to examine this modest work.

I express my sincere gratitude to Mme Mokrani for sharing her important knowledge about the fundamentals of latent tracks.

A special thanks goes to Mr. Bendjeddah for dedicating extensive time to guide us in mastering the techniques. His unwavering patience and honesty in sharing the intricacies of the techniques have been truly appreciated. Thank you, Mr. Bendjeddah, for your exceptional contribution.

I extend my appreciation to Mr. Izzerouken Mahmoud for his significant efforts in conducting irradiation experiments on our samples. His generous investment of time and kind attitude

towards our team are commendable. We wish him continued success, safety, and hope for future collaborations.

Heartfelt thanks to our collaborator from Turkey, Mr. U. Yashi, for his interesting work, especially in providing the VEDBS system.

I also want to express my gratitude to Mr. Hemous, Mr. Ait Ziane, and Mme. Mezzaguer for their comments, kindness, and friendship throughout this journey.

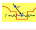
Each of you has played an integral role in the success of this project, and I am truly grateful for your contributions and support.

I am immensely grateful for the unwavering support and love of my parents. Their encouragement and belief in me have been the pillars of my journey, and I am profoundly thankful for the sacrifices they have made to help me reach this point.

To my brothers , sisters and friends(..... a lot of them...) your camaraderie and understanding have brought joy and warmth to my life. Thank you for standing by me through thick and thin, for your encouragement, and for being an integral part of my support system.

I am blessed to have such a loving and supportive family, and I cherish the moments we've shared together. Your presence has made my achievements all the more meaningful. I love you all deeply and appreciate everything you've done for me

Contents

1	<i>The Theory of Positron Annihilation Spectroscopy(PAS)</i>	20
1.1	The first principles foundation of PAS technique	20
1.1.1	Dirac Equation	20
1.1.2	Positron and Positronium's discovery	29
1.1.3	Positron's role as a solid-state property monitor: proof	31
1.2	Positron-Condensed Matter Interaction	33
1.2.1	Thermalization	33
1.2.2	Diffusion	37
1.2.3	Backscattering	38
1.2.4	Positron States	40
1.2.5	Positron-electron Momentum Density :	45
1.2.6	Annihilation Rate:	46
2	PAS Techniques	49
2.1	Technical Instruments	50
2.1.1	Positron Sources	50
2.1.2	Gamma Detectors	52
2.1.3	Nuclear Instruments Modulus(NIM)	64
2.2	Positron Annihilation Spectroscopy Methods	67
2.2.1	Positron Annihilation Lifetime Spectroscopy (PALS) 	67
2.2.2	Doppler Broadening Spectroscopy (DBS)	71
2.2.3	Variational Energy Positron Annihilation Spectroscopy (VEPAS)	73
3	The Solid State Nuclear Track Detector of CR39-Art state	83
3.1	What is CR39 ?	83

3.2	The Nuclear Tracks	86
3.3	Nuclear tracks characterizing techniques	92
3.3.1	Latents tracks characterisation	92
3.3.2	Etching process	98
3.3.3	Etched tracks characterisation	99
4	Results and Discussion	103
4.1	PALS Experiments	104
4.1.1	Heigh Voltage optimization:	105
4.1.2	Energy Selection :	106
4.1.3	Setting-up the spectrometer :	110
4.2	PALS-setup with BC418+Burle 8850	113
4.2.1	Heigh Voltage optimization	113
4.2.2	Energy Selection and Spectrometer Calibration:	114
4.3	PALS-setup with (EJ228+H3378-51).	117
4.3.1	Heigh Voltage optimisation :	117
4.3.2	Energy Selection and Spectrometer Calibration	118
4.4	CR39 irradiation :	120
4.4.1	The series of different Flunce $CR39(\neq \Phi)$:	121
4.4.2	The series of different Energy $CR39(\neq E)$:	121
4.4.3	The series of different Energy $CR39(\neq E^*)$:	122
4.4.4	Induced-Alpha damages in CR39	123
4.4.5	Implantion profile of energetic positron in CR39	126
4.5	Characterization of $CR39(\neq E)$ series using EJ228 detector based PALS set-up.	127
4.5.1	Measurements and results discussion	127
4.6	Characterization of $CR39(\neq \Phi)$ series using (BC418+Burle885) detector based	
	PALS-setup	129
4.6.1	Measurements and results discussion	129
4.6.2	Comparison between the F_V derived from PALS and a computed F'_V	
	using the Waligorski Calculation method :	134
4.7	DBS Experiments :	135
4.7.1	DBS set-up and calibration	135

4.8 DBS Characterization of $CR39(\neq E)$	137
4.9 DBS Characterization of $CR39(\neq \Phi)$	140
4.10 Etched $CR39(\neq \Phi)$ characterization by (BC418+Burle885) detector based PALS-	
setup and DBS :	141
4.10.1 Etching experiment :	141
4.10.2 Effects of Etching in S, W parameters and positronium lifetime/free vol-	
ume radius	142
4.11 $CR39(\neq E^*)$ series characterization by VEDBS	145
4.11.1 Beam positron depth in CR39	145
4.11.2 VEDBS set-up :	146
4.11.3 Measurements and discussion	147
4.12 Positron Lifetime calculation using DFT	149

List of Figures

1.1.1 The discovery of Positron [1]	29
1.2.1 Energetic positron implantation profile in Silicon	35
1.2.2 mono-energetic positron beam implantation profile in Silicon [2]	37
2.1.1 Sodium ^{22}Na Decay Shem [3]	51
2.1.2 Radioactive source + Micropipette	52
2.1.3 The spectral response of Bialkali photocathode	56
2.1.4 Cross section of PMT	56
2.1.5 Photocathode type and mode light transportation	57
2.1.6 BURLE 8850	58
2.1.7 H3378-51 PMT	59
2.1.8 Typical Anode Output with a Burle 8850 PMT	60
2.1.9 The composed detector of BC418+Burle8850+265A Base	61
2.1.10 The composed detector of EJ228+H3378-51+265A Base	61
2.1.11 Ge principle of detection [4]	63
2.1.12 Configuration of GEM Coaxial Germanium Crystal	63
2.1.13 HPGe detector	64
2.1.14 Liquid Nitrogen Cryosta	64
2.1.15 CFDD Model 583B	65
2.1.16 CFDD principle	65
2.1.17 CFDD output signal	66
2.1.18 FAC/SCA 567	66
2.2.1 PALS basic principal	68
2.2.2 PALS devices	68
2.2.3 Detecting system	69

2.2.4 Electronic system	69
2.2.5 DBS spectrometer	72
2.2.6 S and W parameters	73
2.2.7 Tungsten work function	74
2.2.8 Monoenergetic positron re-emission probability for soild Neon [5]	75
2.2.9 The positron accelerator of Marmara University	76
2.2.10 Positron Moderator System	78
2.2.11 Energy Distribution of positron from the moderator. Narrow Energy Spread:	
1.7 eV (FWHM)	78
2.2.12 Long moderator lifetime: 4% per day decay	79
2.2.13 Overview of the TS-1	80
2.2.14 Close up of the load lock, showing the demountable sample holder	80
2.2.15 Close-up of the high voltage feedthrough	81
3.1.1 First Tracks observation [6]	84
3.1.2 CR39 monomer	86
3.2.1 The atomic nature of a particle track in (a) a crystal and (b) a polymer [7]	87
3.3.1 Free volume holes [8]	94
3.3.2 Methods for Characterization and Their Resolutions [9]	95
3.3.3 Ortho-Ps annihilation in the crystalline and amorphous phases of polymers. Lo-	
cal freevolume sizes typically range from 0.5 nm. [10]	96
3.3.4 Free volumes growth under irradiations	98
3.3.5 The track's development's geometry (V_t is constant) [11]	100
4.1.1 Bias Voltage Generator	105
4.1.2 Bias voltage optimization circuit	106
4.1.3 The energy selection assembly using the oscilloscope (START detector)	107
4.1.4 The energy selection assembly using the oscilloscope (STOP detector)	109
4.1.5 SCA-COUNTER circuit	109
4.1.6 Energetic spectrum of START and STOP detectors	110
4.1.7 PALS set-up	110
4.1.8 Evolution of channel in time, T_0	112
4.2.1 Energy spectra for the START detector	113

4.2.2 Energy spectra for the STOP detector	113
4.2.3 Detection geometry	114
4.2.4 Silicon PALS spectrum	115
4.2.5 The fit of unirradiated Si spectrum	115
4.2.6 The best selection energy spectra of BC418	116
4.2.7 The fit of the last selection	117
4.3.1 Energetic spectra for Start Detector	118
4.3.2 Energetic Spectra of Stop Detector	118
4.3.3 Energy spectra of start and stop detectors(EJ228)	120
4.4.1 Unirradiated CR39	120
4.4.2 Irradiation procedure	121
4.4.3 ^{22}Na radioactive source + ^{241}Am source+CR39 samples	122
4.4.4 The fluence variation of alpha particles as a function of irradiation distance	122
4.4.5 Vacuum chamber+ Irradiation set-up of the third series CR39($\neq E^*$)	123
4.4.6 Bragg Curve and Alpha Energy Versus Range	124
4.4.7 TRIM simulation plots for $E_\alpha = 4.5MeV$	125
4.4.8 3D plot of alpha range distribution for $E = 4.1MeV$	125
4.4.9 Radial Dose Distribution Versus Radial Distance	126
4.4.10 Positron depth in CR39	126
4.5.1 Sample preparation	127
4.5.2 PALS of unirradiated CR39	128
4.5.3 PALS spectra of irradiated CR39 with different alpha energies	128
4.5.4 The variation of lifetime of $o - Ps$ as a function of alpha energy	129
4.6.1 Lifetime of unirradiated CR39	130
4.6.2 Lifetime Spectra of CR39 samples	131
4.6.3 Free Volume Radius Distribution	133
4.6.4 Variation of τ_3 and free volume radius, r_h Versus Fluence	133
4.7.1 DBS set-up	136
4.7.2 Spectrum of DBS calibration	136
4.7.3 DBS(Si) spectrum	137
4.8.1 DBS spectra of irradiated CR39	138

4.8.2 DBS(CR39) spectra supposition	139
4.8.3 The S parameter variation curve as a function of alpha particle energy	139
4.9.1 Variation of the S and W parameters Versus the Fluence	140
4.10. Etching experiment	142
4.10.2 Variation of τ_3 Versus Fluence for etched and no-etched samples	143
4.10.3 Variation of free volume-radius versus fluence for etched and no-etched samples	143
4.10.4 Variation of S-parameter Versus fluence for etched and no-etched Samples	144
4.10.5 Variation of W-parameter Versus fluence for etched and no-etched Samples	144
4.10.6 Etched samples under optical microscopy	145
4.11. The variation of the mean depth of slow positrons as a function of their energy	146
4.11.2 variation of VEDBS(Si) spectra Vs positron beam energies	147
4.11.3 variation of VEDBS (CR39) spectra Vs positron beam energies	148

List of Tables

2.1 BC418 and EJ228 scintillators characteristics	54
2.2 PMT specifications	59
3.1 Mulliken atomic charges	85
3.2 Electronic properties of the CR39	85
4.1 Calcul of T_0	112
4.2 The flux and the fluences of the second serie	122
4.3 o-Ps lifetimes and their intensity evolution	129
4.4 Positron annihilation lifetime data for alpha irradiated CR39	132
4.5 F_V the fraction of free volumes for irradiated samples. rF_V the total free volumes radius. F'_V the new calculated free volumes fraction	135
4.6 Regularities parameters	136

General Introduction

The history of positron annihilation spectroscopy's development from basic physics to major industrial applications is an ancient tale of scientific advancement. Positron was first predicted by Dirac in 1928 and then confirmed by Anderson in 1932. In the same decade, Joliot-Curie showed that positrons may be released from artificially created isotopes. But the field didn't see a revival because of the enjoining world events until the 1960s, when more accessible equipment became available. Both angular correlation spectroscopies and positron annihilation lifetime spectroscopy (PALS) saw a considerable boost in sophistication and activity during this time.

Nowadays, Positron Annihilation Spectroscopy techniques(PAS) including : Positron Annihilation Lifetime Spectroscopy (PALS), Doppler Broadening Spectroscopy (DBS) and Variational Energy Doppler Broadening Spectroscopy(VEEDBS) are continuously being developed and are close to becoming a routine analytical tool for polymer characterization. Scientific investigation has demonstrated its durability and flexibility over time, as evidenced by the phenomenal evolution of these approaches from early theoretical predictions and discoveries to their current state of improvement.

Positron Annihilation Lifetime Spectroscopy(PALS) method stands as one of the most advanced techniques for the microstructural characterization of disordered materials. It provides valuable insights into the dimensions and time scales properties aimed at characterizing free-volume voids. Moreover, Doppler Broadening Spectroscopy could be used to comprehend the chemical structure via the quantification of the momentum density. Using Variation Energy Positron Annihilation Spectroscopy(VEPAS), different positron energies could be manipulated which allow the characterization of thin films. In the 1980s a renaissance in PAS applications in the field of polymers was connected with the accessibility of characterized polymer materials as well as with methodological progress which consisted of raw data evaluation and subsequent interpretation allowing free-volume data quantification and its physical explanation.

In the scope of this thesis project, we intend to establish two distinct spectroscopic chains. The first chain is Positron Annihilation Lifetime Spectroscopy (PALS). This particular setup employs detectors that rely on fast scintillators to capture relevant data. Concurrently, the second spectroscopic chain involves a Doppler Broadening Spectroscopy (DBS) positron spectrometer equipped with a Germanium detector. In the subsequent phases of the thesis, we will employ both PALS and DBS techniques to investigate the impact of alpha irradiation on CR39 polymer. CR39 is an amorphous polymer. Notably, it serves a unique role as a solid-state nuclear track detector (SSNTD). CR39 is distinguished by its remarkable capability to effectively capture and preserve charged particles, notably alpha particles.

Once heavy charged particles like alpha interactes with CR39 chains, the formation of nuclear tracks along the particle trajectories will take a place. The nuclear tracks could be : latent tracks which is angstrom-sized. It is formed by initial irradiation on untreated CR39. The second type of tacks is the birth tracks which is visible after a brief etching in order of some micrometer. Revealed tracks is the last type. It could be seen after an extensive etching. The PAS technique is classified as a unique nuclear probe technique to investigate the growth of free volumes. It is very useful to quantify latent tracks by evaluating free volumes, as this offers a way to characterize the CR39. Our goal is to comprehend the impact of radiation and structural alterations in CR39 through an analysis of the free volume evolution following alpha-particle irradiation.

The central theme of the thesis is the pursuit of optimal conditions to achieve the best resolution for polymer characterization. In the realm of Positron Annihilation Lifetime Spectroscopy (PALS), a key focus lies on time resolution and counts rate. In the context of Doppler Broadening Spectroscopy (DBS), the emphasis shifts to fine-tuning electronic settings. Over a span of three years, an extensive array of parameters, including energy selection and spectrometer calibration, underwent rigorous verification. The successful analysis of samples is contingent upon meticulous resolution time calibration, highlighting the critical role this parameter plays in achieving accurate and meaningful results in irradiated-CR39 characterization.

In *Chapter 1*, we embark on a journey by revisiting the foundational scientific principles that gave rise to the theory behind the technique. Commencing with the Dirac equation, a meticulous point-by-point calculation unfolds, unraveling the theoretical genesis of the *A. P. Dirac* long before the experimental validation of positron existence. This serves as a foundational

chapter, establishing the theoretical consciousness that laid the groundwork for the subsequent evolution of the technique. The discovery of the positron by Carl Anderson is detailed, providing a firsthand account of the pivotal moment in the development of positron theory. Following this historical exploration, we delve into an elucidation of the reason that render this theoretical framework advantageous in the realm of solid-state characterization. The chapter articulates how insights from Debenedetti can contribute to enhancing our understanding of condensed matter. Subsequently, the current state of positron-condensed matter interaction theory has been studied. This encompasses an examination of various phenomena, thermalization, diffusion, and backscattering phenomena. The exposition then proceeds to showcase a simulation approach designed to calculate the rate of positron annihilation in bulk materials or within defects, with a specific focus on the Positronium state (Ps). The study of positron-matter interactions is presented in detail, as are the simulation methods used to simulate positron states in both bulk materials and amorphous one is illustrated. This provides a comprehensive summary of the current theoretical art state of positron-condensed matter interactions.

In *Chapter 2*, we delve into an up-to-date and critical review of Positron Annihilation Spectroscopy (PAS) physics, encompassing the use of both fast and slow positron beams. In order to present a comprehensive understanding of the apparatus and methodology, the chapter was divided into two sections. The first section was intended to describe each component belonging to the positron spectrometer setup and the second section was for the PAS methods, including : PALS, DBS and VEDBS. This chapter has intentionally attempted to presume a significant level of familiarity with the technical ideas related to PAS and how they might be used in laboratory. By doing this, we hope to give a thorough grasp of PAS's fundamental principles as well as its practical applications.

In *Chapter 3*, the characterization of CR39 is thoroughly investigated, primarily focusing on the details of its free volumes. To begin, let us define the CR39 as a solid-state nuclear track detector and explain why it was made. Next, we provide an in-depth analysis of nuclear tracks, concentrating on the delta ray theory, which is the most suitable to represent nuclear tracks in polymer cases. Afterwards, etched tracks and latent tracks will be thoroughly examined, with a focus on classifying and understanding these distinct kinds of tracks. This chapter provides a thorough overview of several methods for characterizing nuclear tracks. Remarkably, the positron annihilation technique appears to be the only one that may directly provide tiny hole

parameters, usually on a few Angstrom scale. Acknowledging its importance, we provide a brief overview of the state of the art on Positron Annihilation Spectroscopy (PAS) as it relates to free volume research. This includes a study of how PAS is an effective instrument for deciphering and examining the microscopic features of these tracks, which advances our knowledge of the properties and behavior of materials in general. It has been made obvious how defining nuclear tracks using latent tracks—that is, the evolution of free volumes in this case—differs from characterizing nuclear tracks utilizing etched track monitoring with methods like MEB or OM. The main goal is to establish a relationship between the variations in free volumes and the positron annihilation lifetime. This knowledge assumes utmost significance, especially in the domains of dosimetry and alpha-particle spectroscopy. In order to improve the accuracy and usefulness of methods in alpha-particle spectroscopy and dosimetry, the chapter will examine and comprehend the connection between positron annihilation lifetime and dynamic changes in free volumes. This effort advances our knowledge of how positron interactions and material properties interact in these particular situations.

In *Chapter 4*, a thorough investigation is conducted where we examine the essential experiments conducted to determine the ideal conditions for reaching the best resolution required to characterize polymers. Every interesting experiment is thoroughly explained, giving a detailed description of the procedures used. Specifically, confirming the optimal time resolution in the context of Positron Annihilation Lifetime Spectroscopy (PALS) technology is an important achievement. Essential variables like counts rate and temporal resolution are prioritized in every experiment since they are critical metrics for assessing the spectrometer's performance. In particular, investigations for the DBS set-up are planned to calibrate energy until the silicon energetic spectrum's S parameter reaches 0.5, a demonstration that highlights the set-up's precision. Moreover, a detailed explanation and demonstration of the VEDBS system's setup are provided. Following a thorough demonstration and discussion of the irradiation procedures used on three sets of CR39 samples with alpha particles, the investigation then shifts to the analysis of alpha-irradiated CR39. This methodical approach lays the foundation for a complete analysis of the results acquired by ensuring a solid and full comprehension of the experimental techniques and setup details.

In plus, we have developed a Python script that use the Density Functional Theory (DFT) to compute the lifetime of ortho-positronium (o-Ps) in unirradiated CR39. Python is used

to enable a flexible and comprehensible implementation, demonstrating the usefulness of theoretical physics and contemporary programming methods in addressing challenging scientific problems.

Chapter 1

The Theory of Positron Annihilation Spectroscopy(PAS)

Introduction

In the present chapter titled with the theory of positron annihilation spectroscopy, the following contents will be included all in respecting the chronological order of the development of positron spectroscopy theory. In the first Sec."1.1" we review the calculation of the Dirac equation. Then, we represent the experience on how the positron had been discovered in the first time on laboratory by Carl Anderson. After that, we respond to the first question getting in mind to each experimentalist: Why this technique and how it will be investigated? in the Subsec"1.1.3". The interaction of positron with solids is the subject of the Sec."1.2" where the description of positron-condensed matter interaction including the process : thermalization, diffusion, backscattering, annihilation will be assumed.

1.1 The first principal foundation of PAS technique

1.1.1 Dirac Equation

Schrödinger has established the equation holding his name which describes the behavior of a quantum particle existed therein an external potential, V [12]:

$$i\hbar \frac{\partial \psi}{\partial t} = \mathcal{H}\psi \quad (1.1.1)$$

That equation was built on non-relativistic assumptions at a time when the theory of relativity had been extensively proved, prompting the theoretical community to seek another formulation that would better match the experimental data while also highlighting the relativistic nature of the particles. In fact, at that time, the inherent property of spin had not yet been dis-

covered. Following that, theoretical physicists attempt to model the spin phenomenon using the Schrodinger equation. We shall discuss Klein Gordan's contribution before re-establishing the Dirac equation.

We know that, the energy of a particle at rest is :

$$E = mc^2 \quad (1.1.2)$$

and in motion,

$$E = \frac{mc^2}{\sqrt{1 - \frac{v^2}{c^2}}} \quad (1.1.3)$$

The momentum written as :

$$p = \frac{mv}{\sqrt{1 - \frac{v^2}{c^2}}} \quad (1.1.4)$$

So the energy formula could be expressed in terms of momentum as

$$E = \sqrt{(pc)^2 + (mc^2)^2} \quad (1.1.5)$$

For a photon, $m = 0$

$$E = pc = h\nu \quad (1.1.6)$$

Quantum mechanically, the energy and momentum operators expressed as :

$$\hat{E} = i\hbar\partial_t \quad (1.1.7)$$

$$\hat{p}_j = i\hbar\partial_j \quad (1.1.8)$$

If we would like representing the intrinsic property of spin, we assume their description by spin operators \hat{S}_x , \hat{S}_y and \hat{S}_z . Here is the Dirac ket $|\uparrow\rangle$, $|\downarrow\rangle$ where the application of spin operators gives,

$$\hat{S}_z |\uparrow\rangle = \frac{\hbar}{2} |\uparrow\rangle \quad (1.1.9)$$

$$\hat{S}_z |\downarrow\rangle = -\frac{\hbar}{2} |\downarrow\rangle \quad (1.1.10)$$

In fact, the dirac representation is an abstract configuration equivalent to the following vector states :

$$|\uparrow\rangle = \begin{pmatrix} 1 \\ 0 \end{pmatrix} \quad (1.1.11)$$

$$|\downarrow\rangle = \begin{pmatrix} 0 \\ 1 \end{pmatrix} \quad (1.1.12)$$

which translate the probability amplitude of spin to be up or down, $\pm\frac{\hbar}{2}$. According to the formula 1.1.111.1.12 they think to build a matrix representation of \hat{S} operator using the property

$$\begin{bmatrix} A & B \\ C & D \end{bmatrix} \begin{bmatrix} U \\ V \end{bmatrix} = \begin{bmatrix} AU + BV \\ CU + DV \end{bmatrix} \quad (1.1.13)$$

Since

$$\begin{bmatrix} A & B \\ C & D \end{bmatrix} \begin{bmatrix} 1 \\ 0 \end{bmatrix} = \begin{bmatrix} A \\ C \end{bmatrix} = \frac{\hbar}{2} \begin{bmatrix} 1 \\ 0 \end{bmatrix} \quad (1.1.14)$$

$$\begin{bmatrix} A & B \\ C & D \end{bmatrix} \begin{bmatrix} 0 \\ 1 \end{bmatrix} = \begin{bmatrix} B \\ D \end{bmatrix} = -\frac{\hbar}{2} \begin{bmatrix} 0 \\ 1 \end{bmatrix} \quad (1.1.15)$$

We find that \hat{S}_z written as,

$$\hat{S}_z = \frac{\hbar}{2} \begin{bmatrix} 1 & 0 \\ 0 & -1 \end{bmatrix} \quad (1.1.16)$$

using the commutations relationships between the components of spin operators \hat{S}_x , \hat{S}_y and \hat{S}_z

$$[\hat{S}_i, \hat{S}_j] = i\hbar\hat{S}_{\delta(i,j,k)} \quad (1.1.17)$$

The construction of those operators matrices achieved taking the following building :

$$\hat{S}_x = \frac{\hbar}{2} \begin{bmatrix} 0 & 1 \\ 1 & 0 \end{bmatrix} \quad (1.1.18)$$

$$\hat{S}_y = \frac{\hbar}{2} \begin{bmatrix} 0 & -i \\ i & 0 \end{bmatrix} \quad (1.1.19)$$

They are proportional by $\hbar/2$ factor with matrices called the Pauli matrices which are looking like

$$\hat{\sigma}_z = \begin{bmatrix} 1 & 0 \\ 0 & -1 \end{bmatrix} \quad (1.1.20)$$

$$\hat{\sigma}_x = \begin{bmatrix} 0 & 1 \\ 1 & 0 \end{bmatrix} \quad (1.1.21)$$

$$\hat{\sigma}_y = \begin{bmatrix} 0 & -i \\ i & 0 \end{bmatrix} \quad (1.1.22)$$

Therefore, the idea to develop an electron wavefunction with spin came from in which the new state being as the multiplication of space-time like state with spin state as follows :

$$|\psi_1\rangle = \psi_1(x, y, z, t) |\uparrow\rangle \iff \begin{bmatrix} \psi_1(x, y, z, t) \\ 0 \end{bmatrix} \quad (1.1.23)$$

$$|\psi_2\rangle = \psi_2(x, y, z, t) |\downarrow\rangle \iff \begin{bmatrix} 0 \\ \psi_2(x, y, z, t) \end{bmatrix} \quad (1.1.24)$$

A unified state that govern the spectrum amplitudes in this case should be take the expression

$$|\psi\rangle = \begin{bmatrix} \psi_1(x, y, z, t) \\ 0 \\ 0 \\ \psi_2(x, y, z, t) \end{bmatrix} \quad (1.1.25)$$

which called “*SPINOR*”, we note here that : $|\psi_1|^2 dV$: is the probability of electron at some point with spin up similarly about $|\psi_2|^2 dV$, representing the probability of electron at some point with spin down, noting :

$$\langle\psi|\psi\rangle = \int (|\psi_1|^2 + |\psi_2|^2) dV = 1 \quad (1.1.26)$$

Then, attending to construct a relativistic wavefunction, they apply the relativistic energy operator to that spinor; (for a free electron)

$$i\hbar\partial_t\psi = \left[\sqrt{-(\hbar c)^2\nabla^2 + (mc^2)^2} \right] \psi \quad (1.1.27)$$

$$\nabla^2 = \partial_x^2 + \partial_y^2 + \partial_z^2 \quad (1.1.28)$$

To solve the above equation, we square the both sides to get ;

$$-\hbar^2\partial_t^2\psi = -\hbar^2c^2\nabla^2\psi + m^2c^4\psi \quad (1.1.29)$$

This is what we called “*Klein Gordan*” equation, but we have some problems underling as following

■The energy by itself is positive or negative,

$$E = \pm\sqrt{(pc)^2 + (mc^2)^2} \quad (1.1.30)$$

Because we start by square it firstly where for every solution with positive energy there is a another with $E < 0$ which seems unphysical!

■That equation gives us $\partial_t^2\psi$ whereas we need both ψ and $\partial_t\psi$ towards the specifying of a system state.

■ Predicts incorrect energy levels of hydrogen atoms

■ Does not require or predict the spin of electron . Thereafter, Dirac [13] suggest to express the term of energy with four terms as :

$$\sqrt{p^2 + m^2} = \alpha_x p_x + \alpha_y p_y + \alpha_z p_z + \beta m \quad (1.1.31)$$

$$E^2 = p^2 + m^2 = (\alpha_x p_x + \alpha_y p_y + \alpha_z p_z + \beta m)(\alpha_x p_x + \alpha_y p_y + \alpha_z p_z + \beta m) \quad (1.1.32)$$

$$= \alpha_x^2 p_x^2 + \alpha_y^2 p_y^2 + \alpha_z^2 p_z^2 + \beta^2 m^2$$

$$+ \alpha_x \alpha_y p_x p_y + \alpha_x \alpha_z p_x p_z + \alpha_x p_x \beta m$$

$$+ \alpha_y \alpha_x p_y p_x + \alpha_y \alpha_z p_y p_z + \alpha_y p_y \beta m$$

$$+ \alpha_z \alpha_x p_z p_x + \alpha_z \alpha_y p_z p_y + \alpha_z p_z \beta m$$

$$+ \beta m \alpha_x p_x + \beta m \alpha_y p_y + \beta m \alpha_z p_z$$

$$= \alpha_x^2 p_x^2 + \alpha_y^2 p_y^2 + \alpha_z^2 p_z^2 + \beta^2 m^2 + 0$$

$$= p_x^2 + p_y^2 + p_z^2 + m^2$$

According to the equivalence must be :

$$\alpha_x^2 = \alpha_y^2 = \alpha_z^2 = \beta^2 = 1 \quad (1.1.33)$$

And the later twelve terms goes by zero. Nevertheless, the commutators of component momentum operators carries that :

$$\alpha_x \alpha_y p_x p_y + \alpha_y \alpha_x p_y p_x = 0 \Rightarrow (\alpha_x \alpha_y + \alpha_y \alpha_x) [p_x, p_y] = 0 \quad (1.1.34)$$

Because : $[p_x, p_y] = 0$ that lead to

$$\alpha_x \alpha_y = -\alpha_y \alpha_x$$

To have a solution, it nessesite that α_x or $\alpha_y = 0$ but, $\alpha_x^2 = \alpha_y^2 = 1$. Dirac solution was to configure α by matrices which Pauli matrices satisfies such relationships

$$\sigma_x \sigma_y = -\sigma_y \sigma_x \quad (1.1.35)$$

$$\sigma_x \sigma_z = -\sigma_z \sigma_x \quad (1.1.36)$$

$$\sigma_y \sigma_z = -\sigma_z \sigma_y \quad (1.1.37)$$

$$\sigma_x^2 = \sigma_y^2 = \sigma_z^2 = 1_U \quad (1.1.38)$$

We note from there that the above equation predicts the spin explicitly, where it is clear that the spin operator is an intrinsic requirement of a relativistic theorem of the electron. For a technical reason , the equation needs a matrices($4 \otimes 4$) to get a solution $\alpha_x, \alpha_y, \alpha_z$ and β they constructed according to Pauli matrices as :

$$\alpha_x = \begin{bmatrix} 0 & 0 & 0 & 1 \\ 0 & 0 & 1 & 0 \\ 0 & 1 & 0 & 0 \\ 1 & 0 & 0 & 0 \end{bmatrix}, \alpha_y = \begin{bmatrix} 0 & 0 & 0 & -i \\ 0 & 0 & i & 0 \\ 0 & -i & 0 & 0 \\ i & 0 & 0 & 0 \end{bmatrix}, \alpha_z = \begin{bmatrix} 0 & 0 & 1 & 0 \\ 0 & 0 & 0 & -1 \\ 1 & 0 & 0 & 0 \\ 0 & -1 & 0 & 0 \end{bmatrix} \text{ and } \beta = \begin{bmatrix} 1 & 0 & 0 & 0 \\ 0 & 1 & 0 & 0 \\ 0 & 0 & -1 & 0 \\ 0 & 0 & 0 & -1 \end{bmatrix}$$

The thing that allows us to write the energy formula as,

$$E = \alpha_x p_x + \alpha_y p_y + \alpha_z p_z + \beta m \quad (1.1.39)$$

Then the Dirac equation for a free electron will be :

$$i\partial_t \psi = -i\alpha_x \partial_x \psi - i\alpha_y \partial_y \psi - i\alpha_z \partial_z \psi + m\beta \psi \quad (1.1.40)$$

which is equivalent to :

$$i\partial_t \psi = -i\vec{\alpha} \cdot \vec{\nabla} \psi + m\beta \psi \quad (1.1.41)$$

As a result, Dirac's equation describes the space time evolution of 4th component particle wavefunction which contains both the quantum properties and predicts the motion of electron at any speed. Analyse the above equation, meaning to show all component, we will have :

$$i\partial_t \psi_1 = -i\partial_x \psi_4 - \partial_y \psi_4 - i\partial_z \psi_3 + m\psi_1 \quad (1.1.42)$$

$$i\partial_t \psi_2 = -i\partial_x \psi_3 + \partial_y \psi_3 + i\partial_z \psi_4 + m\psi_2 \quad (1.1.43)$$

$$i\partial_t \psi_3 = -i\partial_x \psi_2 - \partial_y \psi_2 - i\partial_z \psi_1 - m\psi_3 \quad (1.1.44)$$

$$i\partial_t \psi_4 = -i\partial_x \psi_1 + \partial_y \psi_1 + i\partial_z \psi_2 - m\psi_4 \quad (1.1.45)$$

If we would search about an electron at rest ($p = 0$), then the terms with cross between x, y and

z component goes to zero because it is momentum terms. Hence, we will have the following collection :

$$i\partial_t\psi_1 = m\psi_1 \tag{1.1.46}$$

$$i\partial_t\psi_2 = m\psi_2 \tag{1.1.47}$$

$$i\partial_t\psi_3 = -m\psi_3 \tag{1.1.48}$$

$$i\partial_t\psi_4 = -m\psi_4 \tag{1.1.49}$$

For a state of a definite energy E , $i\partial_t \exp(-iEt) = E \exp(-iEt)$ where $\psi = \begin{bmatrix} 1 \\ 0 \\ 0 \\ 0 \end{bmatrix} \exp(-iEt)$,

applying it to the above equation we have :

$$E \begin{bmatrix} 1 \\ 0 \\ 0 \\ 0 \end{bmatrix} \exp(-iEt) = m \begin{bmatrix} 1 \\ 0 \\ 0 \\ 0 \end{bmatrix} \exp(-iEt) \tag{1.1.50}$$

which is equivalent to :

$$E = mc^2 \tag{1.1.51}$$

For the two first equation $E = m$, and for the last two equation $E = -m$. The problem of negative terms has been avoided since doesn't related to the positive one as we see in case of Klein Gordan solution. Dirac said that he thought these perplexing negative energy levels existed physically [14, 15]. Then, he contributed to evaluating a brand-new theory known as the quantum electrodynamic theory(QED). According to this theory, all fundamental particles,

including the electron, have their own quantum field, and what we currently understand as particles and antiparticles are simply these fields vibrations. P. Dirac has predicted the positron existence which have the same properties alike electron plus an opposite charge.

1.1.2 Positron and Positronium's discovery

Positron

Following Dirac's initial assertion of the relativistic Schrödinger equation in 1928. Four years later, experimental confirmation is required. Carl Anderson discovered in 1932 that when a high energy photon from cosmic radiation damages a lead plate, it creates electrons and a new type of particle, which then annihilates with additional electrons to create new photons[1][6]. This confirmation was done in a cloud chamber which is a particle detector made of supersaturated vapor. This vapor becomes ionized and forms a cloud of ions when an ionizing radiation of any sort passes across it. This ion mist leaves behind a trail that can be captured on camera and examined. Different particles with various characteristics will produce unique track shapes. Better yet, the Lorentz force law will cause the particles to curve in the opposite direction if a uniform magnetic field is supplied across this vapor. This particular fact is what made the identification of the positron so straightforward and evident. Figure"1.1.1" is a picture of the positron which Anderson had observed, along with one showing him at work in his Caltech lab. Near the center of the image, a curved track that depicts a particle moving upward and passing through a lead plate can be seen. This curvature was calculated to be exactly the reverse of what one would expect for an electron because of the applied magnetic field.

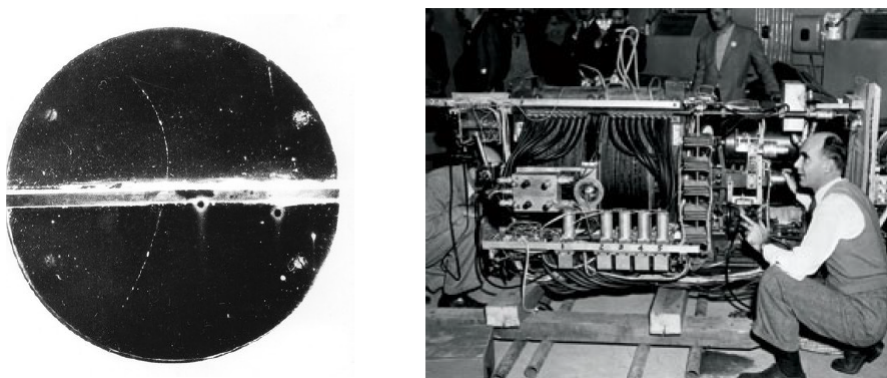


Figure 1.1.1: The discovery of Positron[1]

Positronium

In 1934, Mohorovici'c claimed the presence of a positron and electron bound state, which he (erroneously) thought would be in charge of the mysterious peculiarities in some stars' emission spectra [17]. Kragh (1990) noted that because Mohorovici'c's theories on the characteristics of this new atom were rather bizarre, the term "electrum" that he gave it did not catch on and was eventually replaced by the current name, positronium (Ruark, 1945), with the chemical symbol Ps [18]. Since the reduced mass is half that of the hydrogen atom (1H), its basic (Bohr) spectroscopic structure is identical to that of hydrogen with each energy level being half that of hydrogen. Ps , for instance, has an ionization potential of $6.8eV$. Ps 's ground state is made up of a spin-zero singlet state and three triplet spin states with a total spin of one [19].

$$|\psi_{oPs}\rangle_{(11)} = \left| \frac{1}{2} \frac{1}{2} \right\rangle \left| \frac{1}{2} \frac{1}{2} \right\rangle \quad (1.1.52)$$

$$|\psi_{oPs}\rangle_{(10)} = \frac{1}{\sqrt{2}} \left\{ \left| \frac{1}{2} \frac{1}{2} \right\rangle \left| \frac{1}{2} \frac{-1}{2} \right\rangle + \left| \frac{1}{2} \frac{-1}{2} \right\rangle \left| \frac{1}{2} \frac{1}{2} \right\rangle \right\} \quad (1.1.53)$$

$$|\psi_{oPs}\rangle_{(1-1)} = \frac{1}{\sqrt{2}} \left\{ \left| \frac{1}{2} \frac{-1}{2} \right\rangle \left| \frac{1}{2} \frac{-1}{2} \right\rangle \right\} \quad (1.1.54)$$

$$|\psi_{pPs}\rangle_{(00)} = \frac{1}{\sqrt{2}} \left\{ \left| \frac{1}{2} \frac{1}{2} \right\rangle \left| \frac{1}{2} \frac{-1}{2} \right\rangle - \left| \frac{1}{2} \frac{-1}{2} \right\rangle \left| \frac{1}{2} \frac{1}{2} \right\rangle \right\} \quad (1.1.55)$$

The n^1S_0 Ps decay rate λ_0 into two gammas has been calculated by Pirenne as :

$$\lambda_0(n^1S_0) = \frac{4\rho\sigma(2\gamma)v}{n^3} = \frac{\alpha^5}{2n^3} \left(\frac{mc^2}{\hbar} \right) = \frac{8 \times 10^9}{n^3} sec^{-1} \quad (1.1.56)$$

ρ is the electron density at the position of the positron $\rho = \frac{1}{\pi}(\alpha mc/2\hbar n)^3$, where $\sigma(2\gamma)$ is the Dirac plane-wave cross section for two-photon pair annihilation, which in the limit $\gamma \rightarrow 1$ is given by $\sigma(2\gamma) = \pi r_0(c/v)$ and v is the relative electron- positron velocity, $r_0 = e^2/mc^2$ is the classical electron radius. $(mc^2/\hbar) = 2 \times 10^{22}sec^{-1}$ is the nuclear frequency. Wheeler further stated in 1946 the similar decay rate estimation, he also predicted that the γ 's from bound or free singlet annihilation would be plane polarized with orthogonal planes of polarization if electron and positron have opposite intrinsic parity. Positronium was first demonstrated experimentally in 1951 when Deutsch announced his success in creating Ps in gases. In addition, he had made the first measurements of the hyperfine interaction energy, $W(hfs)$ to $\pm 15\%$ and of $\lambda(1^3S_1)$ to $\pm 10\%$. [20]

The Ps forms mostly in molecular matter, such as porous materials like zeolites or metal-organic frameworks, at areas of low electron density, with a screening cloud of electrons surrounding it [21]. The dynamics of electron-radical recombination, the host material's affinity for electrons, and the environment's ability to block electron-positron attraction all play a role in the creation of Ps . There exist a number of models for how positronium forms, for example, we find the blob model which model the formation of positronium in condensed-matter. Inside the blob composed of free electrons and radicals ionized during the slow-down of positron, the Ps could be created by the positron capturing an electron from the host material or by the binding of a free electron from the implantation track blob in both molecular (polymers, liquids) and porous materials, and escape the blob as a quasi-thermalized Ps . The "spur" model, which operates similarly to the previous one in both liquid and condensed matter, proposes that the formation of Ps results from the interaction of an almost-thermalized positron with an electron released during the ionization of the medium at the end of the e^+ track, in a small region that is home to a number of reactive labile species (electrons, holes, excited molecules). On the other hand, the Ore gap model, which is dependent on the ionization energy of the medium (I) and the binding energy of Ps (E_{Ps}), limits the ability for creation of Ps to positrons within an energy range [22]. The positron kinetic energy E must belong to the interval shown down : $I > E > I - E_{Ps}$. Ore and Powell (1949) find out the decay rate of $1^3S_1 \rightarrow 3\gamma$ as :

$$\lambda_0(1^3S_1) = \frac{2}{9\pi} \alpha^6 \frac{mc^2}{\hbar} (\pi^2 - 9) \simeq 7 \times 10^7 \text{sec}^{-1} \quad (1.1.57)$$

where they also showed that for this process the probability of emission of a γ ray of energy E is essentially linear in E . The best theoretical value for $o - Ps$ lifetime in vacuum is $142.08ns$. Experimentally, it was found to be $141.88ns$ [23]. The pick-off process is the annihilation of positron's $o - Ps$ with an electron of the host material through the two-gamma channel. The $o - Ps$ lifetime typically during that process is ranging between $1-10ns$ depending on the local electron density and size of the open volume pocket [24].

1.1.3 Positron's role as a solid-state property monitor: proof

According to Dirac laws of quantum electrodynamics theory, the two photons of gamma rays annihilation will be separated by 180° at rest. The first person to observe at lab these two simultaneous quanta was Klemperer. However, Debenedetti [25] discovered in 1949 that not

all two gamma rays emitted from positron annihilation in some materials deviated from each other exactly by 180° , they find out a few miliradians of deviation. The test of annihilation radiation by simultaneous pulses might be verified using two scintillators counters. The angular correlation between the two annihilation photons was determined in this experiment. The positron source was ^{64}Cu which was surrounded by a gold absorber that halted the positrons. The distance between the source and either Detector was 120 cm, and the following observation was made: when the detectors are displaced from the horizontal matching it by the source, the counting rate does not vanish for the displacement indefinitely, indicating that annihilation gamma rays are not always emitted in exactly opposite directions, $\lambda \rightarrow p = 0.9 \times 10^{-2}$ in unit of mc It was interpreted as being due mainly by electrons media motion because the positrons having essentially thermalised. Dumond and his coworkers in 1949 had made an accurate measurements of the energy and width of the annihilation gamma-ray line using a crystal spectrometer[26]. They found the width to be greater than that associated with the instrumental resolution. They think that this will attribute to Doppler broadening arising predominately from electronic motion. These investigation leads to the foundation of the Positron Annihilation Spectroscopy technique.

1950 marked the launch and the quick early development of positron techniques. It was discovered that the positron-electron state of the matter is virtually totally responsible for the properties of the annihilation process. The revelation that positrons can offer distinctive information on a wide range of condensed matter physics problems is what has caused the field's explosive expansion. Additionally, the affordable experimental equipment needed for the procedure is readily available on the market. Numerous international conferences have been held with a focus on positron annihilation research[27]. The positron spectroscopy is very useful for studying matter. Because the information is transmitted by the material-penetrating annihilation radiation, it offers a nondestructive way. No particular sample preparation is required, and in some applications, in-situ research are also possible: for instance, on dynamic phenomena at elevated temperatures are possible. On the employment of positrons to examine condensed matter, numerous reviews and bibliographies studies have been written[28].

1.2 Positron-Condensed Matter Interaction

The interaction of positron with matter undergo a standard subsequent steps. It could be backscattered from the surface or loses its energy by different slowing down process to be equilibrated which is called the thermalization. Thereafter, the thermalised positrons get diffused in the medium. The annihilation occur whether in bulk or in defects, the annihilation inside defects got after the trapping process. We will study the evolution of positron-matter interaction starting by describing the thermalisation process. The difference between the known algorithm used to mimic the implantation profile for slow-positron beam will be explained. Then, we will discuss the diffusion process. The backscattering phenomena could be analyzed on the light of previous phenomena once the analytical method use the stopping cross sections and the transmitted one to express with the backscattering probability.

Because the DFT had not yet been established, the Boltzmann technique was utilized in the first theoretical essay that sought to comprehend the annihilation features to their fullest extent. The evolution of the positron distribution in the phase and real space is how the slowing down processes are characterized in the context of the Boltzmann technique. Then, a sophisticated positron distribution and more accurate annihilation characteristics that closely match the experimental values would be provided using TCDFE (Two Component Density Functionnal Theory).

1.2.1 Thermalization

High energetic positrons or slow mono-energetic positron beam are having a kinetic energy greater than the thermal energy of diffusion. So, within the first few picoseconds, the surplus energy is then dissipated by elastic and inelastic scattering off the medium. For instance, a $1KeV$ positron beam will thermalize in an aluminum thin film at a temperature of $600K$ in $3ps$ and $10K$ in $6ps$. While phonon diffusion predominates at low energies and the excitation of conduction electrons predominates in metals, ionization and excitation occur at high energies[29].

Actually, in earlier studies, the Boltzmann equation approach was used to study the dynamic of positrons. Where only momenta in the thermal range are numerically solved. The distribution function is then observed to decline over time toward the Maxwell-Boltzmann distribution and annihilating[30]. Conversely, Perkins and Carbotte examined the dynamic of positrons in

metals using the Green function formalism to find out that positron-phonons contribute to the energy loss at low temperatures [31, 32]. Monte Carlo method is being used by other researchers to simulate the positron mean free path in an electron gas, where they do randomly distribute all the probabilities of each collision type of all positrons entering the media in an effort to simulate the interaction of positrons with matter [33]. By being aware of the cross-section which is usually tabulated for each (energy range, particle, media) for each kind of collision and support a Monte Carlo algorithm.

The slowing down process has been quantified in terms of mean free path, loss energy rate and implantation profile which are a functional of the cross section of the different scattering process.

Implantation profile for high energetic positron

The implantation profile is the result of the thermalization process of positrons. In terms of history, Page et al. and Orth were the first to measure the positron implantation in solids and marked the electric field effect on their deviation. Then, Brindt and Paulin (1977) studied the positron implantation profile of a ^{64}Cu source ($E_{max} = 0.65\text{MeV}$) in 14 different materials with densities $d(\text{g}/\text{cm}^3)$ spanning (0.9–9) [34]. In addition, eighteen elements and six compound solids had their positron mass absorption coefficients determined by Mournin and Paulin (1979) [35].

Consequently, it was proven that the positron implantation profile, after laboriously conducting experiments and analyzing data in comparison to the modern nuclear facilities available today, follows the following formula :

$$P(z) = \exp(-\alpha_+ z) \quad (1.2.1)$$

where α_+ is the positron absorption coefficient

$$\alpha_+ \approx 16 \frac{\rho(\text{g}/\text{cm}^3)}{E_{max}^{1.43}(\text{MeV})} \text{cm}^{-1} \quad (1.2.2)$$

The figure “1.2.1” depicts the implantation profile of ^{22}Na 's continuous positron energy spectrum in silicon.

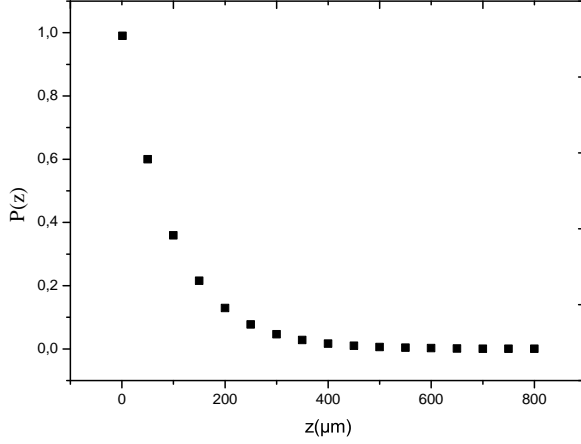


Figure 1.2.1: Energetic positron implantation profile in Silicon

The mean penetration depth \bar{z} is defined when : $P(\bar{z}) = 1/e$ and the information depth or the positron range , \hat{z} in time : $P(\hat{z}) = 0.9999$ Additionally, one can simulate the implantation profile for either high-energy positrons or a slow mono-energetic positron beam using the *GEANT4* toolkit.

Implantation profile for mono-energetic positron beam

Mills and Wilson were the first to test how well positrons transmitted through thin films in order to determine the ideal thickness of the moderators that transferred positrons to apply in slow positron beam experiments which will be explained in **Chapter 2** [36].

The implantation profile $P(z, E)$ is a function of the depth and the incident energy. It had been simulated using Monte-Carlo schemes such as : Valekalehti Nieminen[37], Brookhaven(BNL) and Jensen(+)-Walker(JW)[38]. The main idea of the simulation is tracking positron's trajectories via the cross-section for various scattering processes (elastic + inelastic scattering). The findings are then averaged. The models of cross sections considered vary between each of the MC programs mentioned above. The methodology utilized by Valekalehti and Nieminen is based on Gryzinski's semiempirical expression for the inelastic core and valence electron excitation as well as the screened Rutherford differential cross section for the elastic scattering, taking lattice structure into account. Whereas, the BNL scheme (by following each positron's 10^4 path and had energies between $(1 - 10KeV)$) assume to simulate the implantation profile, backscattered fraction, and transmitted one without taking crystalline structure into account. Although Jensen and Walker keep the same fundamental characteristics as tools like BNL, dif-

ferent inelastic cross section models were used in this case. Regarding how sophisticated the scattering cross-section and geometry are, a great data can be gained from it.

Valkealati and Nieminen[37] were fitted the simulated data for(aluminum, copper, silicon, and gold) using the Makhovian approach and since then, the implantation profile of mono-energetic positron beam could be estimated using the Makhovian function which take the following formula [36]:

$$P(z) = -\frac{d}{dz} \exp\left[-\left(\frac{z}{z_0(E)}\right)^m\right] \quad (1.2.3)$$

with $m = 2$ and $z_0(E)$ related to the mean depth by the following formula :

$$z_0(E) = \bar{z}(E)[\ln(2)]^{-1/m} \quad (1.2.4)$$

In fact, the following integration is used to determine the mean depth. :

$$\bar{z}(E) = \int_0^{\infty} z P(E, z) dz \quad (1.2.5)$$

Since the implantation profile's full integration is the half one, the median depth, $z_{1/2}$, would be estimated :

$$\int_0^{z_{1/2}} P(E, z) dz = \frac{1}{2} \quad (1.2.6)$$

The formula of the style proposed by Katz and Penfold has been used to fit the energy dependence of the mean depth :

$$\bar{z} = \frac{A}{\rho} E^n \quad (1.2.7)$$

Where A, n are empirical parameters dependent on the material. $\rho(g/cm^3)$: density of the material. Ghosh and their colleagues(1995) showed that the formula [1.2.7] could be used to fit JW scheme data for variety of materials throughout an energy range of 1–25keV. Tables for fits parameters have been produced[39]. Experimentally, the empirical parameters were confirmed for silicon [40] [2] and here is the figure “[1.2.2]” depicts Makhov profiles $P(z, E)$ in silicon calculated for 1.5 – 3 – 5 and 10KeV incident positron energies, considering $A = 4\mu gcm^{-2}KeV^{-n}$ n=1.6

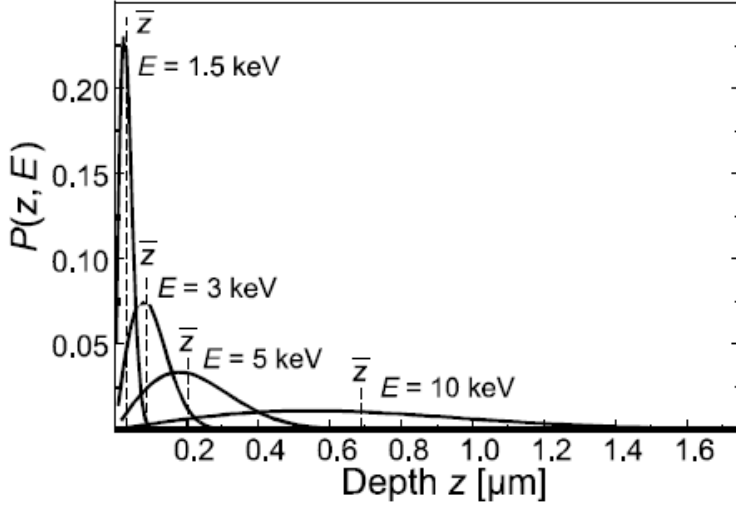


Figure 1.2.2: mono-energetic positron beam implantation profile in Silicon[2]

For Polymers, the implantation profiles are indirectly measured [41]. $P(z, E)$ is crucial to understand initially since it will help us determine how defects are evolving from the positron implantation profile. Monitoring of defects as a function of depth is possible by varying the positron energy in the range of a few eV to many tens of keV . The explanation of positron moderation, measurement principles, and application of slow-positron-beam technique for defect depth profiling will all be covered in *Chapter 2*.

1.2.2 Diffusion

After positrons get thermalized, they diffuse through the material and behave as charged particles. Here, the function of distribution attends the time-independent behavior where the positron momentum distribution follows the Maxwell Boltzmann statistics. The positron scattering is quasi-elastic, the positron spatial distribution could then be described by the following diffusion-annihilation equation[42].

$$\frac{\partial f(r, t)}{\partial t} = D_+ \nabla^2 f(r, t) - [\lambda_b + \kappa(r)] f(r, t) - \nabla [V_d(r) f(r, t)] + f_i(r, t) \quad (1.2.8)$$

D_+ : Diffusion coefficient

V_d : positron drift velocity

λ_b : free defect (bulk) annihilation rate

κ : trapping rate

The effective positron lifetime in the delocalized state is defined as the sum of the positron annihilation rate and the trapping rate.

$$\lambda_{eff}(r) = 1/\tau_{eff}(r) = \lambda_b + \kappa(r) \quad (1.2.9)$$

Only simple cases can be solved analytically (layered structures with interfaces). Otherwise, the diffusion parameters are then simulated. The diffusion coefficient can theoretically be determined if the scattering process is understood[43]. A more understandable equation is provided by the semi-classical random walk theory which provide the more used formula :

$$D_+ = \frac{\langle v^2 \rangle^{1/2} l}{3} = \tau_r \frac{K_B T}{m^*} \quad (1.2.10)$$

where :

$$\langle v^2 \rangle = \frac{3K_B T}{m^*} \quad (1.2.11)$$

$\langle v^2 \rangle$: The average of the square of positron thermal velocity

l : is the positron mean free path between events.

τ_r : the corresponding relaxation time which determined from the microscopic scattering rate.

The formula 1.2.10 is accurate for the scattering types of : elastic scattering, scattering off impurities, quasielastic scattering off acoustic phonons[44].

It is reported that polymers have a positron diffusion length L_+ of about $100nm$.

$$L_+ = \sqrt{\tau_b D_+} \quad (1.2.12)$$

The diffusion parameters may be utilized as a kind of material characterization, particularly when used in conjunction with experimental findings since they can reveal information on defect patterns as well as the precise locations of the annihilation sites[45].

1.2.3 Backscattering

This phenomena might be regarded as the initial step. When positron beams strike a substance, the repelling coulombic potential creates a probability of backscattering which is well

considerable in slow positron beam experiments. Positrons returning to the surface with energy above 50eV were the origin of the backscattered flow [46]. The object of figuring out the absolute positron backscattering probability is to prevent recording annihilation events caused by backscattered positrons in slow positron beam investigations. Both theoretical and experimental investigation has been done to investigate the backscattered probability yield in thin films. The analytical expression of the backscattering probability is directly proportional to the stopping cross sections and the transmitted one. The stopping cross-section describes the effect of inelastic scattering processes while the transmitted cross-section accounts for the angular deflections of the particle which is the result of elastic scattering [47]. The backscattering probability formula is written as follows :

$$\eta = 1 - F(\sqrt{t_0}) \quad (1.2.13)$$

where :

$$F(x) = \exp(x^2)(1 - \text{erf}(x)) \quad (1.2.14)$$

with t_0 is :

$$t_0 = \frac{1}{3} \sigma_{tr}(E)^2 \int_0^E [S(E') \sigma_{tr}(E')]^{-1} dE' \quad (1.2.15)$$

Where

$$\sigma_{tr} = \lambda^{-1}$$

λ is the transmitted mean free path and $S \propto \frac{Z}{E}$.

Then, as we see in precedent sections, A Monte Carlo program should be run in order to reproduce the backscattered fraction [48]. From an experimental standpoint, we find that observations of coefficients η for the backscattering of positrons from elemental solids are reported as a function of atomic number Z and incident energy E [47] [49]. While, it was modeled on the behind of others like founded here [50].

Nowadays, the backscattering coefficient could be simulated using GEANT4. For example, we find the first study of the backscattering coefficient is done in amorphous polymers where the results of the simulations and the previous experiment are in rather good accord [38].

1.2.4 Positron States

As previously demonstrated, the quantifying of positron-condensed matter interaction up to diffusion might be accomplished using a semi-empirical or MC simulation techniques. The next stage is to annihilate once the positron has been diffused. The study of the phenomenon has received extensive research in the context of the DFT approach. In the 1960s, there were other works available to calculate the annihilation rate. When the second quantification of the electron and positron quantum fields made for the description of the positron annihilation rates in metals [51] [52]. The theoretical members are drawn to the DFT toolkits, particularly given the rapid advancement of computational software. It is well known that the density functional theory (DFT) is the last fashion before QMC calculation and ML(Machine Learning) based-techniques of electronic structure calculation since 1965 [53] [54]. Numerical simulations have since turned into a sophisticated technique. The Quantum Monte Carlo (QMC) methodology, a strong simulation tool that is also used to anticipate positron states, is one of the numerical simulation methods that are employed [55] [56]. It is, however, outside the purview of our thesis.

In this subsection, we will study how the positron state could be calculated in an extended DFT framework. The start point was with Boronski and Nieminen1986 [57]. They had been developed a full tow component density functional theory (TCDFE) calculation for systems containing electrons and positrons where the ground state energy of such system in an external potential V_{ext} written as a functional of electron $n_-(r)$ and positron $n_+(r)$ densities as shown below.

$$E[n_-, n_+] = F[n_-] + F[n_+] + \int dr V_{ext}(r)[n_-(r) - n_+(r)] - \int dr \int d\hat{r} \frac{n_-(r)n_+(\hat{r})}{r - \hat{r}} + E_c^{e-p}[n_+, n_-] \quad (1.2.16)$$

where $F[n]$ denotes the following one component functional for electrons or positrons.

$$F[n] = T[n] + \frac{1}{2} \int dr \int d\hat{r} \frac{n(r)n(\hat{r})}{r - \hat{r}} + E_{xc}[n] \quad (1.2.17)$$

$T[n]$ is the kinetic energy of noninteracting electrons or positrons.

$E_{xc}[n]$ is the exchange correlation energy between indistinguishable particles.

$E_c^{e-p}[n_+, n_-]$, the correlation energy functionnal.

The ground state densities that minimizes $E[n_-, n_+]$, could be obtained by solving the following khon-Sham equations.

$$-\frac{1}{2}\nabla^2\psi_i(r) + \left[\frac{\delta E_{xc}[n_-]}{\delta n_-(r)} - \phi(r) + \frac{\delta E_c^{e-p}[n_+, n_-]}{\delta n_-(r)}\right]\psi_i = \epsilon_i\psi_i(r) \quad (1.2.18)$$

,

$$-\frac{1}{2}\nabla^2\psi_i^+(r) + \left[\frac{\delta E_{xc}[n_+]}{\delta n_+(r)} - \phi(r) + \frac{\delta E_c^{e-p}[n_+, n_-]}{\delta n_+(r)}\right]\psi_i^+ = \epsilon_i^+\psi_i^+(r) \quad (1.2.19)$$

Where :

$$V^+(r) = \frac{\delta E_{xc}[n_+]}{\delta n_+(r)} - \phi(r) + \frac{\delta E_c^{e-p}[n_+, n_-]}{\delta n_+(r)} \quad (1.2.20)$$

which present the positronic potential and $\phi(r)$ is the total coulomb potential , its function is as follows:

$$\phi(r) = \int d\hat{r} \frac{-n_-(\hat{r}) + n_+(\hat{r}) + n_0(\hat{r})}{|r - \hat{r}|} \quad (1.2.21)$$

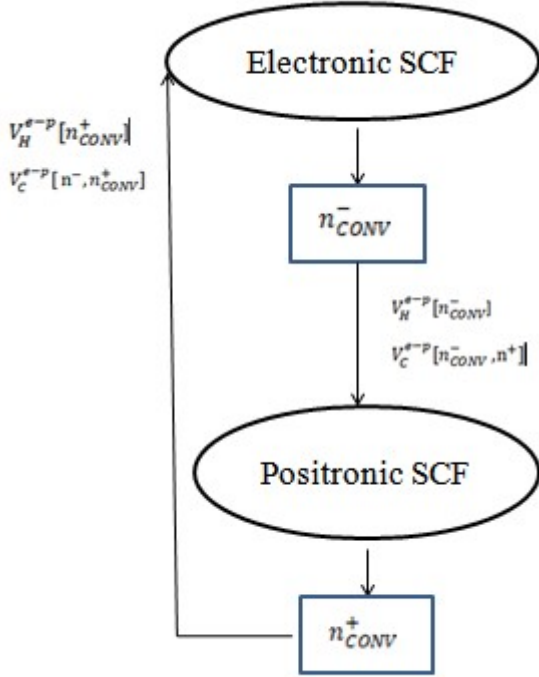
where $n_0(r)$ denotes the positive charge density providing the external potential and it contains the Hartree and external potentials. The electron and positron densities provided by summing over the occupied states.

$$n_-(r) = \sum_{E \leq \epsilon_F} |\psi_i(r)|^2 \quad (1.2.22)$$

,

$$n_+(r) = \sum_i^{N_+} |\psi_i^+(r)|^2 \quad (1.2.23)$$

ϵ_F is the electron fermi energy, N_+ is the number of positrons. The equations must be solved self-consistently and simulteneously using the TC-DFT algorithm [\[1.1\]](#)



Positron State in Bulk :

In case of delocalized positron in a perfect lattice, the two component DFT might be solved easily without the necessity of the self-consistent condition between the positron and electron densities as it must be done in the standard scheme. The conventional approach relies on computing the electron density using a well-known ab-initio code, such as Abinit, Wien2k, Casino, or Quantum Espresso, without taking into account the positron disturbance. Positronic density calculations frequently take into account the presence of just one positron in a material. The Hartree self-interaction components of the positron are then corrected by the positron exchange-correlation term $E_{xc}[n_+]$ as follows :

$$E_{xc}[n_+] = -\frac{1}{2} \int dr dr' \frac{n_+(r)n_+(r')}{|r - r'|} \quad (1.2.24)$$

The matching components in the positron's potential therefore cancel as

$$\frac{\partial E_{xc}[n_+]}{\partial n_+(r)} = - \int dr' \frac{n_+(r')}{|r - r'|} \quad (1.2.25)$$

Hence, its self exchange-correlation energy should exactly balance out the positronic coulomb energy. The resultant potential sensed by positron is composed of the electronic Coulomb

potential, external potential and the correlation potential between electrons and positron.

$$V_+(r) = - \int dr' \frac{n_-(r)}{|r - r'|} - V_{ext}(r) + V_{corr}(r) \quad (1.2.26)$$

Then, the positronic density can be determined by solving the Kohn–Sham equation. The conventional method succeeds beautifully of providing the bulk state, when the positron density is incredibly small throughout every position in the lattice and has no impact on the electronic structure. Conversely, the situation will be different if positron is concentrated at a lattice defect so the positron attracts electrons, and indeed the average electron density rises close to the defect. However, the conventional approach also performs admirably in the majority of applications for positron states at defects. In order to get a good wave function, an appropriate correlation potential have been required. There are tow main models of correlation energy functional. The first correlation energy modeled on the context of the Local Density Approximation(LDA) and the second one is the General Gradient Approximation (GGA).

The LDA is modeled on the idea that the correlation energy at a particular site in the host system depends exclusively on that location’s electron density. The gradient of the electron density contribution is added to the local density component concurrently by the GGA. The instance of the vanishing positron density in a homogeneous electron gas provides the greatest understanding of the electron-positron correlation energy [58][59][29].

Using Lantto[60]data, the evolution of the electron-positron correlation potential as a function of electron density was examined by Boronski and Nieminen in 1986. Using interpolation formulae, practical computations can be performed within LDA which take the following formula of V_{LDA}^{corr} (in Ry)

$$V_{LDA}^{corr} = 1.14 - 1.56/\sqrt{r_s} + (0.051\ln r_s - 0.081)\ln r_s, \quad (1.2.27)$$

$$r_s \leq 0.302$$

$$V_{LDA}^{corr} = -0.92305 - 0.05459/r_s^2 \quad (1.2.28)$$

$$0.302 \leq r_s \leq 0.56$$

$$V_{LDA}^{corr} = -13.15111/(r_s + 2.5)^2 + 2.8655/(r_s + 2.5) - 0.6298 \quad (1.2.29)$$

$$0.56 \leq r_s \leq 8.0$$

$$V_{LDA}^{corr} = -179856.27683 \left(\frac{3}{4\pi r_s^3} \right)^2 + 186.4207 \left(\frac{3}{4\pi r_s^3} \right) - 0.524 \quad (1.2.30)$$

$$r_s \geq 8.0$$

where r_s is defined as $r_s = \left(\frac{3}{4\pi n_e^-} \right)^{1/3}$.

The GGA correlation potential is related to the LDA one as follows :

$$V_{GGA}^{corr} = V_{LDA}^{corr} \exp(-\alpha\epsilon) \quad (1.2.31)$$

here α is an adjustable parameter, and ϵ is defined as

$$\epsilon = \frac{|\nabla \ln(n_{e^-})|^2}{q_{TF}^2} \quad (1.2.32)$$

(q_{TF}^{-1} : is the local Thomas Fermi screening length). For the majority of the elements in the periodic table, theoretical positron lifetime values have actually been systematically determined using self-consistent and non-self-consistent methods. The acquired results have been examined and contrasted with experimental data that are generally in good agreement with values from earlier experiments[61].

Positronium state

Due to the minimal Ps -matter repulsion, the Ps state can localize at open volume. Ps 's capacity to trap in these kinds of imperfections gives it this advantage in condensed-matter characterisation. The most used model known as a standard low to mimic the Ps structure is a single particle type-model. One considers the Ps as a distinguishable particle, taking into account that Ps having a long lifetime inside the imperfections where it interacts weakly then, annihilates through the pick-off process. The model developed by Tao[62] and parametrized first by Eldrup[63]. The last simulate Ps that interact with a small pores and voids (<2 nm) via a spherical potential. The correlation of Ps lifetime to the (pore/void) radius is verified. For some other potential shapes such as rectangular or elliptic, we find an updated version of the standard model of Tao and Eldrup. Furthermore, it find out that Ps could be annihilated in an excited state if the voids($\geq 10nm$) [64].

But, the standard model has a number of limitations that make it tricky to apply in polymers. First off, soft matter does not often justify the notion of spherical holes. Second, assuming hard walls and a homogenous electron density, the polymer matrix's atomic structure is completely disregarded. Third, despite the fact that translationally excited states of *Ps* are accessible at room temperature, temperature is not taken into consideration. Hence, a reasonable simulation of *Ps* structure must be constructed using an accurate many-body ab initio techniques.

Nevertheless, the electronic characteristics of soft-matter molecules are not significantly changed in the condensed form and they attach through weak dispersion interactions[65]. For the last reason, we can apply in our work, a Buckingham potential which expressed with an empirical ansatz proposed by Schmitz and Müller-Plathe [66]. In their model, the positronium moves in a static potential energy landscape produced by the polymer structure. Then, they approximated the overall *Ps*-positron potential by a superposition of atom-*Ps* interaction potentials for a single particle without internal structure, V_{eff}

$$V_{eff} = \sum_{atoms} V_i(|r - R_i|) \quad (1.2.33)$$

where

R_i : the positions of the nuclei.

The attractive van der Waals attraction, which occurs between any two atoms, and the Pauli repulsion between the matrix electrons and the *Ps* electron are the two main factors that contribute to the interaction energy of an atom and a *Ps* particle.

$$V_i(r) = A_i \exp(-r/b_i) - C_i/r^6 \quad (1.2.34)$$

Hence, by solving a single particle Schrödinger equation for the superposition potential, it is possible to determine the ground-state energy and the *Ps* density using DFT as like the positronium bulk state.

1.2.5 Positron-electron Momentum Density :

Moreover, the framework of TCDFE provide us the positron-electron momentum density formula which is equivalent to the momentum distribution of annihilation photons :

$$\rho(p) = \pi r_e^2 c \sum_i \left| \int dr \exp(-ip.r) \psi_i^{e-p}(r) \right|^2 \quad (1.2.35)$$

$\psi_i^{e-p}(r)$ is the tow particle wavefunction in the state i and p is the given momentum. Considering that the electron and positron are independent, we rewrite ψ_i^{e-p} as a product of the electronic and positronic wave functions: $\psi_i^{e-p}(r) = \psi^+(r)\psi_i^-(r)$. Once taking the correlation effects between the electrons and positrons into account, then the positron-dependent enhancement factor $g(n^-, n^+)$ could be included which leads to the expression[67]:

$$\rho(p) = \pi r_e^2 c \sum_{i,j} \left| \int dr \exp(-ip.r) \psi_i^+(r) \psi_j^-(r) \sqrt{g(n^-, n^+)} \right|^2 \quad (1.2.36)$$

According to the formula $p = \frac{h\nu}{c} - \frac{h\nu'}{c}$, measuring the Doppler broadening of the annihilation radiation indicates the momentum distribution of electrons detected by positrons in the material. Hence, for positron annihilation measurements to be used successfully in defect identification, related theoretical and computational work must produce simulated annihilation characteristics that can be compared to the measured ones. Several calculations have been made to predict the positron-electron momentum density in bulk materials and in compound semiconductors[68][69][67].

1.2.6 Annihilation Rate:

The annihilation rate λ in a particular system is expressed as the inverse of the positron lifetime τ^{-1} and is proportional to the overlap of the electron and positron densities which could be written as :

$$\tau^{-1} = \lambda = 4\pi r_0^2 c \int dr n_+(r) n_-(r) g(n_+, n_-) \quad (1.2.37)$$

where :

$g(n_+, n_-)$ is the electron-positron pair-correlation function (it is called also, the contact density) calculated at the point in a homogeneous two-component plasma with positron density n_+ and electron density n_- . This represents an increase in annihilation brought on by the positron's surrounding electron-screening cloud[70][29].

r_0 : the classical electron radius, and c is the speed of light.

The independent-particle model (IPM) or Sommerfeld result for positron annihilation in a

homogenous electron plasma with density n_- serves as the prefactor

$$\lambda_0 = 4\pi r_0^2 c n_- \quad (1.2.38)$$

The positron lifetime τ , can be obtained by integrating $\rho(p)$ over the momentum :

$$\tau^{-1} = \lambda = 1/(2\pi)^3 dp \rho(p). \quad (1.2.39)$$

Concerning the o-Ps rate annihilation could be well approximated with $g(n_+, n_-) = 1$ [71]

Based on Lantto's (1987) many-body calculations, Boronski and Nieminen (1986) provided a useful interpolation formula for the pair-correlation function $g(n_+, n_-)$. It has the appropriate low-density (i.e., the positronium atom) and high-density (i.e., the randomphase approximation) restrictions. g is expressed as a function of both the local electron and positron densities. But, within the the CS and in the limit $n_+ \rightarrow 0$ it will be function of only electron density $\gamma(n_-)$ [68]. A number of formulas have been constructed that interpolate the enhancement factor and produce various schemes that match the correlation potential and the enhancement factor. Therefore, it is crucial to conduct a systematic analysis of the effectiveness of various schemes (including their correlation potential and enhancement factor). The reader can find seven formulas of the enhancement factor in [72] where a significant comments have been made here regarding the effects of enhancing factors employed in calculations.

However, in the case of a simulation using the standard model of Tao-Eldrup, the material's electron density creates a layer on the well's surface that is ΔR thickness thick. The overlap of the single particle and material electron densities is used to determine the pick-off annihilation rate, λ_{o-Ps}^{TE} , as shown below :

$$\lambda_{o-Ps}^{TE} = 2(n_s^{-1}) \left(\frac{\Delta R}{r_h + \Delta R} + \frac{1}{2\pi} \sin \left(\frac{2\pi r_h}{r_h + \Delta R} \right) \right) \quad (1.2.40)$$

r_h : the radius of the sphere

ΔR : 0.166nm

$2(n_s^{-1})$: is the spin-averaged annihilation rate of p-Ps and o-Ps,

In the plateforme of DFT calculation, there are an open sources toolkits doing the calculation of positron annihilation properties in solids like PositronAbint, which calculates the LT and the

momentum distribution of an annihilated positron in crystalline materials[67]. Also, Doppler program offered us the positron annihilated characteristics in a crystalline media. Besides, it exists a lot of DFT toolkits assumes the calcul of the electronic density in different types of matter like KSSOLV and M-SPARC (written in MATLAB) which offers a framework for quick prototyping for the creation and testing of creative algorithms and techniques for real-space DFT[73].

*In our thesis: we are writting a code using python language to assume simulation of the positron annihilation lifetime using the TC-DFT (Conventioanl way) in CR39 which will be demonstrated in **Chapter 4**.*

Conclusion

The fundamental theoretical concepts in developing the PAS technique are presented in this chapter, and we acquire a thorough summary of all the calculations involving the Dirac equation, whose elegance personally captivates me. A broad overview of the positron states was then completed. Knowing that there may be more likely phenomena that we have not yet examined, such as channeling and trapping, we sought to resume the crucial phase of the positron-condensed matter interaction in the following. Regarding the simulation of positronic density in bulk and defects, a narrowed arte state had been constructed. Calculating the annihilation rate or the lifetime of the positron state is the goal of the previous analysis. The positron lifetime is an experimental parameter that hold a clear significance on the structural properties of the material. In order to comprehend the fundamental characteristics of the system under study, it is therefore of utmost relevance.

Chapter 2

PAS Techniques

Introduction

This chapter is intended to introduce the reader to the experimental techniques used in our work. In order to do that clearly, we will divide it into two principal sections. In the Sec"2.1", the description of each component belonging to the positron spectrometer setup has been well studied. The setup components could be a positron source, detector, electronic device or an acquisition system. Then, in the Sec"2.2", we will describe carefully, the functionality principles of PALS, DBS and VEDBS techniques. There exist other techniques such as Age-Momentum Correlation(AMOC), Angular Correlation Annihilation Radiation(ACAR), but they are beyond the scope of our thesis. As the goal of each characterization technique is to reveal a basic structure property, we will establish at the end of each method, the structure property that could be extracted with.

The first part needed to build such spectrometer is the positron source. The positron source could be existed naturally in radioactive elements(^{22}Na , ^{55}Co) or produced via facility-based beams which will be described in Subsec"2.1.1". The goal of the spectroscopy directed to investigate matter properties, by means of detecting the gamma radiation issued from the annihilation of positrons implanted into the sample. Thereby, the study of gamma detectors is undertaken in Subsec"2.1.2". Then, the electronics modulus that assume the accumulation of events is discussed in Subsec" 2.1.3".

The description above is followed by a survey that concentrates on three methods: positron lifetime measurement (PALS), Doppler broadening spectroscopy (DBS), and Variational Energy Doppler broadening spectroscopy (VEDBS). These methods are being discussed in relation to their respective applications and capabilities in the field of materials characterization.

2.1 Technical Instruments

In the current section, a coherent description of the generation of positron and detection of their annihilation radiation is followed by a survey of technical instruments used for positron lifetime measurement, Doppler broadening spectroscopy will be demonstrated.

2.1.1 Positron Sources

To stay safe in a nuclear lab, it is sufficient to guarantee that adequate lead shielding is supplied around the source location in the laboratory setting, and that the need for close closeness to this region is minimized. Much more shielding procedures are typically required in reactors because of the substantially higher ambient radiation levels. There are two general types of positron sources. The first is the radioactive source where the positrons are heigh energetic and have a broad spectrum. It is generally use in the traditional methods. The second type of source is designed for beam experiments. The facilities known where the positron beam could be generated are well the reactors and the accelerators.

Radioactive sources

Amongst the β^+ emitters, the radioactive sodium source ${}^{22}_{11}\text{Na}$ where its decay sheme is depicted in Fig'2.1.1' is broad used in positron lab[3]. The source have been prepared from salt in solution by evaporative deposition for activity $< 37\text{MBq}$. Also, could be prepared in capsule form where considered to have a better intensity[74]. The ${}^{22}\text{Na}$ is the most popular source because of its behavior, which includes a long half-life (2.6y) and an affordable price. The positron flux is clearly defined and maintains a constant value throughout an experiment. After emitting the positron with maximum energy of 0.545MeV .



The ${}^{22}\text{Na}$ nucleus decays to an excited state of ${}^{22}\text{Ne}$ which then get its ground atomic state with the emission of 1.274MeV gamma ray. The detection of this rays will be investigated in the PALS as it will be studied in subsec'2.2.1'. Detecting the corresponding positron annihilation components in the material source and in the foil is a real problem when employing ${}^{22}_{11}\text{Na}$ source. It has been discovered that one way to reduce the source and material annihilation components is to select a radioactive emitter with a higher positron energy. We discover that the ${}^{44}\text{Ti}$ (with:

half-life $47y$, maximum energy $1.47eV$, simultaneous gamma rays $1.16eV$) could be a substitute source as a radioactive positron emitter. But their increased price puts a cap on our aspirations. Moreover, the gamma rays will increase the background using the DBS technique. Then, gamma rays is both unnecessary and even unfavorable. It is preferable to use a source with less gamma radiation coupled with positron emission, like ^{68}Ge [75]. Unfortunately, ^{68}Ge has a short half-life of only 275 days. For high-flux beam measurements in the lab, ^{58}Co has frequently been used [76]. Because of its short 71-day half-life, ^{58}Co is cost-effective. Nevertheless, because it produces many gamma rays per positron, many of which are not time-related to the positron, ^{58}Co is not suited for typical lifetime or Doppler-broadening spectroscopies.

The most recent problem with high-quality availability allowed studies to look at domestic development of appropriate sources [77]. Originally, Wen et al has firstly built an internal device for drop-depositing up to $740MBq^{22}Na$ from $^{22}NaCl$ solutions and sealing with $3\mu m$ Ti [78]. At the N.A.C. in South Africa, $^{22}NaCO_3$ has been produced by Britton et al. [79].

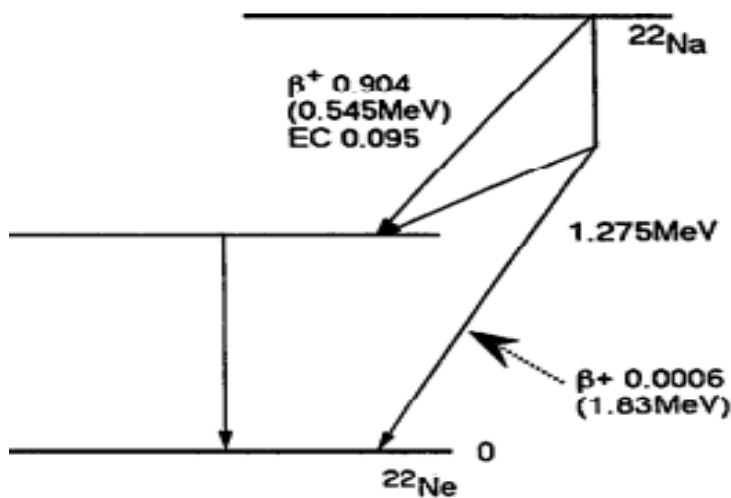


Figure 2.1.1: Sodium ^{22}Na Decay Shem [3]

Facility-based positron beam

The energy conversation low enable the synthesis of matter and antimatter. It is possible to make an electron-positron with a minimal gamma energy of 1.022 MeV in vicinity of a nucleus. Although, it is considered one of the most difficult nuclear applications ever. For instance, in CERN a significant efforts have been made to produce the anti-proton for required experiments. In reality, the idea to generate the positron beam comes when Cherry [80] made the observation of positron emission from a solid surface. Then, positron beam generation was based at a LINAC

facility [81]. At the level of linac, the Bremsstrahlung gamma radiation issued from the intense (50MeV) LINAC electrons produces electron-positron pairs in ^{180}Ta target. Or, using table-top proton and deuteron accelerators, the high energy of the intense radioactive source such as the ^{27}Co could be manipulated to produce a slow positron beam. But a hard maintenance of the cyclotron is undiscussed need.

Alternatively, positrons could be produced also via the gamma energy at a nuclear reactor. Thanks to neutron capture which will generate the intense gamma which will convert to positron-electron pairs using a suitable target. We find Lynn at Brookhaven [82] used for the first time a reactor-based slow positron beam using the copper. A copper ball was irradiated in the reactor core $^{63}\text{Cu}(n, \gamma)^{64}\text{Cu}$. In Munich reactor, the cadmium has been used as a target, $^{113}\text{Cd}(n, \gamma)^{114}\text{Cd}$. [77].

In our lab, we used the ^{22}Na source made at CRNA. This preparation is done using a salty, aqueous, and transparent radioactive mother solution $^{22}\text{NaCl}$; the latter has an activity of 2.5mCi and is placed in a glass bottle and kept in a lead container. Then, using a micropipette, they delicately removed a drop of a few microliters from the mother radioactive solution and placed it on a thin, 12-micrometer-thick sheet of kapton. This created a point (point source). The volume that is selected and, consequently, the quantity of droplets dropped, determine the activity of the source that must be prepared. Once the drop of sodium has been deposited, a drying procedure is performed. In order to evaporate the quantity of water contained in this drop. After drying, another sheet of kapton is glued to the first (sandwich-shaped source). Finally, the whole (kapton/source/kapton) is cut in the form of a square of size 0.5 cm^2 . Figure “2.1.2” shows the ^{22}Na source on the kapton support. The specific activity of the source used is $40\mu\text{Ci}$.



Figure 2.1.2: Radioactive source + Micropipette

2.1.2 Gamma Detectors

Radiation detectors are constructed based on their interactions phenomena with matter, which

give rise to various phenomena. These phenomena derive from the excitation, ionisation or diffusion. The lost energy of the penetrating particle through the medium detector made the function of detectors response. Depending on that, the detectors are classified into three general types: Ionisation detectors, scintillation and the semiconductor detectors.

Talking about gamma detectors, the last two types are considered in gamma ray detection because they are faster than the ionization detectors, more efficient when the necessary energy to create a photon is 25eV in the NaI(Tl) detector and 100eV for plastic scintillator. In plus, they have a good linearity in response. The most specific property of the semiconductor detectors is the excellent resolution. The plastic scintillation detector, a type of scintillation detector and the HPGe detector are employed in PAS technique due to their advantages. The ability to rapidly gather and create light signals as well as their ability to give good resolution in time and energy are key factors. In this subsection, the functionality operating of Plastic scintillator and the photomultiplier tubes (PMT) which form together a combined detector and the HPGe detector will be verified. The special types of detectors used in our work will be subjected also.

Scintillators

The principal working of scintillation detector could be resumed in the following notes. Gamma rays interact with scintillator medium via (photo-electron effect, Compton diffusion and particles production) which cause the loss of all or some of their energy in form of kinetic energy and is dissipated in the detector. The deposited energy on the scintillator will belong to the UV-VIS part of the EM spectrum which is the reason behind the name scintillator. The photons will be converted to an electric signal using the PMT device (this will be explained in the next subsection). There are several types that realize these conditions such as: the organic scintillators (plastic, liquid, crystal) which their scintillation mechanism is called fluorescence and based upon the excited states of the molecules. We find also, the inorganic type, like the famous NaI(Tl) and CsF_2 , BGO , here, the fluorescence is created via impurities which makes an intermediate state. Talking about the plastic scintillators, it is made out of an organic scintillating molecule in a solvent polymerized. Plastic scintillators are a very valuable type of organic scintillator due to how easily they can be formed and manufactured. A common plastic scintillator emits the most scintillation at a wavelength of about 425nm . With an average light output of 25–30 of NaI(Tl) and a comparatively quick decay period of only 2ns , plastic scintillators stand out from other types of scintillators. The material is therefore suitable for

ultra fast timing measurements. All plastic scintillators are responsive to charged particles, fast neutrons, gamma radiation, and x-rays. Along our thesis work, we were using two types of scintillators which are well the BC418 and EJ228. For the best timing results, it should be utilized in tiny sizes to reduce photon scattering effects.

BC418 and EJ228 Scintillator BC418 and EJ228 plastic scintillators are made of polyvinyltoluene polymer based. It is soluble in aromatic solvents, chlorinated solvents, acetone, etc. In addition, it is unaffected by water, dilute acids, lower alcohols, alkalis and pure silicone fluids or grease. The majority of epoxies can be used safely with these scintillators. They are designed for use in timing applications that need extremely fast response times and where there are extremely high count rates. To minimize the effects of photon scattering, it should be utilized in small sizes, with the biggest scintillator dimension being less than 10 cm. The most essential characteristics of those scintillators are mentioned in "Table(2.1)"

	<i>BC418</i>	<i>EJ228</i>
Light Output, %Anthracene	67	67
Rise Time(ns)	0.5	0.5
FWHM(ns)	1.2	1.2
Decay Time(ns)	1.4	1.4
The maximum emission wavelength λ_{max} (nm)	391	391
Density(g/cm^3)	1.032	1.032
Refractive index	1.58	1.58
Atomic Composition($\times 10^{22} N/cm^3$)		
C	4.74	4.69
H	5.21	5.15
Electrons	30.37	30.33

Table 2.1: BC418 and EJ228 scintillators characteristics

Photomultiplier (PMT)

In order to translate the energy deposited upon the scintillator to a readable output signal, it has been attached to the Photomultiplier (PMT). The photomultiplier is a customizable tool that offers an incredibly fast response and excellent sensitivity. As seen in Fig"2.1.4", a PMT tube is made up of a photoemissive cathode (photocathode), focusing electrodes, an electron multiplier (dynodes), and an electron collector (anode) inside of a vacuum tube. The photocathode releases photoelectrons into the void when light enters the photocathode. The voltages of the focusing electrodes then direct these photo-electrons in the direction of the electron multiplier, where they are multiplied by a secondary emission process. The anode then collects the multiplied electrons as an output signal. A photo-cathode is present in the

PMT in either a side-on or a head-on arrangement as seen in Fig”2.1.5”. In contrast to head-on types, side-on types receive incident light through the side of the glass bulb. Head-on types receive light through the glass bulb’s end. A semi-transparent photo-cathode (transmission mode photo-cathode) is deposited on the interior surface of the entrance window for the head-on type or (the end-on type).The head-on type provides better uniformity than the side-on type having a reflection mode photocathode.

The employment of a low-noise electron multiplier, which amplifies electrons through a cascade secondary electron emission process, is what gives photomultiplier tubes their superior sensitivity (high current amplification).

The electron multiplier is made up of dynodes, which are electrode stages that range in number from 8 to 19. There are currently numerous main varieties in use. Like the circular cage type, box + gride type, Linear focused type, box + line type, circular + linear focused type, venetian + blind type, mesh type, microchannel plate MCP, and metal channel type.

The photocathode transforms incident light energy into photoelectrons. The wavelength of the incident light has an impact on the conversion efficiency. The sensitivity of the photocathode calculated by the quantum efficiency which is the number of photon-electrons emitted divided by the number of the incident photons. Another quantity has been used, the radiant sensitivity, S : which present the photon electric current from the photocathode divided by the incident radiant power at a given wavelength. $[S] = A/W$. The relationship between the S and QE is shown in the formula”2.1.2”

$$QE = \frac{S \times 1240}{\lambda} \times 100 \quad (2.1.2)$$

The spectral response characteristic as shown in Fig.”2.1.3” refers to this link between photocathode sensitivity; (S , QE) and the wavelength.

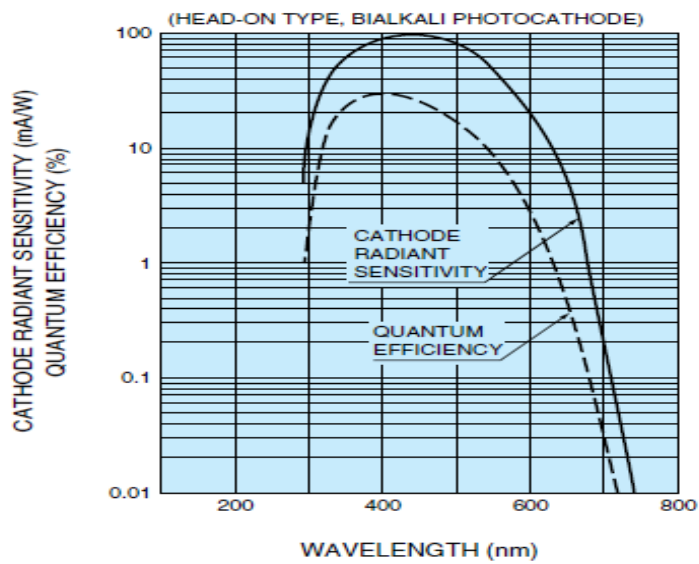


Figure 2.1.3: The spectral response of Bialkali photocathode

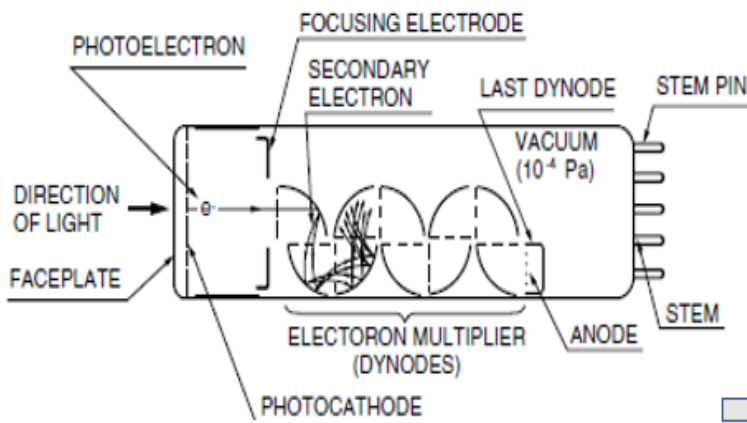


Figure 2.1.4: Cross section of PMT

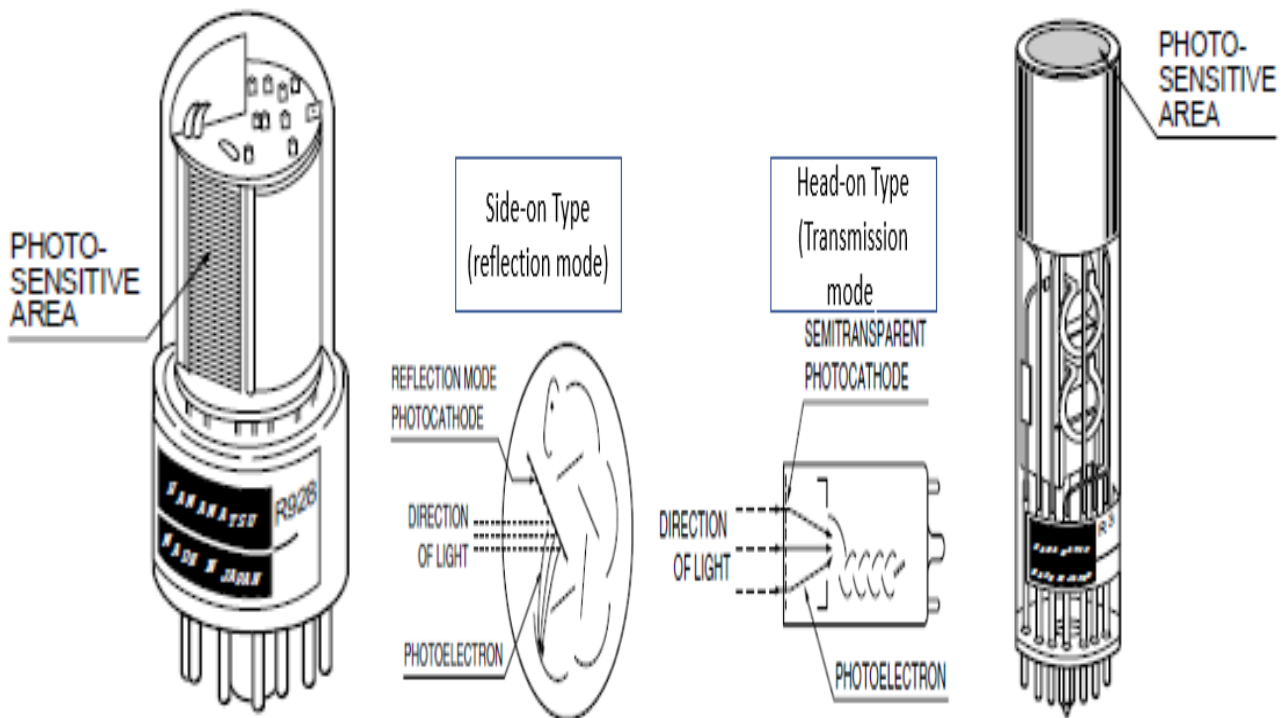


Figure 2.1.5: Photocathode type and mode light transportation

Burle 8850 BURLE 8850 like is shown in Fig. 2.1.6 is a head-on PMT. The photocathode is a semitransparent alkali $Sb - K - Cs$. That material has a high sensitivity and low dark current and a blue sensitivity index matching the scintillation flashes of NaI scintillators. The diameter photocathode is 51-mm. It is composed of 12-stage of dynodes. The first dynode followed by high-stability copper-beryllium dynodes in the succeeding stages. It is highly useful for detection in extremely low-light level measurement applications in the blue region of the spectrum. Typical applications include single photon counting, pollution monitoring, radiometry, Raman spectroscopy, scintillation counting, nuclear "time-of-flight" measurements, and astronomy. Here are the key specifications of this PMT is shown in "Table 2.2"

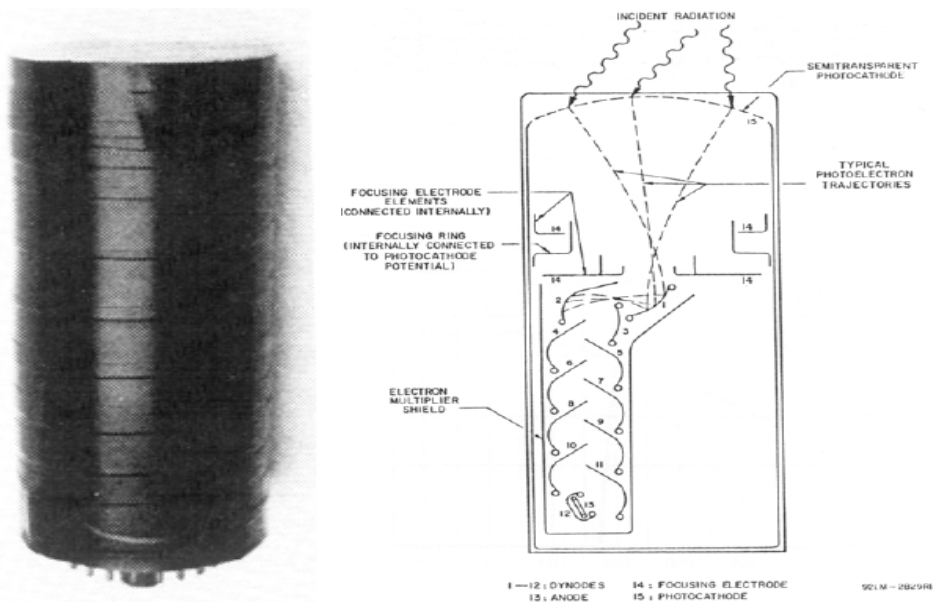


Figure 2.1.6: BURLE 8850

H3378-51 PMT Hamamatsu H3378-51 is demonstrated in “Fig.(2.1.7)” is a head-on PMT having a window of quartz. The photocathode is made of a Bi-alkali materials ($Sb-Rb-Cs$, $Sb-K-Cs$) with diameter of 50 mm. It is composed 8 dynodes. Attached is table”2.2” which shows their specifications. It is highly suited for detecting a wide range of light wavelengths due to its broad spectral response range and excellent quantum efficiency, and its quick rise time and low dark current enable high-speed and low-noise measurements. It’s also important to note that Hamamatsu, the maker of the H3378-51 PMT, provides a variety of additional features and assistance tools to make using their PMTs easier. These items include voltage dividers, preamplifiers, and signal processing modules.

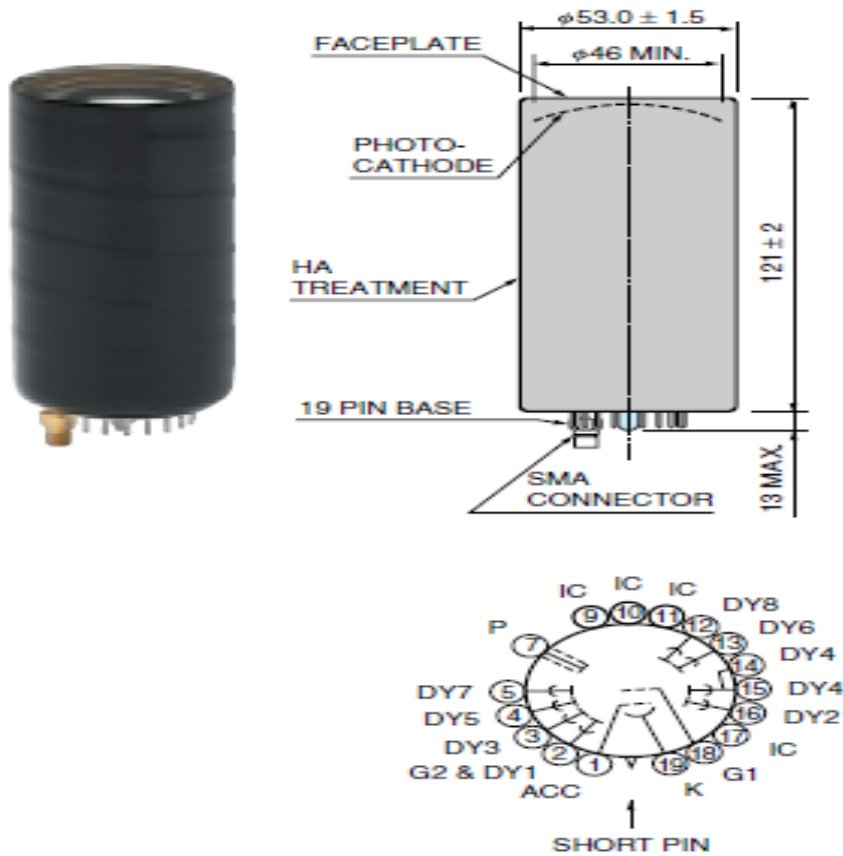


Figure 2.1.7: H3378-51 PMT

	Burle-8850	H3378-51
Spectral response range(nm)	300-650	300-650
Peak wavelength(nm)	420	420
Rise time(ns)	2.1	0.7
transit time(ns)	31	16
Anode to cathode voltage (V)	3000	3500
Average anode current(mA)	0.2	0.2
Gain(anode)	1.6×10^7	2.5×10^6
S-anode(ma/W)	1.3×10^6	2×10^5
S-cathode(mA/W)	82	80
Dark current(nA)	0.6	100
Index of refraction	1.47	1.47

Table 2.2: PMT specifications

BASE-265A

The ORTEC Model 265A Photomultiplier Base is a mechanical assembly that features a resistive voltage divider network and appropriate capacitive decoupling, specifically designed to operate 12-stage photomultiplier tubes (PMTs). This PMT Base is highly suitable for applications that require quick timing or single photon counting. The Model 265A is compatible with a wide range of 12-stage PMTs, such as the Hamamatsu R329, R1332, R1333 and the Burle

(formerly RCA) 8575, 8850, C31000M, which offer excellent characteristics for both timing and energy resolution. The PMT Base's structure maintains good pulse fidelity through a wide range of signal currents, complementing the tube characteristics. The Model 265A's main goals include achieving outstanding pulse fidelity for a variety of signal currents, a high-impedance linear signal from dynode, a timing signal from dc-coupled anode at 50-W impedance, and the ability to perform single-photon counting. Additionally, the Model 265A PMT Base includes an available magnetic shield for added convenience. The Model 265A PMT Base structure complements the tube characteristics by maintaining good pulse fidelity through a wide range of signal currents like seen in [2.1.8](#) where a negative high voltage is applied to the cathode, and the anode is operated essentially at ground potential. This facilitates the incorporation of several features that augment the fast-timing performance.

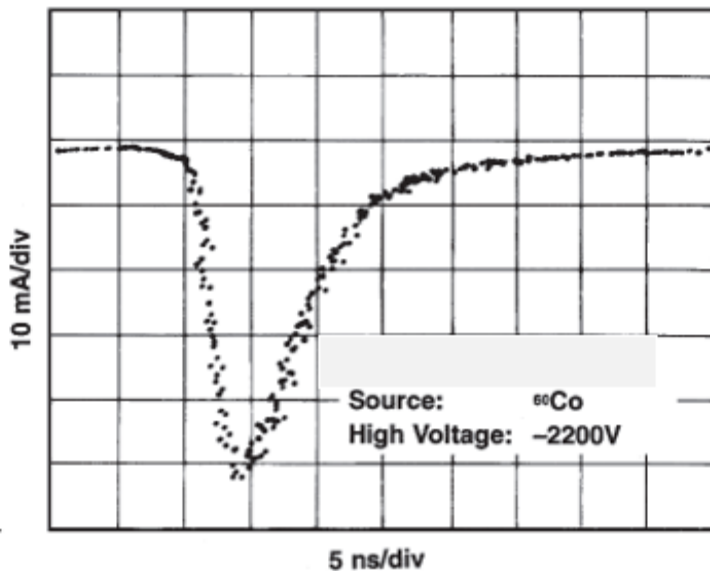


Figure 2.1.8: Typical Anode Output with a Burle 8850 PMT

In our lab, we use the following combined detectors mentioned in “Fig.([2.1.9](#))” and “Fig.([2.1.10](#))”



Figure 2.1.9: The composed detector of BC418+Burle8850+265A Base

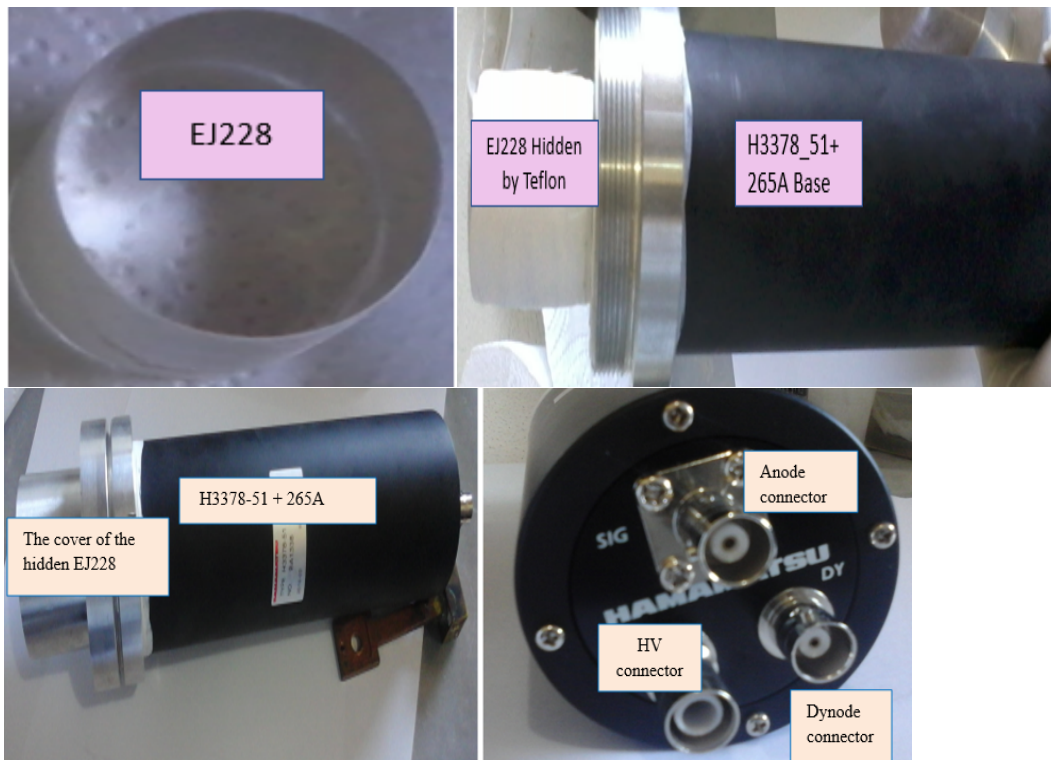


Figure 2.1.10: The composed detector of EJ228+H3378-51+265A Base

HPGe Detector

Semi-conductor detectors are a special type of ionization detector. A charged particle traversing a semiconductor produces electron-hole pairs in the band gap instead of exciting or ionizing the medium (Fig. 2.1.11). The energy required to form a pair is just about 3 eV (as opposed to 30 eV in gas for ionization). The number of electron-hole pairs increases as the radiation's energy increases. As a result, a large number of electrons are moved from the valence band to the conduction band, and a correspondingly large number of holes are produced. Germanium may completely absorb high-energy photons (up to a few MeV) since it can have a depleted, sensitive thickness of a few centimeters. By providing an electric field, the flight of electrons and holes to the electrodes produces a pulse that can be detected in the outer circuit. The energy of the radiation that was incident initially is transmitted by this pulse. The frequency of these pulses reveals information about the radiation's intensity.

Eventually, there exist detectors based on silicon. The HPGe detector is found to be the most suitable choice for accurate gamma and x-ray spectroscopy. Due to its far greater atomic number than silicon and lower average energy required to generate an electron-hole pair—2.9 eV for germanium against 3.6 eV for silicon—germanium detectors are far more effective at detecting radiation than silicon detectors. Germanium has a shorter mean free path because of its bigger linear attenuation coefficient, which is brought on by its higher atomic number. Furthermore, silicon detectors can only be a few millimeters thick. Germanium can also be utilized as a complete absorption detector for gamma rays up to a few MeV due to its depleted, sensitive thickness of centimeters. To best efficiency, the HPGe detectors must work at liquid nitrogen temperatures of $-196^{\circ}C$ since the noise from thermal excitation is excessively loud at ambient temperatures. In the lab, we had been used the HPGe Coaxial Detector System from ORTEC's GEM series, which is shown in "Fig. (2.1.13)", in the lab. A detector "capsule" containing the HPGe detector, preamplifier, and high voltage filter is connected to the appropriate cryostat in Figure "2.1.14". "Fig. 2.1.12" illustrates the configuration of the GEM Coaxial Germanium Crystal. GEM Series HPGe detectors from ORTEC are made to cover the energy range from 40 KeV and above. Peak symmetry and the good energy resolution are assumed. The Following Specifications are also assumed

- Energy resolution full-width half-maximum (FWHM) at 1.33-MeV of ^{60}Co is 1.6 KeV
- Relative Photopeak efficiency at 1.33 MeV is 24%

- Peak-to-Compton ratio at 1.33 MeV is 63:1
- Peak shape ratio for the full-width tenth-maximum to the full-width half-maximum at 1.33 MeV is 1.85
- Energy resolution at 122 keV of ^{57}Co is 687eV
- Energy resolution at 5.9 keV of ^{55}Fe is 600eV

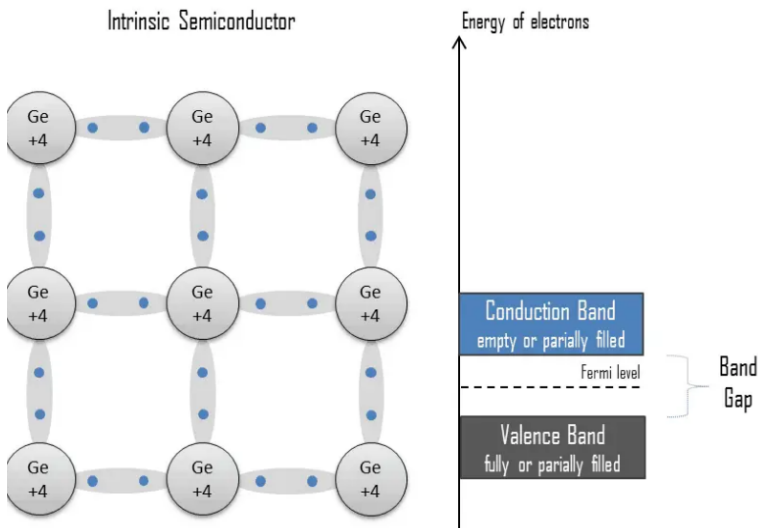


Figure 2.1.11: Ge principle of detection[4]

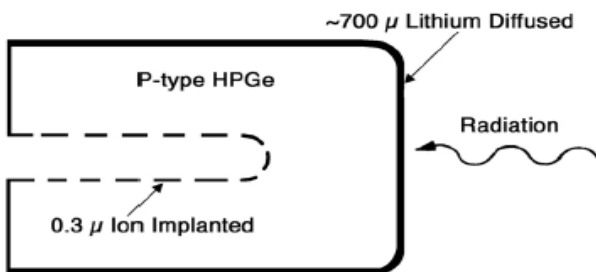


Figure 2.1.12: Configuration of GEM Coaxial Germanium Crystal



Figure 2.1.13: HPGe detector



Figure 2.1.14: Liquid Nitrogen Cryosta

2.1.3 Nuclear Instruments Modulus(NIM)

In the experiment, we make use of certain electronic modules designed to progress the signal processing. In this subsection we will show these different modulus and describe the working principle for each one.

Constant Fraction Differential Discriminator CFDD 583

This module is a Nuclear Instrument Module(NIM) type which is the first and most fundamental electronic standard, according to "The ORTEC Model 583B" documentation(Figure"2.1.15"). Its initial release dates back to 1969, and its primary function is to generate rapid time signals on a single channel by accepting negative electrical pulses within the range of 0 to -10 volts. The module operates on a basic principle that involves a discriminating process, wherein a portion of the signal is removed, and the remaining portion is converted into a logic signal. After detecting the zero crossing(T_0), the module generates an output signal as like mentioned in

Fig"2.1.16'. In the fig."2.1.17' an output pulse from the CFDD of our lab. The CF Shaping Delay is optimized for each application for better (rise time, nominal width of input signal).

The important connectors are:

- * Input (0, -10V)

- * Upper Level: single channel selector, it only accepts [-30mV, -5V] signals and transforms it into [0 - 5V] signals. In principle this potentiometer is made to determine the maximum signal threshold of entrance.

- * Lower Level: single channel selector, it only accepts signals of [-30mV, -5V] and transforms it into signals of [0 - 5V], In principle this potentiometer is made to determine the minimum signal threshold of entrance.

- * Modes of discriminators; you can switch between DIFF(differantial) and INT(integral) selection

- * Time Modes; on switch between CF(constant fraction) and SRT(slow rise time reject)

- * Delay: total delay is 0.7 ns, the module should be used with 50 ohm cable.

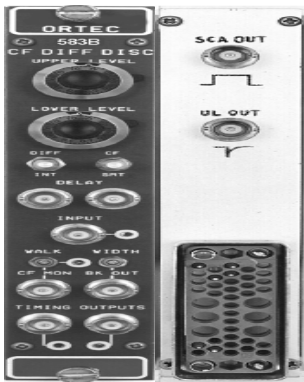


Figure 2.1.15: CFDD Model 583B

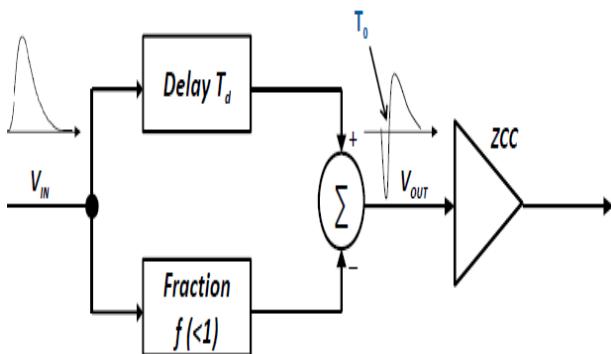


Figure 2.1.16: CFDD principle



Figure 2.1.17: CFDD output signal

Time Amplitude Converter TAC

The ORTEC Model 567, Time-to-Amplitude Converter/Single-Channel Analyzer (TAC/SCA) shown in fig' [2.1.18](#)' performs single-channel analysis of the analog signal and detects the time gap between start and stop input pulses. It then generates an analog output pulse proportional to the measured time. In our case, we have been used as a TAC not as an SCA. When a signal enters the TAC, a capacitor gets charged. As soon as the succeeding signal arrives, the capacitor stops charging, and a pulse is created with an amplitude proportionate to the charge on the capacitor. The minimal restriction on the Start-to-Stop conversion time is $5ns$. We can modify the range from $50 - 200ns$ using the Range connector on the front panel.

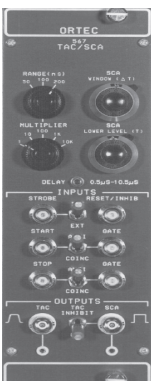


Figure 2.1.18: TAC/SCA 567

Multi Channel Analyser (MCA)

In its simplest form, an MCA is a device that counts and sorts events in real time. These events are sorted according to one or more of their characteristics, and for the purpose of counting, the events are compiled into channels. Pulse-height analysis (PHA) is the most prevalent and the form of multichannel analysis that nuclear spectroscopists are most interested in.

The term "PHA events" describes signal pulses that come from a detector. The pulse height or voltage, which is directly related to the particle or photon's energy. Each pulse is converted into a channel number via an analog-to-digital converter (ADC) in order to make analysis easier. As a result, only a limited range of pulse heights or voltages are represented by each channel.

The Multichannel Analyser (MCA), which receives pulses sequentially, builds up a distribution in its memory that links the quantity of pulses to each pulse's corresponding pulse height. The count of pulses with comparable, though not necessarily identical, heights is stored in each memory location, which corresponds to an ADC channel, to illustrate this distribution.

The distribution indicated previously, arranged in ascending order of energy, is referred to as a spectrum. The acquired spectrum must be available for analysis and/or storage in order for it to fulfill its intended function. The way it is commonly displayed is on a graph, where the vertical axis denotes the quantity of pulses at each height and the horizontal axis the height of the pulse. A histogram is the name given to this graphic representation.

2.2 Positron Annihilation Spectroscopy Methods

2.2.1 Positron Annihilation Lifetime Spectroscopy (PALS)

R.E.Bell and R.L.Graham(1953) published the first comprehensive analysis of the lifetimes of positrons in solids and liquids[83]. They made the evidence that in metals and crystalline solids, positrons annihilate with a single mean lifetime ($\tau_1 = 0.150 - 0.200\text{ns}$). This brief lifetime appears to be almost independent of the specific material utilized, which has been historically reliable. Additionally, they observed the lengthier o-Ps component, which is at that time unknown, in some amorphous non-metals and in the majority of liquids. However, they did not understand how thermodynamically sensitive this component is to temperature and order-disorder in solid materials[84].

PALS (positron annihilation lifetime spectroscopy) bases its measurements on the duration

of time the positron has been present in the sample. In our lab we use the ^{22}Na positron source, which is the most common source (cheaper, easy to handle and its half-life is 2.6 years). The schematic of its decay Fig."2.1.1" illustrates how can simultaneously emit a positron and a gamma photon with a 1.28 MeV energy. Then, we consider the detection of a 1.28 MeV gamma photon as the birth of a positron (although in practice, this photon is emitted after a few picoseconds of the positron's decay) and the detection of one of the gamma photons of 0.511 MeV of annihilation the death of positron as like simply illustrated in the Fig" 2.2.1"

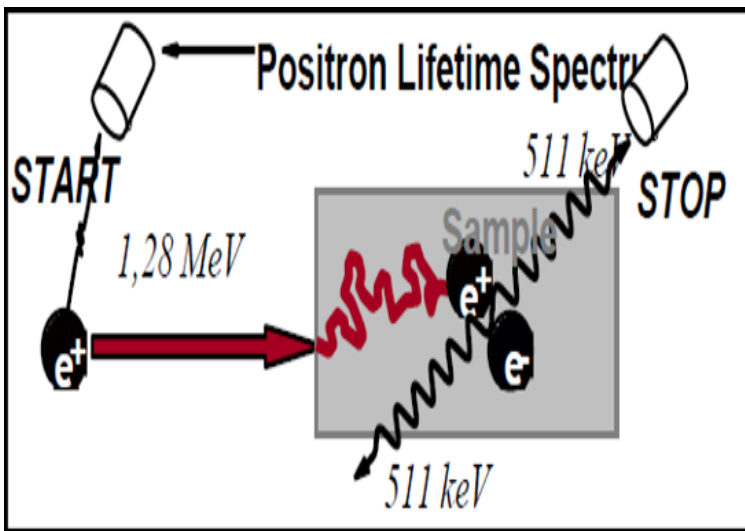


Figure 2.2.1: PALS basic principal

The figure"2.2.2" shows the apparatus used in our lab of positron te setting-up the PALS spectrometer.

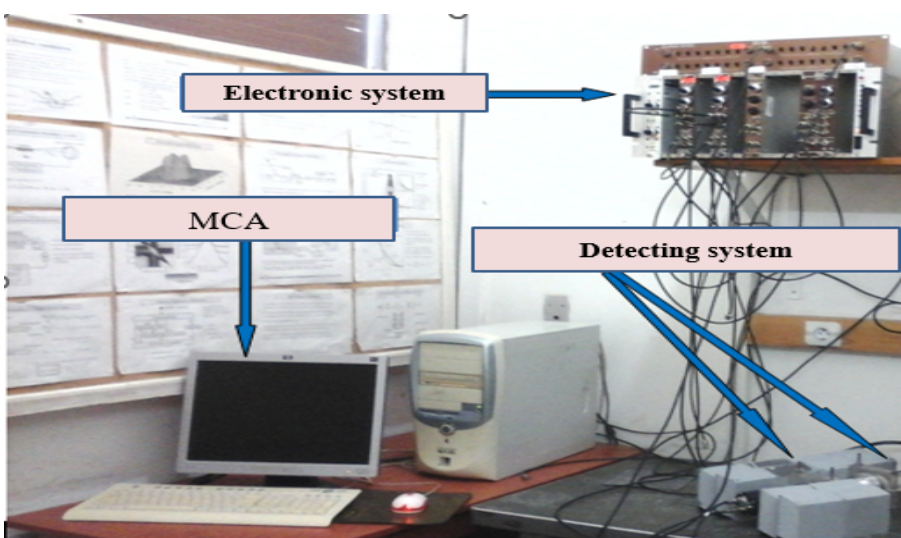


Figure 2.2.2: PALS devices

It is made of

* Two detectors arranged in pi geometry as like proved in “Fig. 2.2.3”

*Electronic system which is composed of: two CFDD, TAC, Amplifier, generator and a delay box as like demonstrated in “Fig. 2.2.4”

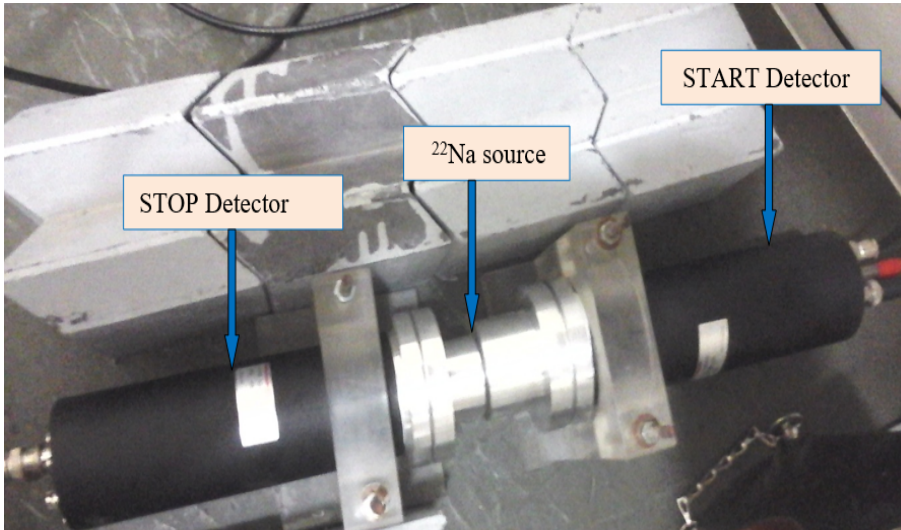


Figure 2.2.3: Detecting system

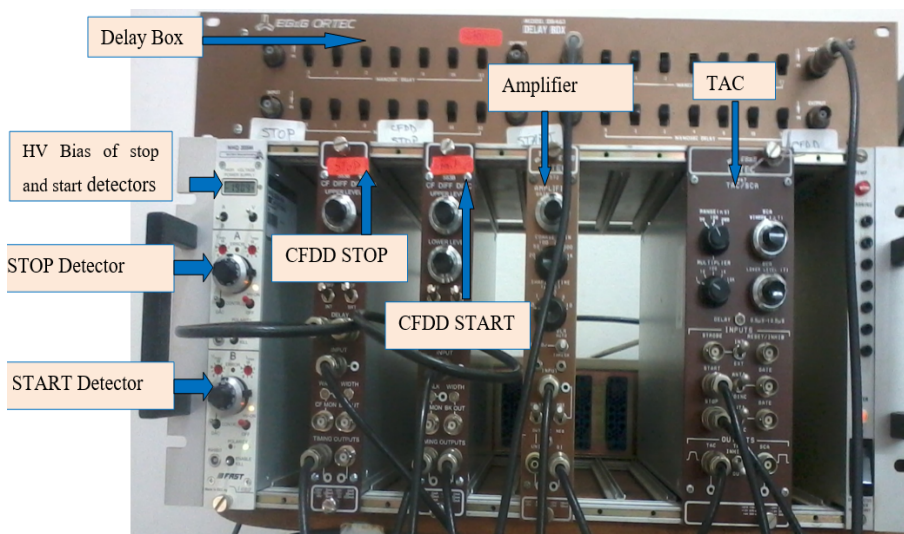


Figure 2.2.4: Electronic system

The final device is the acquisition system, MCA which is a card of the Maestro MCB25 type (Ortec), which is built into a microcomputer, collects the pulses at the time-amplitude converter’s (TAC) output. They are organized and saved in channels with a width of t_0 , according to their amplitude, to create a lifetime spectrum. Thus, the n_{th} channel is equal to the quantity of positrons with lifetimes between n and $(n + 1)t_0$. The time per channel, or t_0 , is unique to each lifetime system. The measured annihilation times of individual positrons

within a material are captured in a histogram, PALS spectrum. It thus represents a decay curve, designated as $y(t)$. Each of the exponential decay components that make up this decay curve has a unique lifetime (τ_i) and intensity (I_i). Different positron-states, such as the $p - Ps$, free positron, or $o - Ps$ may decay and develop in network structures. Knowing that each component spectrum reflects the annihilation rate probability in a special condition, which relates to such quantifiable information. The decay curve as a spectroscopic output must be convoluted with the instrumental resolution, (R) that specifies the detection system and affected by experimental noise (B).

$$y(t) = R(t) \otimes \sum_i I_i e^{-t/\tau_i} + B \quad (2.2.1)$$

A PALS analysis program's main goal is to solve the inverse problem of obtaining the lifetimes and relative weights. Direct deconvolution of the spectrum or the fitting of a theoretical model to the experimental data are two methods that can be used to accomplish this. The direct deconvolution method is used by a number of existing applications, including CONTIN[85] and MELT[86]. Whereas, the model fitting have been used in programs like POSITRONFIT[87], RESOLUTION[88], PALSfit[89] and LT.9 [90]. Mathmatically, the inverse problem is one of the most complicated tasks[91]. For that, the based algorithms consists of some useful strategies like the Maximum Entropy principe[92] which is used in MELT program. The preference for smooth solutions is another fundamental principle used in CONTIN program. The concept permit the generation of continuous and smooth solutions during the deconvolution process, improving the outcomes' interpretability. Using a specified model, such the ELTA (Empirical Lifetime Transform Analysis) which is a model was specifically developed[93] to fit polymer spectra taking into consideration their distinct properties. Programs like POSITRONFIT and LTv9 based upon models works with a set number of components. The analysis process is simplified and made more effective by these tools. Recently, given the rapide developement of AI tools of training and deconvolution nuclear data, we find researchers as Petschke(2019)[94] used an AI based methods to fit experimental positron annihilation data.

Along our thesis we use the LT.9.2 program to fit the PALS spectra. LT.9.2 is a model fitting based program. The code essentially fit the experimental data on the following function [2.2.2](#): S which is defined as a linear combination of exponential lifetime components

$$S(t) = \sum_i \frac{I_i}{\tau_i} \exp\left(-\frac{t}{\tau_i}\right) \quad (2.2.2)$$

From the experiment, we obtain a spectral data y_{ex} , in reality, it is convolution of the theoretical function Eq. 2.2.2' with the resolution function R .

$$y_{ex}(t) = \int_0^\infty R(t - t_0) S(t_0) dt_0 \quad (2.2.3)$$

2.2.2 Doppler Broadening Spectroscopy (DBS)

Using a Ge(Li) detector, the doppler broadening of the annihilation radiation line resulting from the motion of the electron-positron system has been seen. In comparison to a gamma ray of equivalent energy, the linewidth of the annihilation radiation is around twice as large.

Let's take a more basic look at the scenario where the electron-positron pair is travelling with momentum p prior to annihilation. Then, when the annihilation happens, one quanta is released in the direction of p . The detection will be carried out using a *Ge(Li)* detector. Although only the momentum component in the direction of the detector is taken into account, it is the only one that influences the energy of the quanta to first order. Therefore, the photon energy that was released in the other direction has been detected.

Given the requirement for energy and momentum conservation in the direction of p , we write :

$$2mc^2 = h\nu + h\nu' \quad (2.2.4)$$

$$p = \frac{h\nu}{C} - \frac{h\nu'}{C} \quad (2.2.5)$$

where m is an electron's rest mass. The pair momentum may be expressed in terms of the difference in the observed energy $h\nu$ and the energy $h\nu_0 = mC^2$ as like:

$$p = \frac{2(h\nu - h\nu_0)}{C} \quad (2.2.6)$$

As a result, the distribution of the number of electrons with a certain momentum component parallel to the direction of emission of an annihilation quantum is the same as the distribution of the number of annihilation events in photon energy. The resultant line-width of the annihila-

tion photon has been exploited to create a positron spectrometer, whose application to defects studies has been treated at the first time by Hurley(1968) and by Rama Reddy(1970)[95]. The longitudinal Doppler shift of the radiations is detected, whereas the transverse shift is often measured by angular correlation tests. Using a computer software program, the momentum distributions production had been verified that agree with those had been published. Theoretically, the annihilation photopeak's Doppler broadening provides the same details about the distribution of electrons in the material where the annihilation originates as can be learned from measuring the angular correlation of the two quanta. DBS has been employed to characterize the dislocations in pure copper and in the aluminum alloy[96]

Along our thesis we had been used a DBS spectrometer demonstrated in the figure"2.2.5" which is made of the following components: HPGe detector, Amplifier, generator and MCA to collect the spectra.

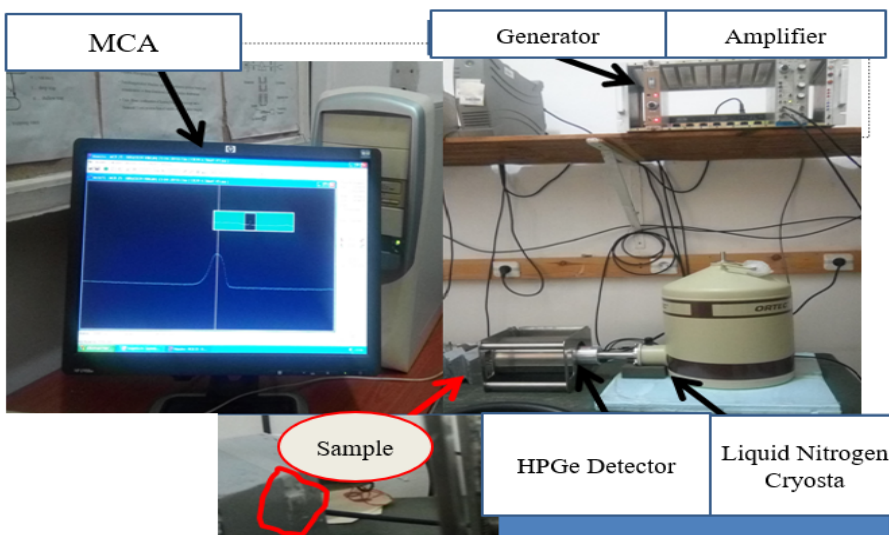


Figure 2.2.5: DBS spectrometer

511 KeV peak, is doppler broadened by the longitudinal momentum of the annihilation pair. Since the positrons are thermalized doppler broadening measurements provide information about the momentum distribution of electrons at the annihilation sites.

The characterization is well established via the parameters of shape, S (shape parameter) and wings, W (wing parameter) which are demonstrated in Fig"2.2.6". S is expressed with the ratio of the centered integrated area upon the full integrated area of the 511KeV energetic spectrum. Whereas, the W parameter is the ratio of counts in the off-center fraction divided by the entire area of the annihilation line.[28].

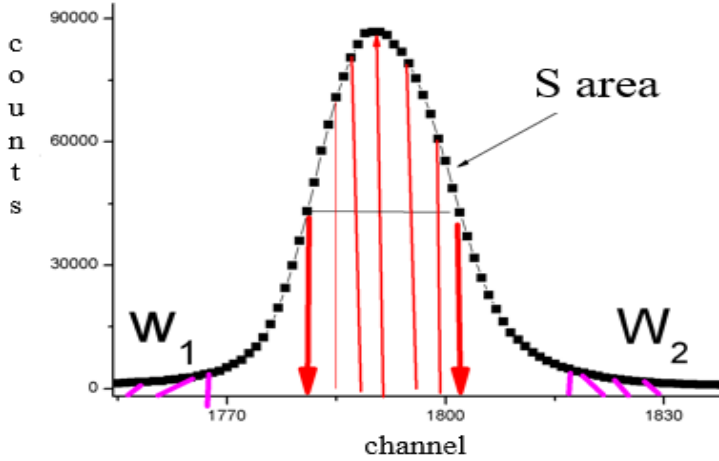


Figure 2.2.6: S and W parameters

The fit of the DBS spectra is well realized by using the SP program written from the part of J. Dryzek[97]. It has an easy implementation and automatically calculates the S and W parameters by deducting the background. The based algorithm can fit a gaussian curve to the spectrum and the position of the maximum of the gaussian curve matches to the $511keV$ position. Determining the integration ranges for the S and W parameters in the analysis depends on this position. The S parameter with values up to 0.5 is sensitive to the annihilation with low momentum valence and unbound electrons. The middle portion of the peak is raised, increasing the value of the S parameter as a result of annihilation with low momentum electrons that are also present in the open volume defects. When there are more imperfections where positrons might be localized, the S parameter rises. When there are more annihilation events involving core electrons, the W -parameter's value rises because it is more sensitive to the annihilation site's chemical environment than the S -parameter is. Momentum core electrons are mostly responsible for the energy area between $(511 \pm 5) keV$ and above.

2.2.3 Variational Energy Positron Annihilation Spectroscopy (VEPAS)

When we employ heigh energy radioactive source for positron annihilation spectroscopy, the depth of annihilation gamma is greater than $540\mu m$. Therefore, the moderation of the positron's energy is needed if we want to characterize the surface. VEPAS (Variational Energy Positron Annihilation Spectroscopy) is what we dubbed it.

Madanski and Rasetti, 1950[98] they were the first that realized the limitation of energetic positron in surfaces implantation. Then, Cherry (1958)[80] has been observed the moderated

slow-positron emission, with an efficiency of 10^{-8} . After that, both Groce et al. (1968) and Costello et al. (1972) [81] provided experimental evidence of efficient (10^{-7} - 10^{-6}) creation of slow (eV) positrons. Another evidence of energy moderation had been realized in 1970's closing years when Mills, 1978 [99] and Lynn, 1979 [100] arrived to manipulate surfaces as moderators.

The moderation of the host positron spectrum to monoenergetic beam is done by using special type of thin films because it posses a positron negative work function, or the amount of power needed to remove a positron from the bulk and place it outside the surface dipole. It is predicted by Tong (1972) [101], who first discovered the relevance of the dipole contribution. Hodges and Stott (1973b) [102] then adjusted this model for positron-electron screening.

In fact, tungsten thin films, W(100) are almost always used as a moderator in positron laboratories because it has a negative work function of -3eV as mentioned in "fig. 2.2.7" which allows the reemission of 0.05% of positrons with kinetic energy of 3eV . To maximize the incident positron flux, the moderator's characteristics are crucial. For this, a heat treatment at high vacuum (10^{-7} mbar) and at a temperature of 2000°C is required for tungsten moderators in order to remove the defects and avoid the incorrect informations.

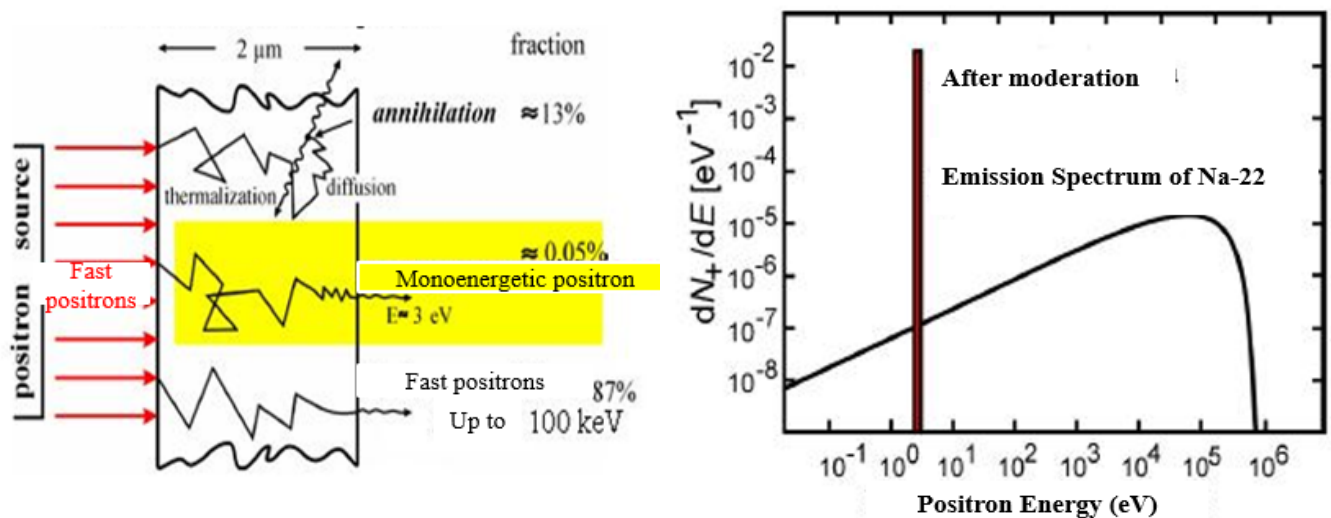


Figure 2.2.7: Tungsten work function

Nevertheless, there is another type of moderator that is highly effective and is based on the creation of crystal from a rare gas (Ne) [5]. By lowering the temperature at 5°K in vacuum (10^{-10} mbar), crystal formation is achieved. This improved moderator generation allowed for the production of 10^6 positrons per second of flux.

The outcome of positron interaction with the neon solid is demonstrated in the Fig." 2.2.8" which presents the probability yields versus the implantation energy for a thick sample of Neon.

The band gap E_g , the exciton threshold E_x , and the inelastic threshold E_{th} are all indicated. The probability is practically unity between 2 and 10 eV, drops drastically at $E_{th} = 16\text{eV}$, and suddenly rises between $E_x = 17.5\text{eV}$ and $E_g = 21.5\text{eV}$, as seen in the figure. Due to the implanted positron's rapid diffusion rate and low loss rate for energy below E_{th} , it is quite likely that it will escape from the solid. Just below E_{th} , there is a probability production of positronium. The binding energy of positronium, E_b , is related to the positron work function, ϕ_+ , E_g , and E_{th} by the formula [2.2.7].

$$E_b + \phi_+ = E_g - E_{th} \quad (2.2.7)$$

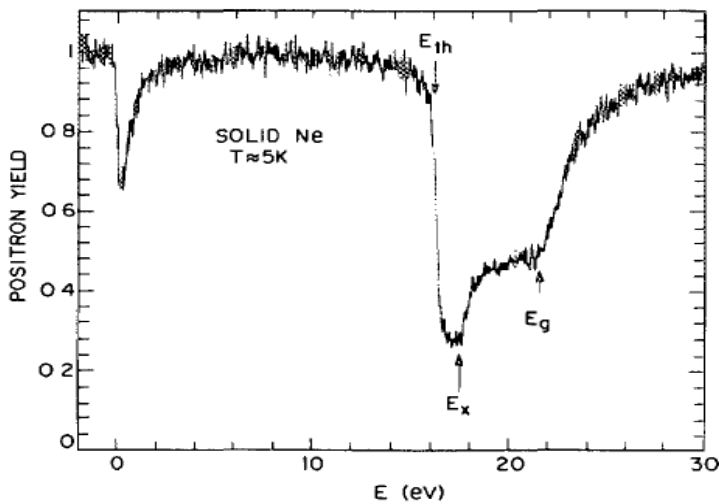


Figure 2.2.8: Monoenergetic positron re-emission probability for solid Neon [5]

The distribution of the energy spectrum of the positrons released from a rare gas solid should range from zero to E_{th} and be influenced by the initial distribution of positron energies immediately before they reach the inelastic threshold energy E_{th} .

A new method for studying solids with positrons has emerged, emphasizing the surface and near-surface regions that were previously only indirectly accessible due to the high efficiency of conversion from the continuous positron energy spectrum to monoenergetic beams.

During our thesis we had benefited an internship period with our colabaratory colleagues in Turkey, where they have a positron lab contains a VEDBS system.

The accelerator there as shown in Fig [2.2.9] is set up differently from other accelerators that are currently in use in European labs. The idea of moderation, the slow and rapid positron

separation system, and the acceleration system are what make the difference. The dimension is not exceeding 1m 50 cm.



Figure 2.2.9: The positron accelerator of Marmara University

The main constituents of this accelerator are:

- A moderator crystal growth chamber housing the ^{22}Na source of an activity of 50mCi with a shielding in lead balls.
- Pre-acceleration part with a negative voltage of -25 V for a pre-acceleration of positrons.
- System formed from an electric and magnetic field combination ($E*B$) for the elimination of fast positrons.
- A magnetic guidance system along the accelerator tube. An accelerating part located in the jet chamber (near the measurement sample door).
- Helmholtz coils surrounding the reaction chamber and which are used to focus on the positron beam.
- Board of reaction housing "flat microchannel" for the measurement of life time.
- A vacuum system made up of ion pump, molecular turbo and membrane.
- Detection system (Ge (Li) and Hamamatsu detectors) for measurement of positron annihilation lifetime and Doppler broadening with electronics modulus made up of CFDDs.
- Micro computer with a Maestro type acquisition card.
- System control is done via software made on LabVIEW.

Specific technical characteristics of the positron accelerator

1-Positron Moderator System (RGM-1) Positron beam systems, with an output of up to to 10^7 positrons per sec., include equipment for producing solid neon moderators, radiation shielding for sources of up to $50mCi$ (^{22}Na), magnetic beam transport, and fixturing for loading and unloading source capsules with minimum radiation exposure as shown in Fig"2.2.10". The system is delivered with all required vacuum equipment, magnetic field coils, computer control system etc.

- The positron beam performance:

- High efficiency: 8 million positrons from $50mCi$ ^{22}Na
- Narrow energy spread, typical $1.7eV$ as shown in Fig"2.2.11"
- Moderators grown automatically under computer control (Labview interface, source code supplied)

• Simple installation of radioactive source using supplied handling tools.

- Features:

- Moderator material: Solid neon
- Moderator temperature: 7-8.4 °K
- Beam transport: Magnetic
- Source shielding: in vacuo: Elkonite external: lead shot
- Separation filter: Magnetic deflection
- Moderator diameter: 8 mm
- Beam diameter: <3mm (depending on B)
- Positron flux: 8 million/sec
- Energy spread: 1.4-2.5 eV (1.7eV typical)
- Moderator decay rate: <4% per day as clarified in Fig"2.2.12"
- Moderator regrowth time: <20 min total
- Vacuum pumping: 100 l/sec ion pump molecular drag pump
- Sizes 150x130 cm

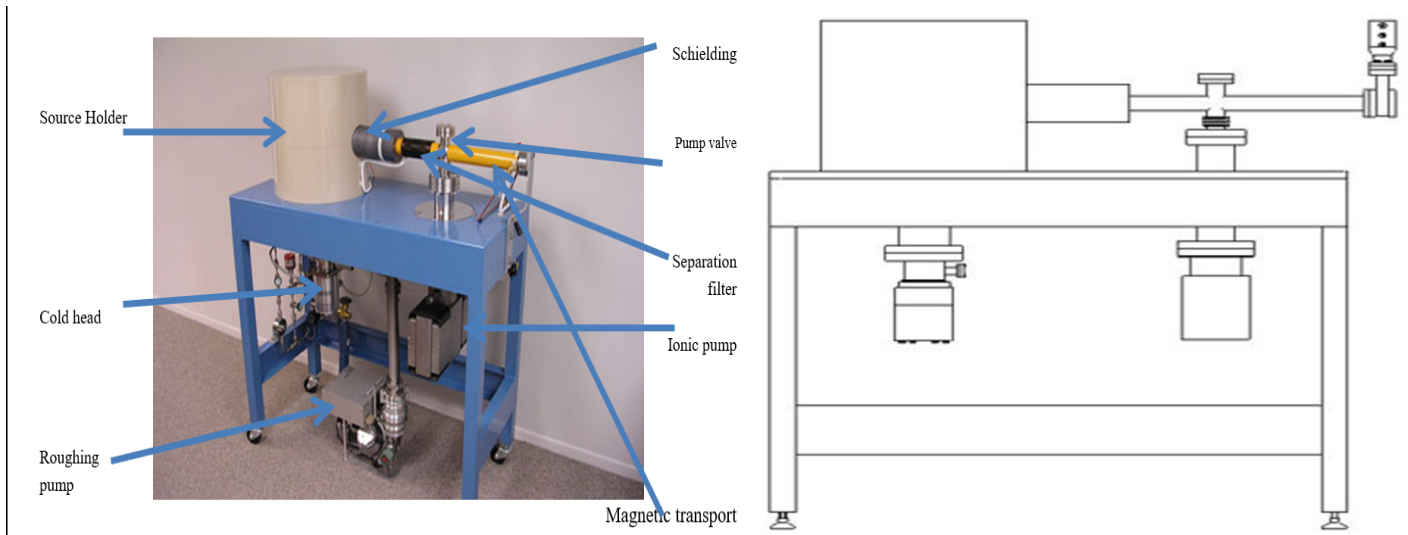


Figure 2.2.10: Positron Moderator System

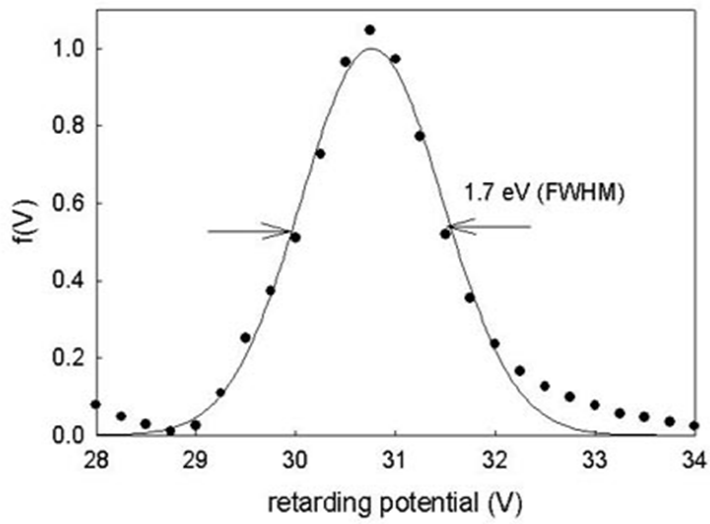


Figure 2.2.11: Energy Distribution of positron from the moderator. Narrow Energy Spread: 1.7 eV (FWHM)

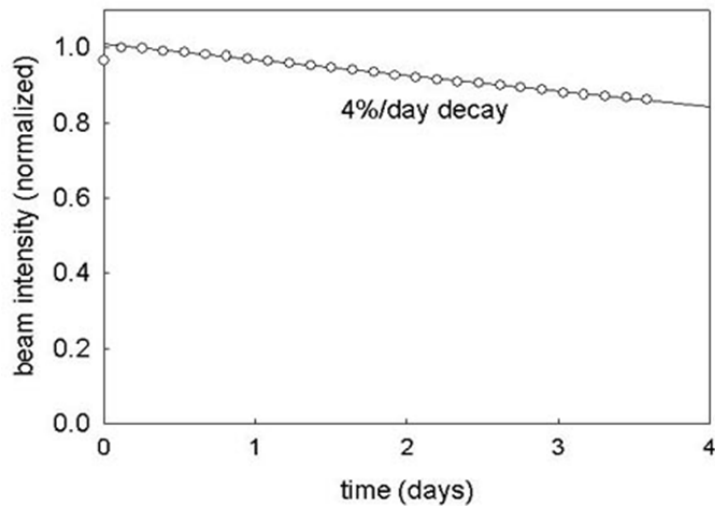


Figure 2.2.12: Long moderator lifetime: 4% per day decay

2. Sample Chamber (TS-1) Sample chamber (TS-1) was designed for Doppler-broadening spectroscopy in conjunction with a suitable magnetically guided slow positron beam source such as the RGM-1. The TS-1 is shown in Fig"2.2.13" and is supplied with all required power supplies and vacuum instrumentation. Specifications are as follows:

1. Chamber: stainless steel, metal sealed using Conflat flanges.
2. Primary pump: 60 l/s ion pump.
3. Roughing pump: molecular drag/diaphragm pump.
4. Magnetic field: 1 par of Helmholtz coils up to 90 gauss.
5. Base pressure: < 10⁻⁹ torr.
6. Sample bias: up to 30 kV
7. Sample introduction: load lock using modular sample holder.
8. Footprint: 60 x 130 cm

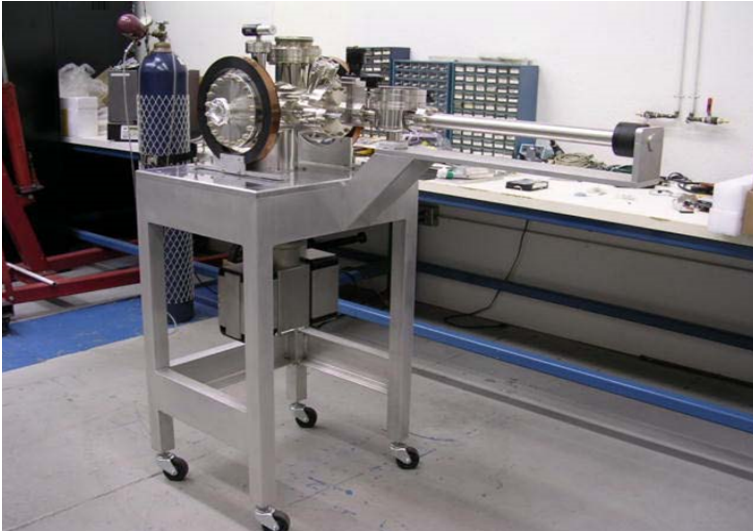


Figure 2.2.13: Overview of the TS-1

Figures' [2.2.14](#), [2.2.15](#)' displays the demountable sample holder and a close-up of the high voltage feedthrough respectively.



Figure 2.2.14: Close up of the load lock, showing the demountable sample holder

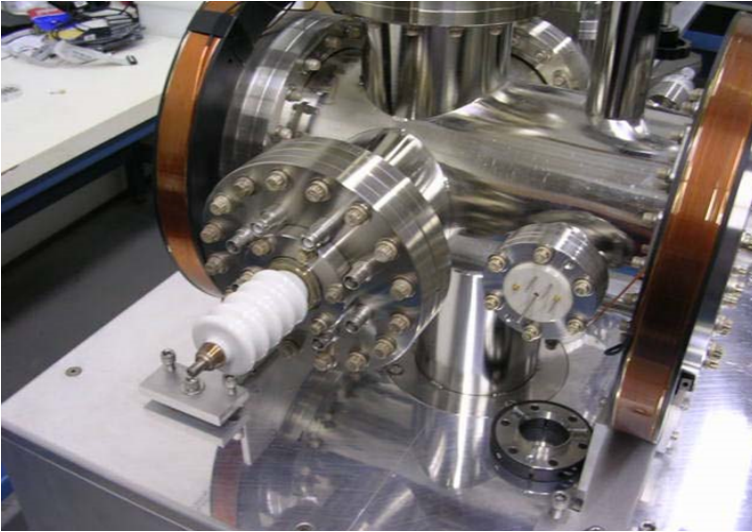


Figure 2.2.15: Close-up of the high voltage feedthrough

Since the first publication highlighting the capability of PALS to reveal the microscopic structure of materials [103], it has been recognized as a powerful nuclear probe technique. PALS has proven to be especially useful for examining the atomic and molecular level structural characteristics of materials. PALS sheds light on the electron density distribution, free volume, and defect-related phenomena in diverse materials by examining the annihilation times of positrons. Additionally, DBS could be used to comprehend the chemical structure. Through the use of positrons with different energies [24] [28], VEPAS is also useful for researching the characteristics of thin films, which are essential for numerous technological applications [97]. PALS assists in characterizing point defects, impurities, and their consequences on electronic behavior in semiconductors [104]. The microstructural characteristics of metals [105], such as grain boundaries, dislocations, and defects, which are essential for comprehending their mechanical and electrical properties, have been thoroughly examined. PALS has also been used to examine the free volume and structural changes in polymers, providing information about their mechanical and physical characteristics [21] [9].

Conclusion

This chapter presents a comprehensive discussion of the fundamental concepts that underlie the use of positron properties in monitoring strategies. PALS, DBS, and VEPAS, the three spectroscopies previously addressed, all rely on the detection of gamma radiation injected in the samples. Numerous articles in the literature demonstrate how well these techniques work for identifying a wide range of materials, including metals, semiconductors, and polymers. These methods have been extremely helpful in revealing information on the microstructural

characteristics, defects, and electronic structure of these materials. The chapter ends with a summary of the key concepts and principles related to the use and application of PAS types. These summaries can be used as a guide while setting up and running experiments that make use of different PAS methods.

Chapter 3

The Solid State Nuclear Track Detector of CR39-Art state

Introduction

It has been well proved that the structural, optical, chemical, electrical properties of CR39 could be modified under irradiation. Different kinds of irradiation had been realised towards the examination on how the CR39 could be exploitable. The study of CR39 capabilities is achieved via the monitoring of induced damages evolution. This monitoring will allow us to know the profile of the tracks. Then, the use or a characterization technique could be documented. In that chapter, why and how different irradiations could affect the polyallyl diglycol carbonate will be resumed. We are starting by defining the CR39 as a solid state nuclear track detector and show the reason beyond what it has been manufactured. Then, we detailed the study about the nuclear tracks concepts and their history. Latent tracks and etched tracks which are the kinds of tracks have been well explained in that chapter. The different characterization techniques of the tracks have been listed. As like the positron annihilation method has emerged as the unique probe which is capable of providing the microscopic hole (a few Angstrom in size) properties directly, we provide a succinct summary of current knowledge on the PAS study of free volumes. By assessing chemical and molecular changes, we could quantify nuclear tracks which permits the characterization of CR39. This rich array of analysis techniques enables researchers to gain a comprehensive understanding of nuclear track perturbations.

3.1 What is CR39 ?

CR39 is one of the most important solid state nuclear track detector (SSNTD) in radiation physics since its manufacturing in 1978. The SSNTD cannot be discussed without referencing D. A. Young, 1958 when he discovered that after being treated with chemical reagent, LiF crystals

attached to Uranium foil displayed a number of etch pits which is completely in accordance with the anticipated number of recoiled fission fragments. Then, Silk and Barnes on 1959 observe directly the damaged regions in mica using TEM, the figure”[3.1.1](#)”, illustrates a few of the tracks[\[6\]](#). R. L. Fleischer, P. B. Price and R. M. Walker during the 1960, developed the technology’s broad advancement, extending Young’s etching approach to mica and a range of other materials, including glasses, polymers, and different minerals crystals and they arrived at a generalization of the track etching protocol[\[106\]](#). The tracks could only be generated in electrical insulators or semiconductors, and they were only produced by highly ionizing particles (alpha for polymers and fission fragments for crystals). In situations like light or high radiation doses, they remain stable[\[107\]](#). These detectors were quickly adopted in a wide range of areas because to their robustness, simplicity, and specialized nature of response.

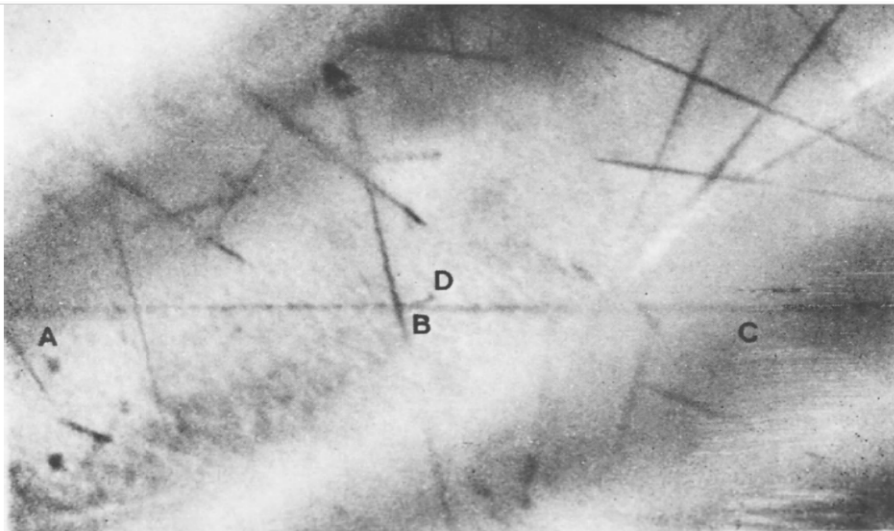


Figure 3.1.1: First Tracks observation [\[6\]](#)

We must now examine the various SSNTDs that were available if we want to comprehend why the CR39 was created. In fact, it appears that the previously developed SSNTD has inhomogeneous and anisotropic physical characteristics(see [\[7\]](#)). Variations in sensitivity and bulk-etch rate between surfaces (of the same sheet) and a non-geometrical holes are formed[\[108\]](#).

CR39 is representing the 39th formula of a thermosetting plastic developed by the columbia resins project in 1940. Chemically known as Polyallyl Diglycol Carbonate, which is produced when the monomer of Allyl Diglycol Carbonate is polymerized. The monomer has the following structure, $C_{12}H_{18}O_7$ [\[109\]](#). The generation of the CR39 monommer was well assumed using Gaussian 09 software as demonstrated in the Fig”[3.1.2](#)”and their properties are tabulated in the table” [3.1.3.2](#)’[\[110\]](#) [\[111\]](#)

Nbr of atom	Atom type	Mulliken atomic charge
1	O	-0.628369
2	C	-0.125016
3	H	0.271703
4	H	0.212481
5	C	-0.109963
6	H	0.219541
7	H	0.262141
8	C	-0.139436
9	H	0.231630
10	H	0.252901
11	C	-0.140804
12	H	0.250693
13	H	0.253973
14	O	-0.649770
15	O	-0.651007
16	C	1.107692
17	C	1.109614
18	O	-0.579651
19	O	-0.595988
20	O	-0.664688
21	O	-0.665832
22	C	-0.128024
23	H	0.264175
24	H	0.253061
25	C	-0.132153
26	H	0.246869
27	H	0.259965
28	C	-0.236231
29	H	0.248112
30	C	-0.228416
31	H	0.24437
32	C	-0.438413
33	H	0.205966
34	H	0.227262
35	C	-0.418674
36	H	0.194854
37	H	0.215429

Table 3.1: Mulliken atomic charges

Charge	0.0000 electrons
nuclear repulsion energy .	1544.5883381223 Hartrees
E(RHF)	-983.232851504
Electronic spatial extent (au): $\langle R^2 \rangle$	6247.8406
electrons Dipole moment (field-independent basis, Debye)	X= 0.4142 Y= 1.0306 Z= -1.6609 Tot= 1.9981
Quadrupole moment (field-independent basis, Debye-Ang)	XX= -137.5992 YY= -120.9077 ZZ= -108.0010 XY= 19.1848 XZ= 1.5072 YZ= 3.2134

Table 3.2: Electronic properties of the CR39

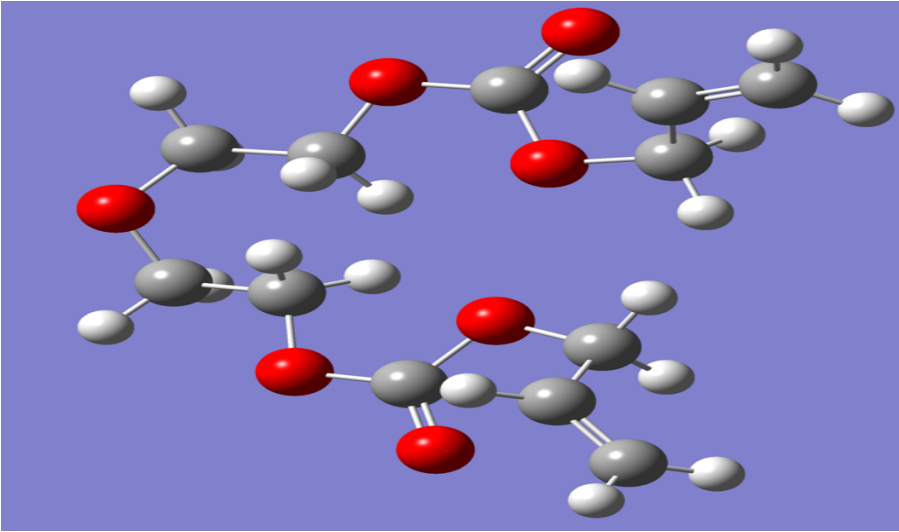


Figure 3.1.2: CR39 monomer

The two allyl functional groups enable crosslinking and polymerization of the monomer, resulting in a thermoset plastic as opposed to a thermoplastic. In addition to dissolving in specific solvents and having weaker macromolecular connections than other materials, thermoplastics can alternately become firmer on heating and softer on cooling. Thermoset polymers, on the other hand, are notable for being hard insoluble in all solvents (with little swelling), and infusible. It satisfies the requirements of optical transparency (it is really used to make inexpensive eyeglass lenses), high isotropy and homogeneity, exceptional sensitivity to radiation (including alpha, proton, even gamma radiation, and neutrons), and high stability([108]).

3.2 The Nuclear Tracks

Charged particles that move through the CR39 chains release their energy through the ionization and/or excitation of electrons. This procedure takes 10^{-18} sec to be completed[112]. The energy imbalance could then result in the creation of novel chemical species through processes like chain scission or cross-linking [113]. As a result, tracks are created along the trajectories of the particles. The tracks is made of as a new chain ends and other chemically reactive locations. The damage to the crystal is a continuous disorder made up of interstitial ions or atoms and unoccupied lattice spaces as like be shown in Fig"3.2.1"

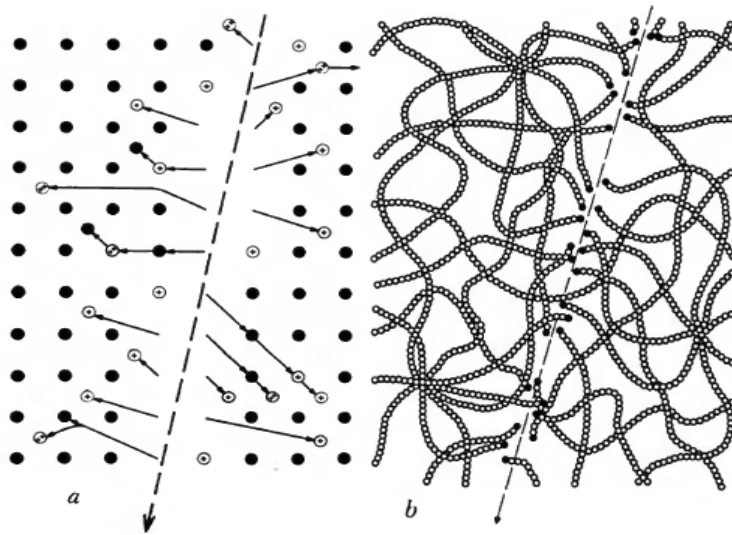


Figure 3.2.1: The atomic nature of a particle track in (a) a crystal and (b) a polymer [7]

Many models, concentrating on the understanding of how energy is dispersed within the electronic system and communicated through atomic movements, have been created to explain the generation of these nuclear tracks. The ion explosion spike model, thermal tip model, and the theory of secondary electrons (Delta electrons theory) are among the examples of these models [114]. The Delta electrons hypothesis is regarded as the best model for polymers like CR39.

Delta electrons theory

Katz initially presented the delta-ray theory of track formation [115] [116] [117] [118] [112]. Based on the following main assumption, this theory seeks to explain how tracks form: Ionization happens in tow steps. First, through a process of primitive ionization and electronic excitation, charged particles distribute a portion of their energy to neighboring atoms along their path. Delta electrons are ejected as a result of this primitive ionization, and they move perpendicular to the path of the particles. Through further electronic interactions with distant electrons outside the path of the particle, these delta electrons can subsequently transfer their energy. The ability of the delta rays theory to accurately reproduce the dose distribution around the path's particle has been well established. In fact, the trajectory of the particle will be surrounded by primary electron energy loss in only a few angstroms. However, secondary electrons move the energy a few microns further from the path of the particle. The approach simulates the local dose distribution as a function of the radial distance, allowing us to estimate the track core radii where the radiation damage dose reaches its maximum value. Katz and Kobetich developed

their model based on the delta function that limits the number of hits that are included. The hit is the quantum that is reflecting the interaction rays-sensitive element [119]. The sensitive element may consist of aggregates, molecules, or atoms that are embedded in a matrix. The density of all hits is measured by the energy deposited per unit volume. The probability of creating a hit is described by the following Poissan formula :

$$P = 1 - e^{-D_r/D_r^{37}} \quad (3.2.1)$$

where D_r^{37} is the dose that does not influence 37% of the sensitive components. The probability looks like $1 - e^{-SD}$ where D is the particles beam and S is the probability to have one hit in volume unit. The approach is based on the following assumption :

1- The ion is contained in a cylindrical shell that surrounds the ion path, and their volume is $V = 2\pi T x dx$.

2- The ions as like are constant.

Hence, the delta electrons, $D(\delta)$ is distributed randomly upon all the shells. The number of the hit in the shell in volume unit could be expressed like :

$$d\Pi = (2\pi T x dx)(N_0)[1 - \exp(-D_\delta/D_{37})] \quad (3.2.2)$$

Then,

$$S = \frac{\Pi}{N_0 T} = 2\pi \int_0^\infty x dx [1 - \exp(-D_\delta/D_{37})] \quad (3.2.3)$$

To evaluate this formula, one must rewrite $D(\delta)$ in function of the energy(ω) using the mathematical delta function.

$$dn = \frac{CZ^*}{\beta^2} \frac{d\omega}{\omega^2}, \omega \leq \omega_{max} \quad (3.2.4)$$

Or,

$$dn = 0, \text{ if } (\omega > \omega_{max}) \quad (3.2.5)$$

where :

$$Z^* e = Ze[1 - \exp(-125\beta Z^{-2/3})] \quad (3.2.6)$$

and

$$C = \frac{2\pi N e^4}{m c^2} = 0.85 \frac{keV}{100\mu} \quad (3.2.7)$$

This represents the number of delta electrons in a length unit at an angle of 90 degrees. The integration of electrons number give the formula :

$$n[\omega(x), \omega_{max}] = \frac{CZ^{*2}}{\beta^2} \int_{\omega(x)}^{\omega_{max}} \frac{d\omega}{\omega^2} = \frac{CZ^{*2}}{\beta^2} \left[\frac{1}{\omega(x)} - \frac{1}{\omega_{max}} \right] \quad (3.2.8)$$

In light of the experimental findings, Weber 1964 fitted the following expression [120]:

$$D_\delta(x, \beta, Z^*) = \frac{k^{-1} dx CZ^{*2}}{2\pi x dx \beta^2} \left[\frac{1}{\omega(x)} - \frac{1}{\omega_{max}} \right] \quad (3.2.9)$$

Hence, it could be rewritten as :

$$D_\delta = \frac{CZ^{*2}}{2\pi x \beta^2} \left[\frac{1}{x} - \frac{1}{X} \right] \quad (3.2.10)$$

$k\omega(x) = x$ and $k\omega_{max} = X$. The formula '3.2.10' allows one to calculate the amount of energy deposited per unit mass in various mediums. Depending on how far x is from the trajectory, for various particles of different energies. The model is then effectively updated from Fain [121], which incorporates the deposited primary energy and all possible values of the electron emission angle. There is often a variation of up to a factor of ten between the dose estimates produced for the same particle in the same detector using these two models [122]. In 1986, Waligorski [123] continued and later improved the calculations of Katz and Kobetich, which were based on Monte Carlo calculations of the dose distribution in liquid water and integrating the interactions of the primary particles and all of the secondary particles that accompany the passage of the incident ion. Two possibilities have been put forth on the path-energy relationship of the electrons, depending on how the incident particle's energy relates to the medium electron's binding energy. In one of them, the electron range-energy relation had been considered to be linear and the medium's electrons are thought to be initially bound at ionization potential I , which they setted arbitrarily at $10eV$. In the other, the electrons are free and the range-energy relation could be provided using a power law. for the bounded electrons, the range-energy relation for electrons as

$$r = kw \quad (3.2.11)$$

Whereas, the free electrons having a range-energy relation looking like :

$$r = kw^\alpha \quad (3.2.12)$$

The range-energy relationships had been based on a fit of an available experimental data (see references in [124]).

The Rutherford formula for delta-ray production from a medium containing N electrons per unit volume, bound with ionization potential I which is supposed to be ejected along the normal and go straight. The number dn of secondary electrons with energies between ω and $\omega + d\omega$ produced by an ion with an effective charge of Z^* travelling at a speed of $v = \beta c$ is given by the equation [3.2.13]:

$$dn = \frac{2Ne^4Z^{*2}}{m_e c^2 \beta^2} \left(\frac{d\omega}{(\omega + I)^2} \right) \quad (3.2.13)$$

For the bounded electrons with the potential I the dose deposited in a cylindrical layer of radius r and thickness, dr around the trajectory of the charged particle is given by:

$$D_0(r) = \frac{1}{2\pi r dr} \int_{\omega_r}^{\omega_{max}} \left(-\frac{d\omega_r}{dr} \right) dr \frac{dn}{d\omega} d\omega \quad (3.2.14)$$

where : $\omega_{max} = 2m_e c^2 \beta^2 / (1 - \beta^2)$ is the maximal energy of an electron delta. The integration of Equ [3.2.13] give the following formula of dose :

$$D_0(r) = \frac{Ne^4Z^{*2}}{m_e c^2 \beta^2} \left(\frac{1}{r + \theta} - \frac{1}{R + \theta} \right) \quad (3.2.15)$$

with $\theta = kI$ and $R = k\omega_{max}$. For the free electrons where, $r = k\omega^\alpha$, the dose formula will be then,

$$D_1(r) = \frac{Ne^4Z^{*2}}{\alpha m_e c^2 \beta^2 r} \left[\frac{\left(1 - \frac{r+\theta}{R+\theta}\right)^{1/\alpha}}{r + \theta} \right] \quad (3.2.16)$$

The parameters for the water, they are :

$$k = 6 \times 10^{-6} gcm^2 . keV^{-\alpha}$$

$$\alpha = 1.079 \text{ if } \omega < 1keV$$

$$\alpha = 1.667 \text{ if } \omega > 1keV$$

These formulas are correct to within 10% only for electron energies under $2keV$. Waligorski had updated the formula by adding an extra factor as follows :

$$D_2(r) = D_1(r)(1 + k(r)) \quad (3.2.17)$$

where:

$$k(r) = A \left(\frac{r - B}{C} \right) \exp\left(-\frac{r - B}{C}\right) \quad (3.2.18)$$

A, B and C are determined semi-empirically. The equation “3.2.16” is the dose deposited by the secondary electrons. The quantity, $D_2(r) = D_1(r)k(r)$ characterizes the contribution to the radial dose of the excitations and primary ionization and equation(3.2.17) gives the total radial dose deposited in a cylinder of radius , r around the path of the charged particle. As an alternative, a model of ion track structure based on traditional collision dynamics was created by Kiefer and Straaten in 1986[125]. They used the empirical range-energy equations of “3.2.11”and “3.2.12” and created a straightforward formula that predicts nicely the radial dose distribution. It is significant to note that over the past few decades, these models, along with others like those given by Cucinotta et al [126, 127] and Chen et al (1997)[128], have undergone countless adjustments and enhancements and continue to be improved [129]. An essential and initial step in simulating the radial dose is the electron range-energy relationship. Given the inherent challenges in establishing accurate theoretical assessments for this relationship, empirical formulas based on experimental data had almost been designed to approach this relationship, as was the case in the example of “3.2.12”3.2.11”. On the other hand, such measurements were made by Tabata et al. (1972)[130], who also suggested empirical range-energy relationship for electrons which is written like :

$$R(T) = a_1 \left(\frac{1}{a_2} \ln \left(1 + a_2 \frac{T}{mc^2} \right) - \frac{a_3 \frac{T}{mc^2}}{1 + a_4 \left(\frac{T}{mc^2} \right)^{a_5}} \right) \quad (3.2.19)$$

$\rho = 1g/cm^3$ for water, $a_1 = \frac{b_1 A_T}{\rho Z_T^{b_2}}$, $a_2 = b_3 Z_T$, $a_3 = b_4 - b_5 Z_T$, $a_4 = b_6 - b_7 Z_T$ and $a_5 = \frac{b_8}{Z_T^{b_9}}$. Z_T and A_T are the atomic number and the mass number of the target, the b_i are empirical constants existed in the reference[129]. Awad et al[129] developed a model using the formula “3.2.19”. This technique is similar to that proposed by Kiefer and Straaten (1986)[125] and Spohr (1990)[131]. Their model provides a useful alternative for time-consuming Monte Carlo simulations and works well for hadron treatment dosimetry.

Z. Lounis-Mokrani et al [132] used the small angle neutron scattering (SANS) technique to experimentally confirm this method, determining the radial size of the damaged region caused by the proton beams in the CR-39. By employing Guinier-plots, the track core’s radii have been determined. Following that, the outcomes are contrasted with those that were determined

using Waligorski radial dose distribution.

3.3 Nuclear tracks characterizing techniques

Nuclear tracks can be classified into three distinct types : latent tracks, birth tracks and revealed tracks. Latent tracks, with diameters on the order of angstroms are directly produced by irradiation on untreated CR39. After a short period of etching, birth tracks become visible, appearing as tracks with diameters of only a few micrometers. With extensive etching, revealed tracks develop and become more apparent [133][134]. The dimensions and characteristics of the tracks dictate the most suitable monitoring technique to be used. The characterisation is done by highlighting the generated perturbations caused by the passage of the charged particles. There exist a diverse range of techniques where each one is limited to characterizing specific structural properties regarding to the resolution of that technique. These techniques can be classified based on the type of information they yield. The most used in characterization of the latent tracks , we address :

*Small Angle Neutron Scattering(SANS) and Small Angle X-ray Scattering (SAXS) techniques which provide the radial damage distribution [135][132][136]. We can measure with SANS, $10^{11} - 10^{13} tr/cm^2$.

*Ultraviolet-Visible(UV) technique provide the study of the chemical structure where the chains cross linking could be quantified [132][137][138].

*Infra-red(IR) and Electron Spin Resonance (ESR) could quantify the radicals formation and scission of bonds [132][139][140][138].

Concerning the analyzing of birth and revealed tracks, almost always, we use : Optical microscopy(OM), scanning electron microscopy (SEM) and transmission electron microscopy (TEM) techniques which visualizing the tracks. It could measure the tracks density ($10^5 tr/cm^2$), diameters and the track profile. With MEB, we can visualize until, $10^5 tr/cm^2$ and measure the tracks diameters [141][142][143]. These extensive assessments give us an overview of the numerous effects caused by charged particle radiation on materials.

3.3.1 Latent tracks characterisation

As was already indicated, the latent tracks are the direct result of the charged particles irradiations. These tracks are confirmed to result from chemical bonds being disrupted, which also

causes free volumes to form within the material. Latent tracks may also include chain endings as a result of the broken molecular bonds in the CR39 material. These modification could be analyzed using (UV and IR).

Because the CR39 is an insulating polymer known for its wide bandgap, The UV spectroscopy could be benefited in monitoring their variations. However, the presence of weakly bonded π electrons or n electrons, associated with chromophoric groups like $C = C$ (180 – 220nm) or $C = O$ (160nm) bonds, leads to $\pi \rightarrow \pi^*$ and $n \rightarrow n^*$ transitions. As tracks form, the bonding of double bonds between them shifts these bands towards the visible spectrum for $\{C = C(233 – 235)$ and $C = O (257 – 275nm)\}$ in case of proton irradiated CR39 [122]. The increased formation of these conjugated systems reduces the optical gap energy.

In the literature, we find Mostafa Fawzy Eissa et al, 2011, [144] studied the optical properties of CR-39 irradiated with alpha and gamma. Where they noted an absorption peak appeared at 208nm in the UV spectra for the $E_\alpha = 4.86MeV$. Moreover, A. Saad et al, 2014 [145] declare that the UV–visible spectra of alpha irradiated CR39 ($E = 4.86MeV$) demonstrated that there is a chain scission at low fluence. The chain scission increased at high fluence and a decrease in band gap energy is noted. On the other hand, Zaki et al, 2017 [146] studied the UV/Vis responses of alpha CR39 irradiated with different fluences (1.62×10^6 , 2.72×10^6 , 3.82×10^6 and 5.21×10^6 particles/cm²) and find out that it exhibits a single absorption band in the range of 254–352nm.

Infrared (IR) analysis relies on the absorption of vibrations/rotations in bonds of $C = C$ at $1650cm^{-1}$, $C = O$ at $1734cm^{-1}$, $C - O - C$ at $1133 - 1090 - 1022cm^{-1}$, $C - O : 1227cm^{-1}$, and $C - H$). Changes in the concentration of these vibrational energy levels can quantify the radicals formed and reflect the distribution of deposited energy. Almost always, the IR analysis of alpha irradiated CR39 was rarely highlights a significant modification [146]

Concerning the free volumes study, The PAS technique was classified as a unique method for characterizing and investigating them. In the following, a detailed review about the study of free volumes will be presented.

Free volumes :

The free volumes in polymers describes the portion of the total mass that is not actually occupied by the molecules as like demonstrated in Fig. 3.3.1. It is generated on redistribution upon molecular chain packing. This effect could be the result of radiation damage [147] [148].

The following types of free volume are further characterized based on how polymer chains are packed [149]. Hole free volume is the term for the free space that exists between a specific polymer's perfectly aligned polymeric chains.

Configurational free volume: An additional free space known as configurational free volume is created as a result of insufficient chain packing.

Fluctuation (dynamic) free volume: As polymeric side chains move, they leave small gaps that result in the creation of fluctuation free volume.

The concept of free volume can be beneficial when examining the chain segments mobilities in concentrated polymer solutions. It gives solid molecules the flexibility to move.

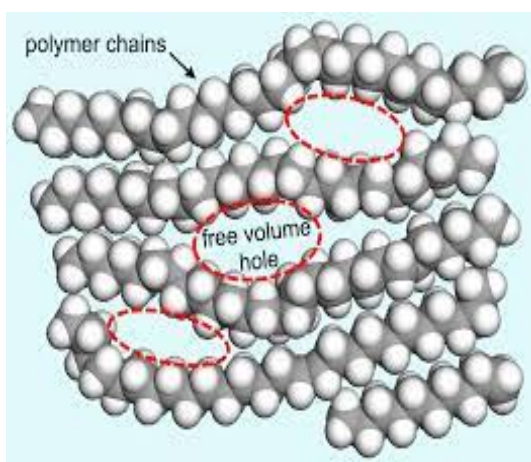


Figure 3.3.1: Free volume holes [8]

The thermal, mechanical, and relaxation properties of polymers are influenced by the relative percentage of these holes. In the literature, there are a lot of different free volume theories. Fujita presented the earlier idea, and Vrentas and Duda presented another useful theory [150]. In both theories, the chance of the jumping to the the free volumes has been assessed. The jumping unit is chain segment for the polymer component. However, they use a distinct formulation in each hypothesis. According to the Fujita theory, the Doolittle equation relates the free volume per unit volume to the jumping unit's mobility [151]. By applying the Cohen-Turnbull equation [152], Vrentas and Duda hypothesize that the mobility of jumping units is determined by the average free volume per jumping unit [153]. On the other hand, the free-volume Simha-Somcynsky theory was created in 1969 and is based on the lattice cell model. According to this theory, the free volume is determined by equating it to the percentage of vacant cells, which is established by minimizing the Helmholtz free energy [154].

Characterizing Free volumes using PAS

Given the significance of free volume, only a small amount of experimental information regarding the free volume of polymers has been published. This is mostly because there aren't any good probes for subnanometer molecular dimensions and because many dynamic motions have a short time scale. Most of physical methods that were used were for static defects. Only other indirect measurements, like precise volume experiments or calculations based on theoretical models, like the van der Waals dimensions for molecules, might be used to determine it. This is because probing the free volume, which has a small size and persists for a brief period of time is fundamentally challenging. The free volume of polymers has really been measured in a number of efforts. Free-volume size distributions have been derived from density fluctuations using small-angle X-ray and neutron diffractions. Atomic force microscopy (AFM) and scanning tunneling microscopy (STM) are both sensitive to Å size, however they can only be used in static holes and on the surface. At a size of 10Å or above, scanning electron microscopy (SEM) and transmitting electron microscopy (TEM) are more sensitive to static holes. In the Fig. (3.3.2) a resumed concerning the scale where the the above methods are available are shown.

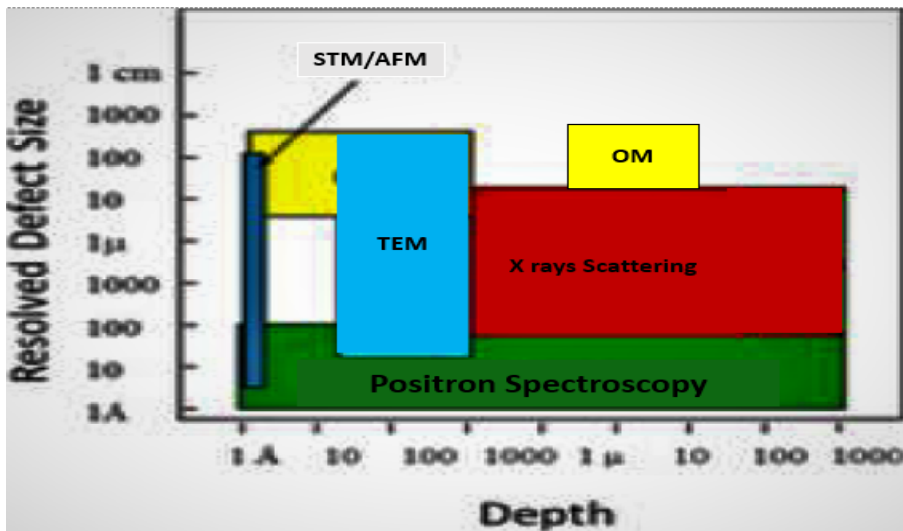


Figure 3.3.2: Methods for Characterization and Their Resolutions[9]

Once PAS technique has been recognized as a nuclear probe technique[155]. It has been possible to investigate or study the existence of free volumes, which can include timescales from (10^{-13}s) to (10^{-16}s) and diameters therein $(1 - 10)\text{Å}$. PAS is proposed as an exclusive method for investigating the free volumes grow which is uniquely suited for probing free volumes

as shown in Fig. (3.3.3). Hence, the monitoring of the latent tracks which is resulted on the radiation passage upon polymer could be achieved by pursuing the evolution of free volumes [156] [157] [158]. Any of the current techniques, such as positron annihilation lifetime spectroscopy (PALS), Doppler broadening spectroscopy (DBS) or Variational Energy Positron Annihilation Spectroscopy (VEPAS), can be used to calculate the overall change in the free volumes.

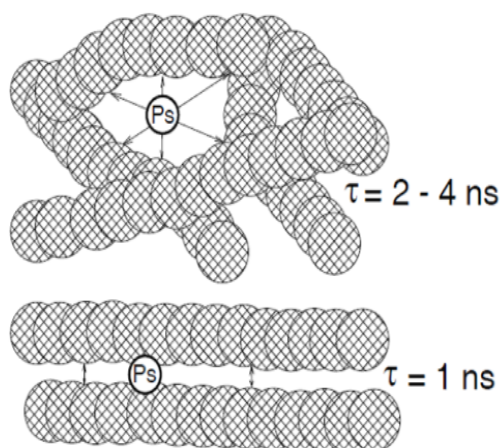


Figure 3.3.3: Ortho-Ps annihilation in the crystalline and amorphous phases of polymers. Local freevolume sizes typically range from 0.5 nm. [10]

In contemporary applications, PALS has been utilized to determine the dimensions of free volumes. This technique involves measuring the lifetime of orthopositronium, τ_3 . The specific value of τ_3 is influenced by the electron density surrounding the orthopositronium particle. This particle tends to reside within areas of lower electron density, causing τ_3 to rise as electron density decreases. Within the context of theories concerning free volume, the orthopositronium particle is confined within a free volume region. In this scenario, the lifetime τ_3 experiences an augmentation as the size of the free volumes increases. In addition to measuring the orthopositronium (o-Ps) lifetime (τ_3), we also determine the total fraction of positrons that form o-Ps, denoted as I_3 . The formation of o-Ps particles is presumed to be contingent upon the prevalence of regions characterized by low electron density, leading to an elevation in its value with an increasing concentration of free volumes. This suggests that PAS has the potential to provide direct insights into both the size and concentration of free volumes within the polymer matrix. However, it's important to note that empirical observations indicate a substantial impact on the intensity from various factors. These factors encompass the source strength and radiation duration, the presence of an electrical field as well as exposure to visible light [159].

The fraction of free volume (F_v) is defined mathematically as the ratio between the available free volumes and the entire volume. Initially, determining the complete fraction of total free volume required the application of semi-empirical methods. For instance, a technique involving the measurement of external volume concerning hydrostatic pressure and temperature, $V(P, T)$, was employed. This approach utilized the statistical mechanical equation-of-state (EOS) theory developed by Simha and Somcynsky [160]. Then, a general formula has been conducted. The free volumes don't have constant sizes inside any one sample state. It is important to note that the existence of a unique lifetime parameter, τ_3 , does not imply that positrons exclusively annihilate in with the same size. On the contrary, there is unquestionably a distribution of free volumes of various sizes. It makes sense to assume that an orthopositronium (o-Ps) atom can spend its entire lifetime exploring different free volumes. Despite the variation in free volume sizes in this situation, all o-Ps atoms share an average lifetime (as measured). The total of the contributions coming from various free volumes makes up the measured probability of annihilation, λ . Each contribution is weighted by the λ value associated with that free volume [161].

The free volumes are found to be dramatically affected by temperature. Dlubek and coworkers studied how temperature influence on the evolution of free volumes [147 21]. The free volumes spread when the temperature rises due to the thermal mobility of the adjacent atoms. Then, the thermal expansion of free volumes contributes to the expansion of diameters. The anharmonicity of molecular vibrations and local motion close to the holes are also a principal forces behind this expansion [162, 163]. As the temperature rises, the intensity (I_3) becomes less intense, which suggests that the density of holes is decreasing. This prompts us to propose the hypothesis that, rather than an increase in the number of holes, the increase in total free volume at higher temperatures is predominantly defined by the enlargement of hole size.

In the literature, several researchers have conducted studies on the growth of free volumes brought on by irradiation in CR39 and other polymers. Notable examples include Dlubek et al. [164, 147, 21], Lounis-Mokrani et al. [165], and Kumar et al. [166, 167, 168, 169]. Their research has been used the correlation of o-Ps lifetime with free volume dimensions. The delicate mechanism of how irradiation affect the free volumes inside the polymer matrix has been clarified. In particular, their work has delved into the phenomena of cross-linking and bond scission within CR39 polymer chains. These processes might produce new chemical entities

in the latent tracks which highlight the complexity of the structural changes brought on by charged particle radiation. Furthermore, the S-parameter in an un-irradiated sample serves as a reference value. Beyond this value, every rise in this parameter denotes the existence and extension of free volumes within the material. These works have significantly contributed to the scientific community's understanding of the structural changes occurring at the atomic and molecular levels due to radiation exposure. A thorough picture of the progression of damage creation after the initial exposure to irradiation is shown in Fig. (3.3.4). This illustration shows the progression of the irradiation from its initial stages to the final formation of free volumes inside a polymer matrix.

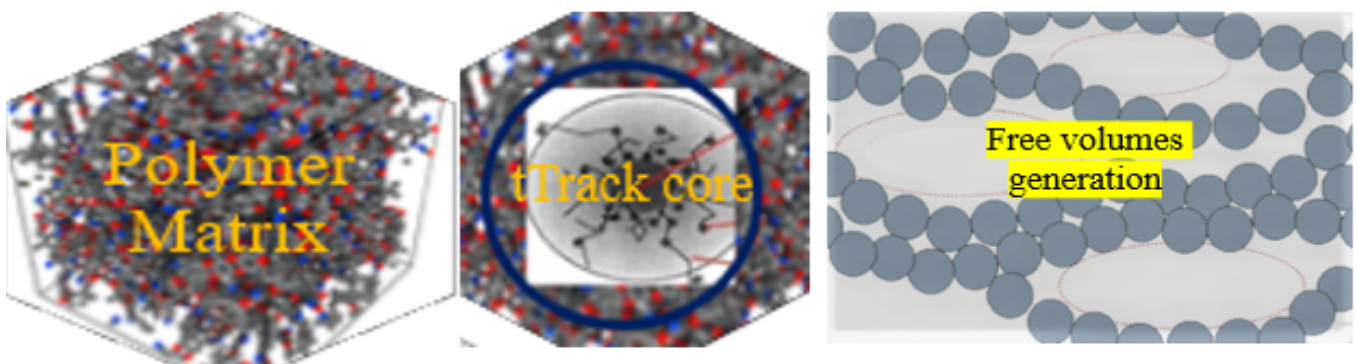


Figure 3.3.4: Free volumes growth under irradiations

3.3.2 Etching process

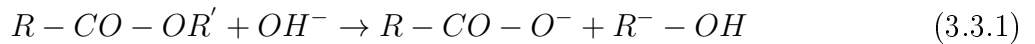
The monitoring of the nuclear tracks could be realized also via the monitoring of the etched tracks which could be birth or revealed tracks. The last need exhibits the use of the chemical etching where the tracks are studied by analyzing the variation of the different track-etch parameters (length, diameter, track density, track etch rate...) obtained from the optical microscopy (OM), MEB or AFM.

In the etching operation, almost always, the samples is immersed in a thermal bath containing a basic solution to carry out chemical etching. The etchant was continuously agitated during the etching procedure to guarantee their uniformity and homogeneity[170]. The detectors were properly cleaned in distilled water after the etching process to get rid of any left etchant. They were then dried to end the etching process permanently and get clear of any *KOH* or other components of the basic solution that might still be on the detectors. In an attempt to determine the ideal etching conditions, such as the concentration, temperature, and etching time, the etching of irradiated CR39 has been thoroughly researched and is still being

explored. Alkaline etchants like sodium hydroxide ($NaOH$) and potassium hydroxide (KOH) are frequently employed in the literature to etch $CR39$.

The KOH hydroxide solution is more suitable as chemical etching than $NaOH$ for $CR39$ polymer because the KOH is slightly more basic than $NaOH$ due to the larger size and lower charge density of the potassium ion (K^+). The larger ion size allows for better dispersal of the negative charge, resulting in a higher degree of hydroxide ion availability. For these alkaline solutions, the recommended etching temperature is between 60 and 70°C, and the normal concentration is between 6 and 7N [171].

When Gruhn et al [112] first explored the mechanism of etching, they discovered that the carbonate ester bands, which are clearly visible in figure 3.1.2 undergo hydrolysis when they are attacked by a powerful base like KOH . As a result, the hydroxide ion breaks down the carbonate ester linkage in the PADC molecule, releasing the carbonate ion and other organic etch products like : diethylene glycol, and ethylene glycol which the majority of, are polyallyl alcohols as illustrated by the following equation [171]



The reaction 3.3.1 depicts as an endothermic reaction, which means it needs energy to start. It is known that the temperature of the etching solution increases the rate of this process. The fact that the etching rate exponentially depends on both the temperature (T) and the concentration (C) of the etchant solution is actually one of the most notable aspects noticed in the etching process. The etching rate accelerates exponentially as the temperature and concentration rise. This behavior demonstrates the sensitivity of the etching process to temperature and concentration variations, which can greatly affect how quickly material is removed [172] [173]

3.3.3 Etched tracks characterisation

When the latent tracks are etched, they become larger and, when seen under an optical microscope, manifest as dark circles. Usually, the progression of track growth has been described geometrically. The track shape that is most frequently seen is a cone whose axis is the trajectory of the incident particle [174]. The final configuration of the track is influenced by the bulk etch rate (V_b), which displays the etch rate in the majority of SSNTD (no damaged regions), the preferential attack rate (V_i), or track etch rate, which is related to the etch rate of the damaged

zone along and around the ion's trajectory, and the angle of incidence of the particle (whether it is normal or oblique) [175]. In case of normal incidence, the particle arrives at a detector perpendicularly to the detector's surface (Figure 3.3.5). Here, "I" is the initial surface, "I'" is the surface after etching, "V_t" represents the track etch rate, and "V_b" symbolizes the bulk etch rate of undamaged sections. Where "OE" equals the particle's range within the detector material, "O" and "E" stand for the particle's entrance and endpoints, respectively. "L'" and "L" stand for the distances that the etching solution travels and the track depth, respectively. The distance "h" represents the layer thickness that has been removed by etching [11]. The track depth is given by :

$$L = (V_t - V_b)t \quad (3.3.2)$$

where, t is the etching time.

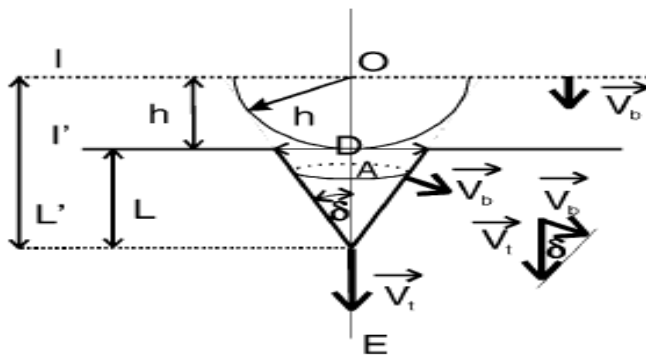


Figure 3.3.5: The track's development's geometry (V_t is constant) [11]

The ratio $V = V_t/V_b$, determines how well a track will evolve. $V > 1$ is a need for track creation, which means that V must be greater than or equal to 1. In Figure 3.3.5 the local development angle " δ " is significant. It is clear from the resemblance of the triangles in the illustration that $\sin(\delta) = 1/V$. The specific track etch rate (V_t) and the bulk material's etching rate (V_b), are key differences that affect the sensitivity of polyallyldiglycol carbonate (PADC) to the etching process. This sensitivity, denoted by the letter "S," is defined as

$$S = (V - 1). \quad (3.3.3)$$

From the track figure, we can see that :

$$\tan(\delta) = \frac{D/2}{L} = \frac{h}{\sqrt{L'^2 - h^2}} \quad (3.3.4)$$

Where D is the diameter of the track opening. It could also be written as :

$$D = 2h\sqrt{\frac{V-1}{V+1}} \quad (3.3.5)$$

If $V \gg 1$, $D \cong 1$. The track has a cone-like shape in three dimensions and is defined by a growing angle " δ ." By turning the track wall around the trajectory of the particle, this angle is produced. The path that a point on the track wall follows as it circles the particle's path. This path is represented by the circle " A " in the figure [3.3.5](#). The track wall moves parallel to its own orientation while it is being etched.

Comprehensive research has been done on the topic of nuclear track etching in polyallyldiglycol carbonate (PADC), including both theoretical and experimental work. The main goal of these initiatives has been to create standardized methods for classifying tracks. The basis for this characterisation procedure is a number of crucial variables, including V_b (bulk etch rate), L (track length), D (track diameter), V_t (track etch rate), and the angle of incidence of particles [\[176\]](#), [\[177\]](#), [\[178\]](#), [\[173\]](#), [\[179\]](#). Thorough analysis have been done to reveal the complexities of these recordings. The track-etch parameters, including track length, diameter, density, and rate, have undergone careful examination. These investigations are carried out using optical microscopy (OM) and the atomic force microscopy (AFM). The outcomes are then associated with crucial elements including the time of the etching procedure and the innate characteristics of the incident particles. Prior research projects have demonstrated this thorough analysis [\[180\]](#). These thorough analyses led to the development of numerous models that describe the track etching procedure where the availability of track length and track profile data has served well in developing empirical models. As an illustration, Yamauchi et al. created a model of the overlapping probability of latent and overlapped tracks. Furthermore, Zylstra et al. presented a novel model that was created expressly to account for track overlap in in CR-39. It's important to remember that the latter model can only manage the overlap of two tracks [\[181\]](#). The ability of these models to accurately reproduce the complex sizes and patterns of etched tracks found in experimental tests has been astounding.

Conclusion

Nuclear track methodology provides an alternative method for the analysis of alpha particle energy, especially in situations in which the measurements need to be in situ and/or in the open air. They showed the possibility for identification and measurement of alpha contaminants [\[182\]](#)

[183] and radon dosimetry [184][185] as an example. This greater comprehension helps to improve radiation dosimetry techniques and develop applications in nuclear engineering. We can improve protective measures, engineer radiation-resistant materials, and create safer nuclear technologies thanks to our ability to quantify latent tracks, display birth tracks, and reveal revealed tracks. The positron annihilation technique has been used extensively to characterise the structural properties of polymers. A thorough study of the uniqueness of PAS in studying the free volumes has been presented in the chapter.

Chapter 4

Results and Discussion

Introduction

In the last chapter, we conclude with a thorough examination of the key experiments carried out in the process of developing and optimizing PAS settings . A thorough summary of the steps is given for each of the four configurations: PALS with BC418, PALS with EJ228, DBS, and VEDBS. The development and fine-tuning process of each setup is carefully analyzed, providing insights into the difficulties and advances encountered. Then the attention turns to characterizing various series of CR39 samples that have been exposed to alpha radiation. The irradiation processes used to three different sample series are thoroughly described in this chapter. Next, as a useful application of the PAS setup, the characterisation of these samples is methodically carried out. This step highlights the success and applicability of the methods used throughout the study, in addition to validating the effectiveness of the established PAS setups.

This thesis is primarily concerned with finding the best circumstances to reach the best resolution possible for polymer characterisation. Verifying the optimal time resolution is a crucial step towards achieving this goal within the scope of the Positron Annihilation Lifetime Spectroscopy (PALS) method. During the course of the experiments, great care was taken to evaluate the spectrometer's performance using the time resolution and counts rate metrics. The most notable accomplishment in this context was the 50 counts per second (cps) count rate and the incredible temporal resolution of 0.270 picoseconds. Within the DBS setup, a significant result was shown by means of tests that allowed the 511 KeV peak in silicon to be calibrated until the S parameter was equal to 0.5. This result highlights how accurate and calibrable the DBS system is, making it more useful for spectroscopic investigation. Moreover, a detailed

demonstration and explanation of the setup and configuration of the Variational Energy Doppler Broadening Spectroscopy (VEDBS) apparatus were provided. This guarantees a thorough comprehension of the configuration, enabling its efficient application in later investigations. Through the presentation of these successes and methodological specifics, the thesis emphasizes a commitment to improving the capabilities of every spectroscopic setup, which ultimately contributes to the overall objective of improving polymer characterization by means of optimum experimental conditions.

The second goal of our thesis is the characterization of free volumes using PAS. The free volumes is classified as a latents tracks, the latents tracks characterization would be assumed by monitor the free volumes growth. By assess chemical and molecular changes(free volumes changes), we could quantify nuclear tracks which permits the characterization of CR39. Adding to that, the combination of chemical etching with positron-based measurements might be valuable in getting insights into the structural changes induced by alpha induced tracks in the CR39.

The Waligorski model of radial dose distribution has been used to validate the experimental findings. The validation process involves a comparative analysis between the experimentally derived F_V from PALS and a computed F'_V using the Waligorski Calculation method. Surprisingly, a significant accord has been reached, confirming the validity of the experimental results.

A brave attempt has been made to use Density Functional Theory (DFT) theory to compute the lifetime of $o - Ps$ in un-irradiated CR39 through the development of a Python code. In Section"4.12", the scheme and approach used to run this code will be discussed in detail. This adds a computational analytical layer to the thesis and helps the reader comprehend the theoretical elements of positron behavior in the CR39 better.

4.1 PALS Experiments

We have two different composed detectors in the lab. In order to find the appropriate one, we had to look at each one. This section presented the equipment required to construct the positron annihilation lifetime spectrometer (PALS) which is used throughout this research. The PALS system is ultimately based on fast plastic scintillators coupled to photomultiplier tubes. We have set up two PALSs. The first configuration's comprised detector is the *BC418*

plus the *Burle8850* plus the *265A*. The second configuration is $EJ228 + H3378 - 51 + 265A$. This section concerns necessary steps to perform prior to using PALS for experimental work. Optimisation of components will be discussed and justified. An example for the measurement of positron lifetime spectrum is presented. The optimization of the PALS-chaine is done by following the set of instructions below :

- 1: Heigh voltage optimisation
- 2 : Energy selection
- 3 : Calibration

4.1.1 Heigh Voltage optimization:

The detector needs to be polarized with a voltage that ensures their functionality. Realizing that a negative voltage is necessary for this kind of detectors. As a result, we will run the subsequent experiment twice, once for the START detector and again for the STOP detector. The voltage generator is shown in Fig"4.1.1".



Figure 4.1.1: Bias Voltage Generator

and here is the setup :

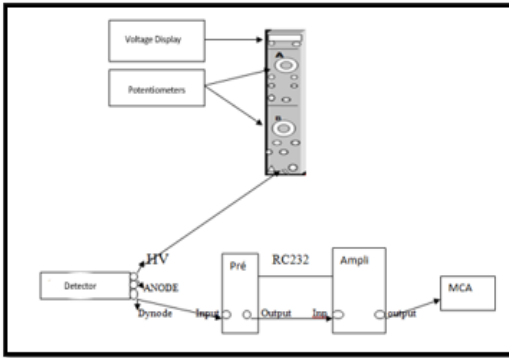


Figure 4.1.2: Bias voltage optimization circuit

We connect the high voltage output of the detector with the generator (A for STOP-Detector and B for START-Detector) and the dynode output (energy output) with the input of the preamplifier, then the current passes from the output of the latter to the input of the amplifier where the final link will be to the MCA. Before recording the spectra, the acquisition card is calibrated using the Cobalt source ($1.17MeV$). The choice of the optimal voltage is done according to the following criteria :

- Better counting
- The sharpest peak
- The range between the two peaks

4.1.2 Energy Selection :

The measurement of positron lifetime consists in the detection of gamma photon $1.28MeV$ by the START detector which indicates their birth and the detection of annihilatin photon $0.511MeV$ by the STOP detector. However, the detectors detect the two gamma rays. For this reason, one must select certain interval of the tensions using discriminator CFDD START in order to let pass only the signals which can produce the energy peak $1.28MeV$. The same for the STOP detector, using CFDD STOP we determine the signals that can reproduce the energy peak of $0.511MeV$. The selection of energy can be carried out by two methods : (Oscilloscopr or SCA-Counter)

Energy selection using the oscilloscope

START Detector: Using the oscilloscope, here is the assembly we made using the oscilloscope.

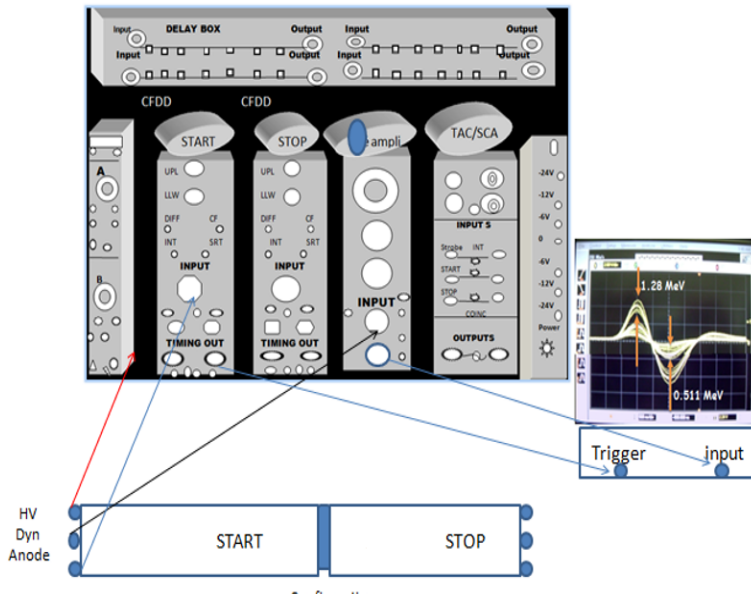


Figure 4.1.3: The energy selection assembly using the oscilloscope (START detector)

The cables are linked as follows : The first link made from the dynode output with the amplifier (you can insert a preamplifier because the energy signal is weak), the anode output will attach with the CFDD. Then we close the circuit by linking the output of the amplifier with the input of the oscilloscope and the TIMING output of CFDD with the Trigger input of the oscilloscope (Trigger is a specific input for temporal signals). According to the assembly shown in Fig^{4.1.3}, one can visualize the two energy packets detected by the START detector. It is clear that there is a voltage bundle that sweeps the 1.28 MeV energy, our job is to specify the minimum and maximum voltage. The discrimination is made using an SCA integrated in the CFDD. From the oscilloscope the highest value of the 1.28MeV packet voltage corresponding to the 4.07V and we know from the literature that this packet begins to appear from 0.7MeV, let's make the rule of three we conclude that the minimum voltage for 1.28MeV bunch can appear is 2.22V.

After this estimate, we fix the cursure of oscillo on the voltage 4.07V and we vary the voltage of ULD (in CFDD) until a signal coincides this value. Second, we fix the cursure(oscillo) on the 2.2V voltage and vary the LLD voltage (in CFDD) to appear a coinciding signal. At the end we read the tensions in the CFDD and close the windows of each potentiometer. The voltage values are : $LLD = 2.25V$, $ULD = 4.21V$.

STOP Detector : For the STOP detector, the selection was made for the 511KeV bunch. The corresponding voltage range :

$$(0.511\text{MeV} \rightarrow 0.81\text{V})$$

$$0.34\text{MeV} \rightarrow 0.53\text{V}$$

On the other hand, there is a chance of mingling with the lower front of the 1.28MeV energy. Hence, the discrimination for the maximum apparent tension of the package 0.511MeV will be made between the minimum apparent tension of the package 1.28MeV and the maximum apparent tension of the package 0.511MeV . The visualization [4.1.4](#) displays the following tensions for the 1.28MeV package.

$$1.28\text{MeV} \rightarrow 2.22\text{V}$$

$$0.6\text{MeV} \rightarrow 1.03\text{V}$$

Hence, for maximum voltage value, discrimination will occur between 0.81V and 1.03V . By setting the voltage cursor at the oscilloscope level as we did previously, we may control the voltage by varying the behavior of the connectors $CFDD(LLD, ULD)$ until a signal emerges. Finally, the voltage values were read as $LLD = 0.35\text{V}$ and $ULD = 1.27\text{V}$.

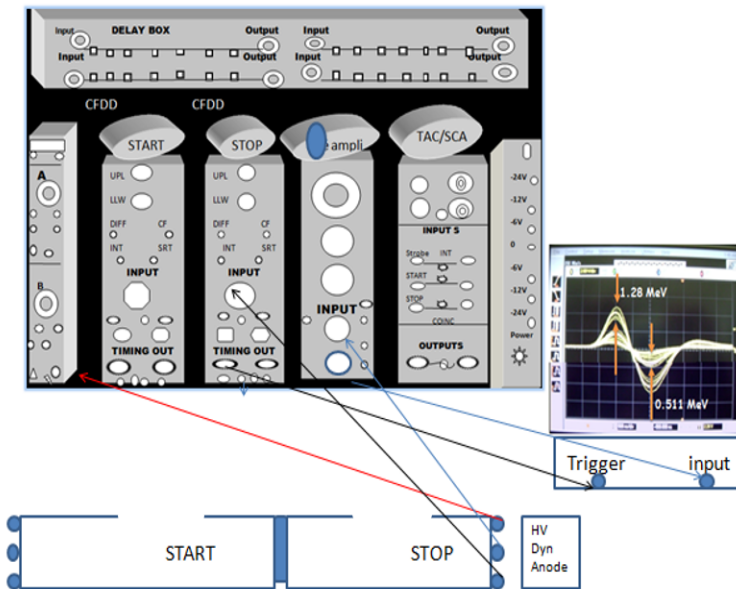


Figure 4.1.4: The energy selection assembly using the oscilloscope (STOP detector)

Energy selection using SCA-Counter

The energy selection method could be carried out by using a Counter-SCA (demonstrated in figure 4.1.5)

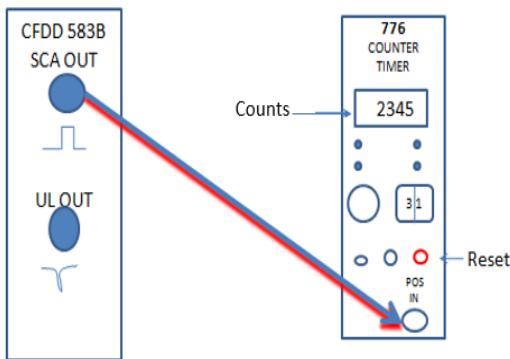


Figure 4.1.5: SCA-COUNTER circuit

In this technique, we tried to make the selection as follows: First, we vary the *CFDD* voltage from $0.1V$ up to $5V$, take 0.1 as the step and read the number of counts displayed on the counter. Second, we plot the number of counts recorded as a function of voltage.

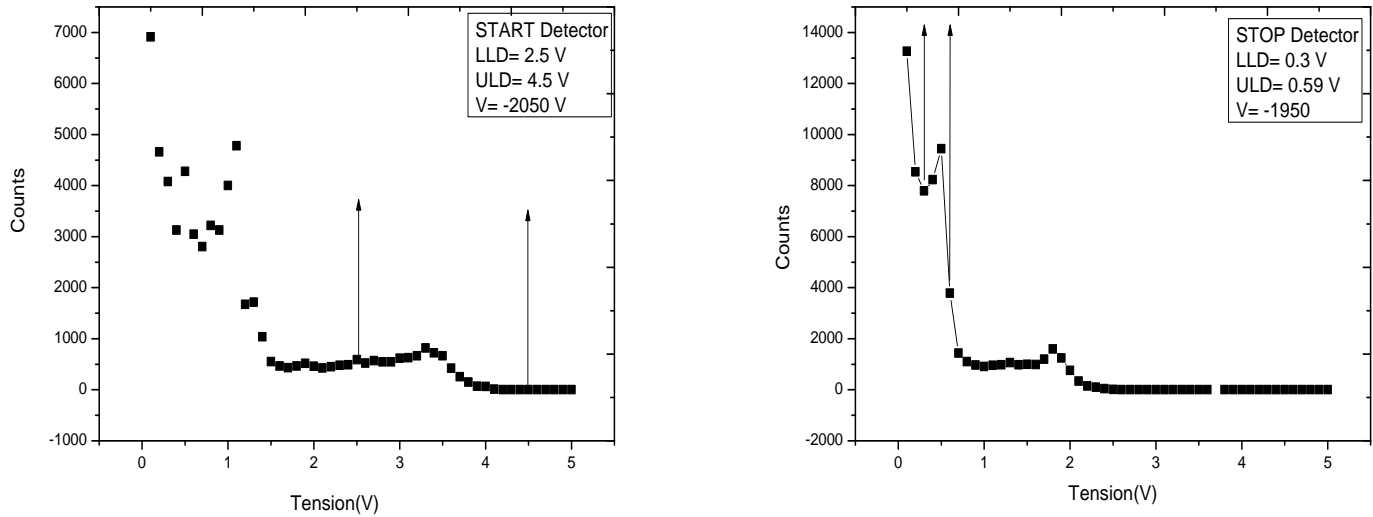


Figure 4.1.6: Energetic spectrum of START and STOP detectors

From the selection, we set the potentiometers to the values indicated in figure 4.1.6

4.1.3 Setting-up the spectrometer :

After assuming the energy selection, the recommended mounting is carried out as shown in 4.1.7, allowing for the measurement of the nanoseconds (positron lifetime) that elapse between the detection of the two start and stop signals.

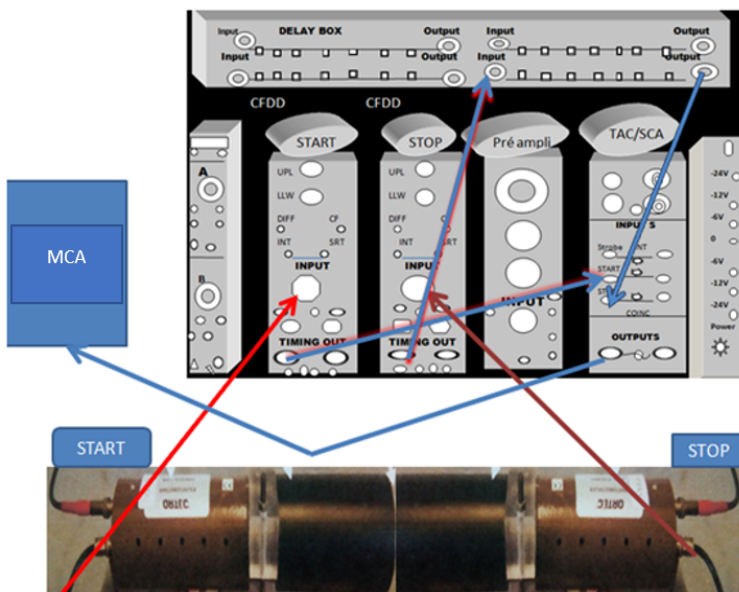


Figure 4.1.7: PALS set-up

We can say that the current flows through two paths in this assembly, one from the start

detector and the other from the stop detector. Along the first path, the anode output of the start detector is connected to the CFDD START input, where only voltage signals within the range of $[2.25V, 4.21]$ are accepted. After that, a wire is passed from the CFDD's output timing to the TAC's input start, which triggers when it gets the start signal. For the second path, the cable is always linked from the stop detector anode output to the CFDD STOP input where only the signals of $[0.35V, 1.28V]$ pass. Nevertheless, the output timing is connected to a DELY-BOX in order to postpone the signal's arrival and make it appear clear. Between the output of the DELAY BOX and the input Stop of the TAC, the circuit will closed. When the TAC receives the STOP signal will stop recording the voltage signal and convert it to a time signal. Then, it links to a an analog-digital-converter and send it to the MCA for the last step of spectrum accumulation.

Temporel Resolution

The temporal calibration of the spectrometer must be completed before beginning the collection of a positron lifetime spectrum. To determine the spectrometer's temporal resolution, this calibration is necessary. A sealed ^{60}Co source that emits gamma at energies of 1.17 and $1.33MeV$ is used for this calibration. Two different delay values are fixed in the spectrometer's Stop branch during the calibration process. Data is then gathered for these two delay time values. Two Gaussian distributions represent the statistical summing of coincidence events coming from the two energies, $1.17MeV$ and $1.33MeV$. To calculate the value of the channel in time and also of the time resolution from the two Gaussians collected for the delay times of $6ns$ and $12ns$, we proceed as follows : we calculate the values of the widths at mid- heights of the two Gaussians. These values must be equal when the spectrometer is stable. Then, we calculate the value of the channel in time T_0 which is none other than the ratio $(\Delta T/\Delta Ch_{max})$, where ΔT represents the difference of the delay times inserted and ΔCh_{max} the difference of the channels which correspond to the maximum of counts in both Gaussian. The detail of the calculation we performed is as follows :

First Gaussian: $6ns$ inserted delay. Number of counts = 1454 counts, $1454/2 = 727$ counts.

The two channel numbers that are corresponding to that counts are : $Ch_1 = 271$, $Ch_2 = 277 \Rightarrow \Delta Ch = 6$

Second Gaussian: $12ns$ inserted delay. Number of counts = 1328 counts, $1328/2 = 664$ counts

The two channel numbers that are corresponding to that counts are : $Ch_1 = 393, Ch_2 = 399 \Rightarrow \Delta Ch = 6$

The value of a channel in time T_0 : $T_0 = \frac{\Delta T}{\Delta Ch_{max}} = \frac{12-6}{396-274} = 0.0491ns$

Spectrometer time resolution : $FWHM_{temporel} = T_0 \times \Delta Ch = 0.0491 \times 6 = 0.295ns$

Thus the calculated value of the time resolution (instrumental) is $295ps$ and the value of the channel in time T_0 is $0.0491ns/ch$.

Calcul T_0 using MCA

The *MAESTRO* acquisition card: *MCB25(ORTEC)* is used to collect the spectra; the known acquisition concept has been previously described. The signal amplitude will expand along the 1024 channel chain for time spectra. Let's assess the channel time width, also known as T_0 . We vary the delay time at *DELAYBOX* and record the maximum channel each time.

$t(ns)$	2	4	6	8	10	12
Channel _{max}	236.63	278.23	318.12	358.38	399.68	440.68

Table 4.1: Calcul of T_0

After 300-second acquisition period. Finally, using the origin, we plot $T = F(Channel)$ which is demonstrated in figure [4.1.8](#)

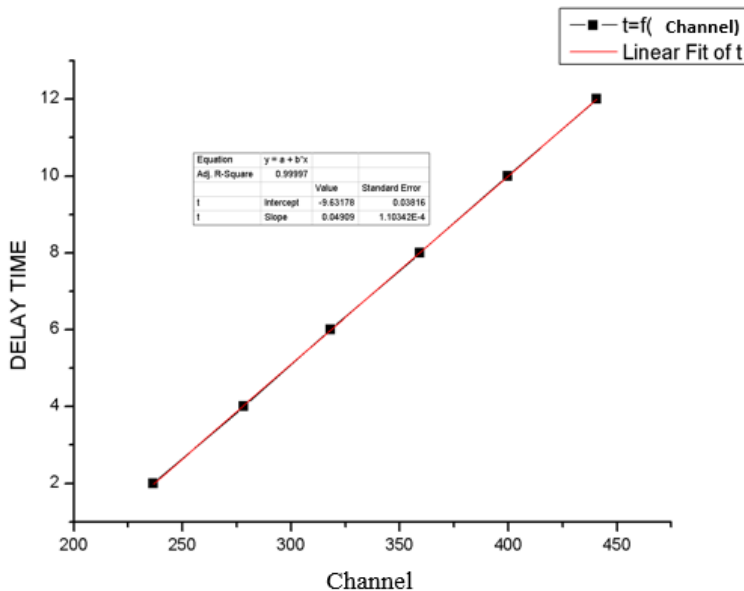


Figure 4.1.8: Evolution of channel in time, T_0

From the plot , we have : $T_0 = 0.0492ns/Channel$.

4.2 PALS-setup with BC418+Burle 8850

4.2.1 High Voltage optimization

We carry out the assembly [4.1.2](#). Then, we varied the generator voltage from $-1900V$ to $-2450V$ and record for each voltage the energy spectrum produced by MCA. The resulting energy spectra are shown in the figures [4.2.1](#) and [4.2.2](#)

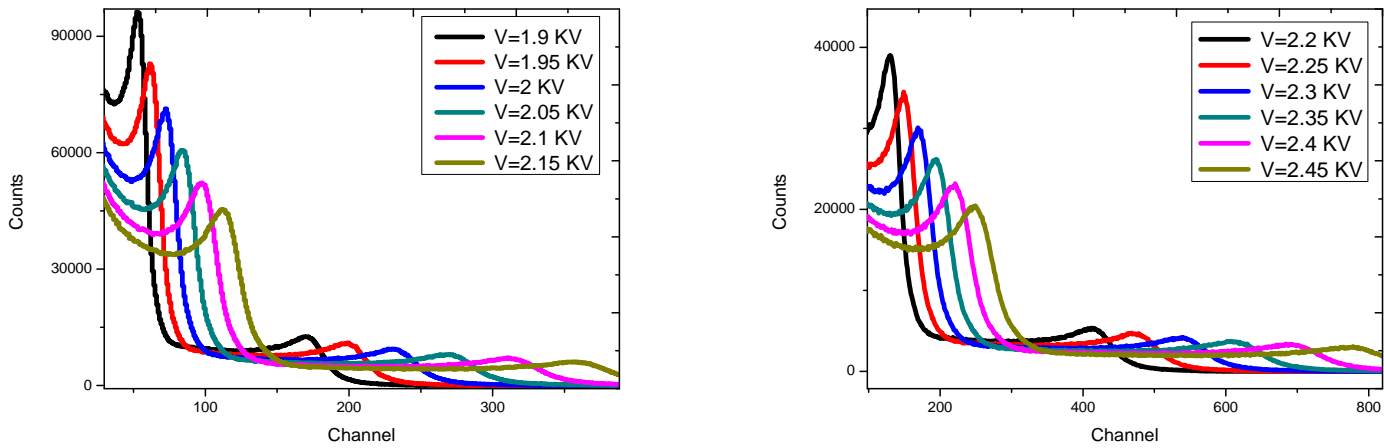


Figure 4.2.1: Energy spectra for the START detector

For the START detector, we choose the voltage that can generate the sharpest $1.28MeV$ peak, and the one that generates an excellent range between the two peaks, so we choose the voltage $-2050V$.

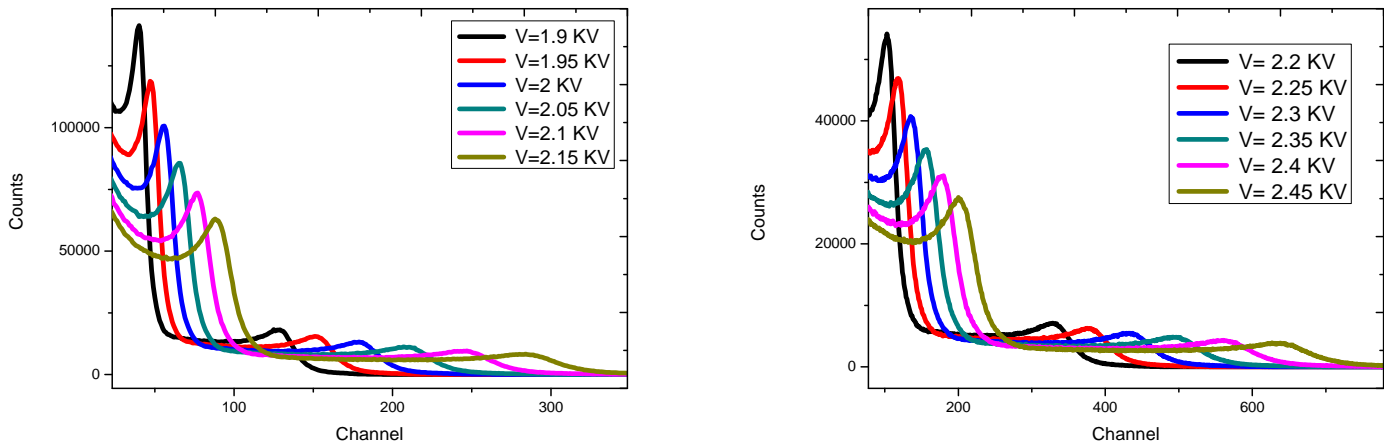


Figure 4.2.2: Energy spectra for the STOP detector

Concerning the STOP detector, we take the voltage which generates the peak, that of the best counting above all, hence the optimal voltage is: $-1950V$.

4.2.2 Energy Selection and Spectrometer Calibration:

We performed energy selection using the oscilloscope mentioned in the Fig. 4.1.2 by setting the potentiometers connected to the start detector and the stop detector as follows: We set the lower level discriminator (LLD) and upper level discriminator (ULD) of the start detector to $2.25V$ and $4.21V$, respectively. The LLD was tuned to $0.35V$ and the ULD to $1.27V$ for the stop detector, respectively. We then went on to calibrate the PALS spectrometer to make sure it was operating at its best. The instrument resolution and counting rate were evaluated as part of this calibration. Using a set-up consisting of a silicon film ($1cm^2$), a radioactive source (^{22}Na), and a second silicon film in the shape of a sandwich and covered in aluminum, we were able to accomplish this. The next geometry (Fig. 4.2.3) is then established once it is cast at one of the detectors' focus.

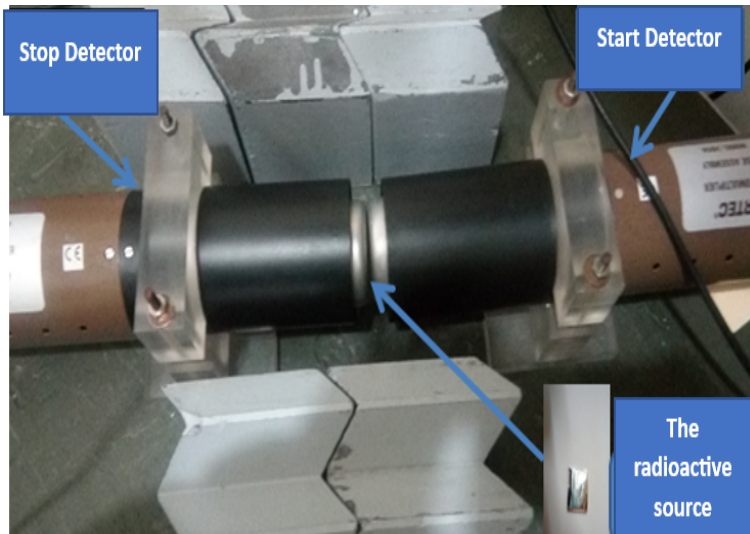


Figure 4.2.3: Detection geometry

We set a 6 ns delay time. The acquisition card level settings were changed to $\text{Nbr/counts} = 10^6$, rating: 60 cps/s , and an acquisition time of $20,000$ seconds. The convolution of the experimental resolution function and the exponential decay sum produces the PALS spectrum shown in Fig. 4.2.4'. The results of our analysis of the PALS spectrum using the LT9.2 program are shown in Fig. 4.2.5'

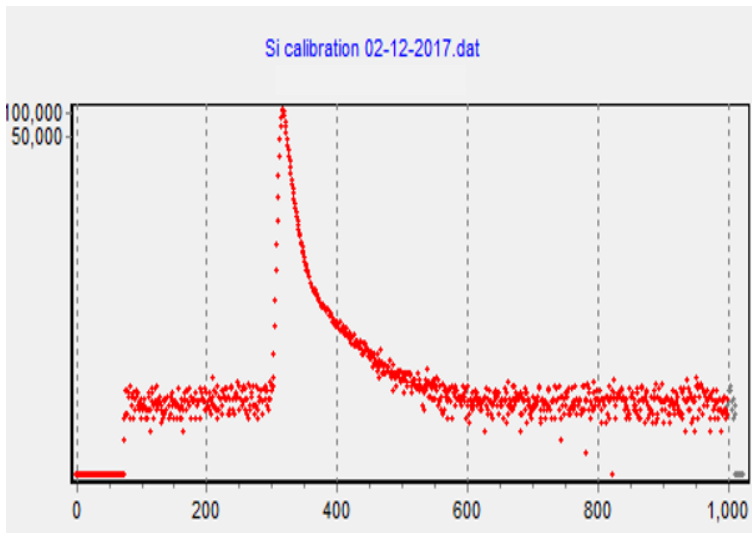


Figure 4.2.4: Silicon PALS spectrum

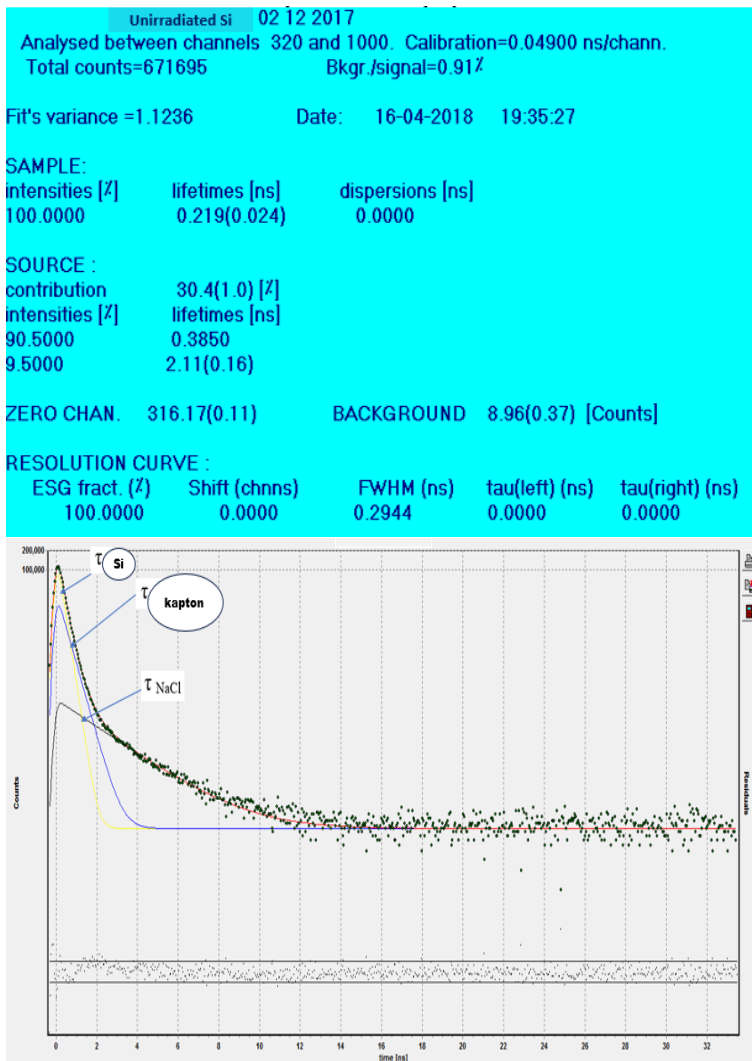


Figure 4.2.5: The fit of unirradiated Si spectrum

The obtained temporal resolution, with a full-width at half-maximum (FWHM) of 0.294 ns,

was, nevertheless, less than ideal. This bad resolution is believed to have a connection to the energy choice. Let's assume that the energy packets merge since the slope on the Gaussian side is male right. We then attempted to manipulate the potentiometers of CFDD in order to enhance the resolution. We changed LLD for the STOP detector from 0.35V to 0.34V and ULD from 1.28V to 1.2V. LLD was changed for the START detector from 2.25V to 2.3V while the ULD was left at 4.21V. The acquisition's settings remained the same. The resolution marginally increased to 0.284 ns after re-acquiring the spectrum, but it was still deemed inadequate. At this point, we changed the way we choose our energy selection and used a Counter-SCA (Single Channel Analyzer) where the potentiometers are fixed to the values indicated in Fig."4.1.6". The resolution remained at 0.278 ns, hence this customize did not result in a significant improvement. As part of our ongoing effort to improve resolution, we changed the polarization voltages for both detectors to -2000V. The results of the selection made are: Start detector :($LLD \rightarrow 2.4V$, $ULD \rightarrow 3.2V$). Stop detector($LLD \rightarrow 0.5V$, $ULD \rightarrow 0.75V$). Despite achieving excellent resolution (FWHM=0.229 ns), the counting rate of 24.88 cps was insufficient for accumulating a spectrum of lifetime. We further adjusted the detector voltages in a subsequent effort, making them -2100V for the START detector and -2050V for the STOP detector. Start detector findings are (LLD=2.6V, ULD=4.5V) and Stop detector results are (LLD=0.5V, ULD=1V). Sadly, this produced the worst resolution of these modifications, which is equal to 0.300 ns. Finally, in our last manipulation, we maintained the voltages, -2050V for the START detector and -2000V for the STOP detector and CFDD potentiometers settings as illustrated in Fig."4.2.6". The fit of the lifetime spectrum is shown in Fig"4.2.7".

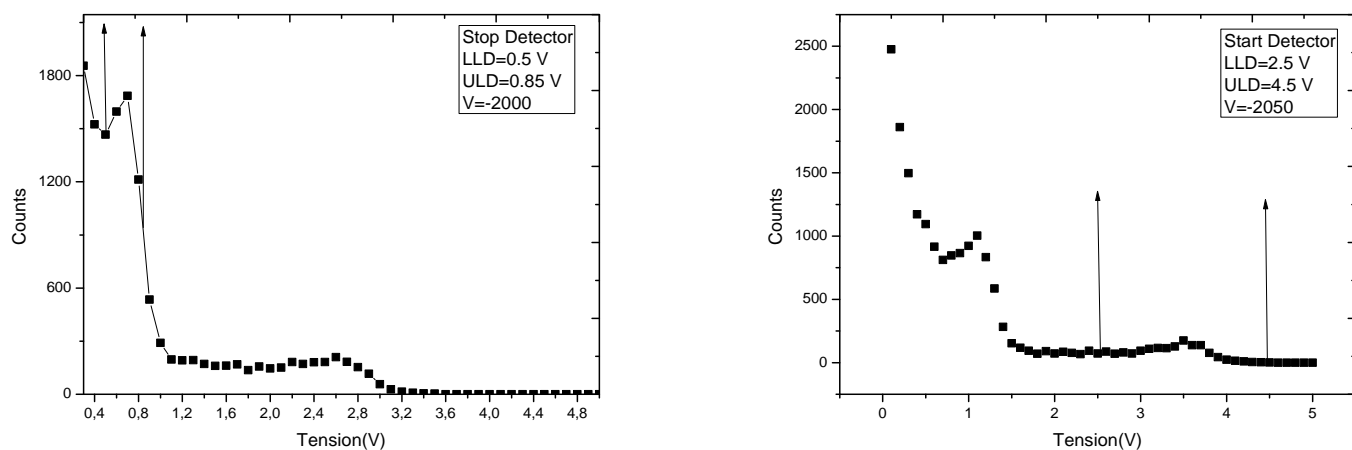


Figure 4.2.6: The best selection energy spectra of BC418

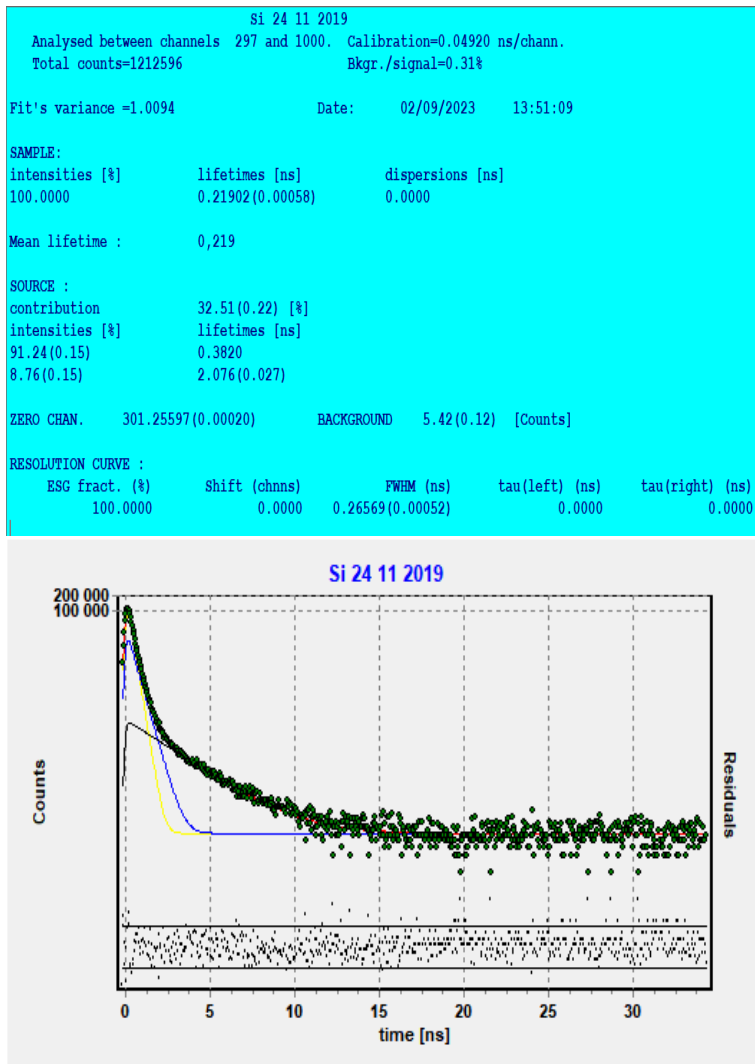


Figure 4.2.7: The fit of the last selection

When the timing resolution was adjusted, it resulted in precision on the order of $0.26569(0.00052)ns$ which is ideal for examining free volumes within polymer materials. This comprehensive evaluation procedure guarantees the PALS spectrometer's dependability and precision for the investigation of free volumes in CR39.

4.3 PALS-setup with (EJ228+H3378-51).

4.3.1 Heigh Voltage optimisation :

We carry out the assembly [4.1.2](#). Then, we varied the generator voltage from $-2000V$ to $-2700V$ and record for each voltage the energy spectrum produced by MCA. The resulting energy spectra are shown in the Fig" [4.3.1](#) [4.3.2](#) :

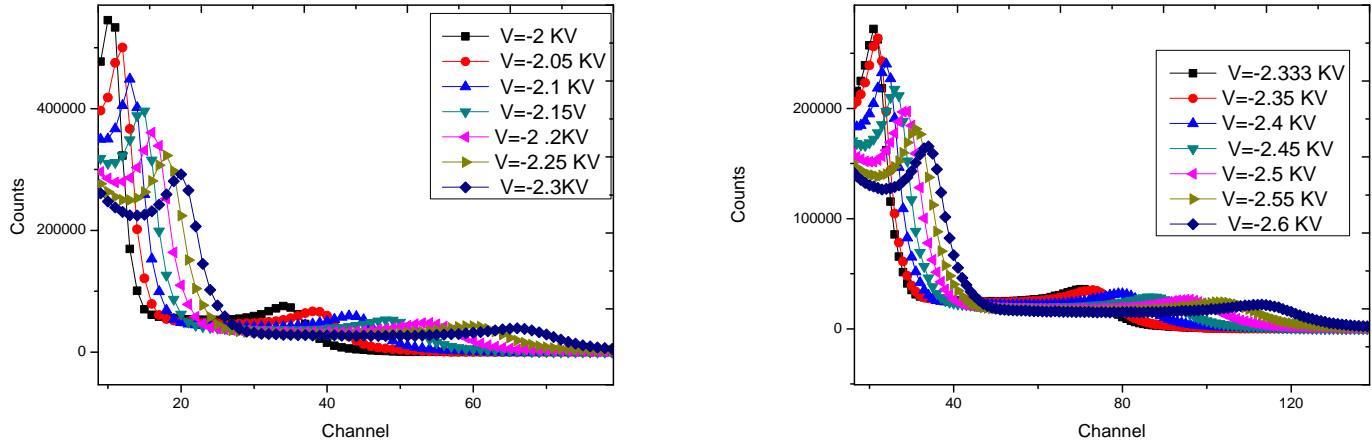


Figure 4.3.1: Energetic spectra for Start Detector

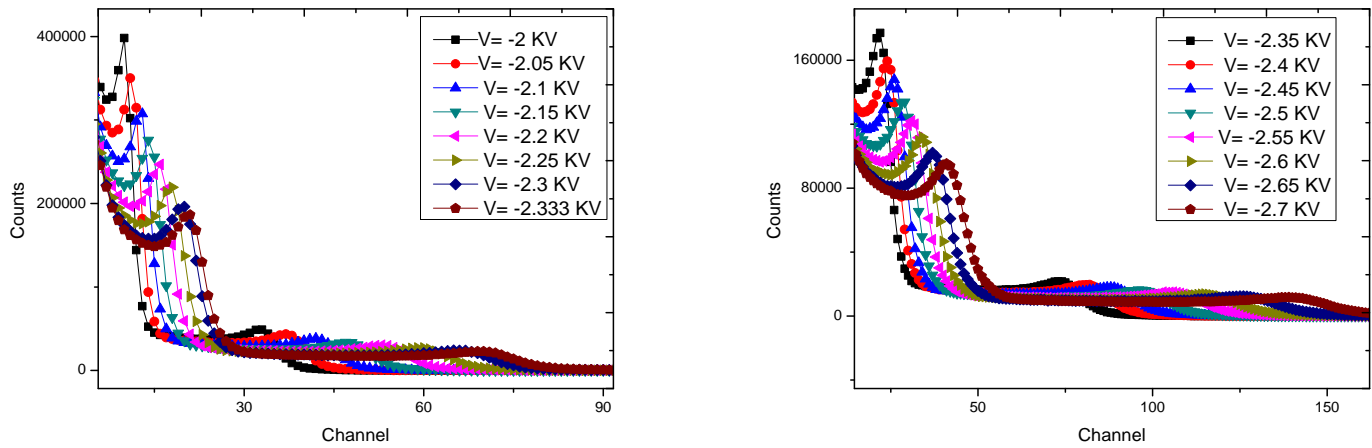


Figure 4.3.2: Energetic Spectra of Stop Detector

According to the spectra, we choose the following voltages. START detector($-2300V$). STOP detector($-2100V$).

4.3.2 Energy Selection and Spectrometer Calibration

The process of selecting the appropriate bias voltages and energy selection were chosen after several iterations with the goal to optimize both the counting rate and resolution. For energy selection in this set of tests, we used the Counter-SCA. We had serious issues with the low count numbers in the initial experiment after plotting the spectra with initially optimal bias voltages. As a result, we made the decision to review our setup by raising the bias voltages. In the subsequent attempt, the START detector was set at $-2450V$ and the STOP detector

to -2350V . This prompted us to set the discriminator windows for the Stop detector at LLD = 0.3V and ULD = 0.55V, whereas for the Start detector they were LLD = 2V and ULD = 4.5V. Unfortunately, we found that this configuration only produced a counting rate of 37 cps, which we deemed to be insufficient. Therefore, in the later trial, we intended to increase the discriminator windows. The CFDD (Constant Fraction Discriminator) settings were changed for the subsequent attempt. LLD and ULD were set to 1.95 and 4.5 volts for the START detector and 0.3 and 0.6 volts, respectively, for the STOP detector. As a result, there was a counting rate of 54 cps and an excellent resolution in the spectrum. However, our goal was to achieve even higher counting rate. In the following attempt, we altered the bias voltages to -2100V for the STOP detector and -2600V for the START detector. Unfortunately, this selection resulted in a PALS spectrum with poor resolution, leading us to discard this configuration. For the next experiment, we raised the polarization to -2450V for the STOP detector and -2600V for the START detector. For the Start detector, LLD = 2V and ULD = 4.5V, and for the Stop detector, LLD = 0.4V and ULD = 0.78V, the discriminator windows were changed accordingly. The resolution for this setup was FWHM = 0.241 ns, and the counting rate was 73 cps. The bias voltages were changed for the latter try to -2100V for the STOP detector and -2600V for the START detector. Unfortunately, this decision led to a PALS spectrum with resolution of 0.300ns, thus we had to abandon this setup. Finally, polarization voltages of -2450V for the START detector and -2250V for the STOP detector were chosen as the best option. Energy spectra of two detectors are shown in the Fig"4.3.3". With the appropriate adjustments to the discriminator windows, a resolution of 0.249 ns and a counting rate of 50 cps were achieved. Consequently, this spectrometer can be used to study the positron annihilation characteristics for CR39 irradiated by alpha particles.

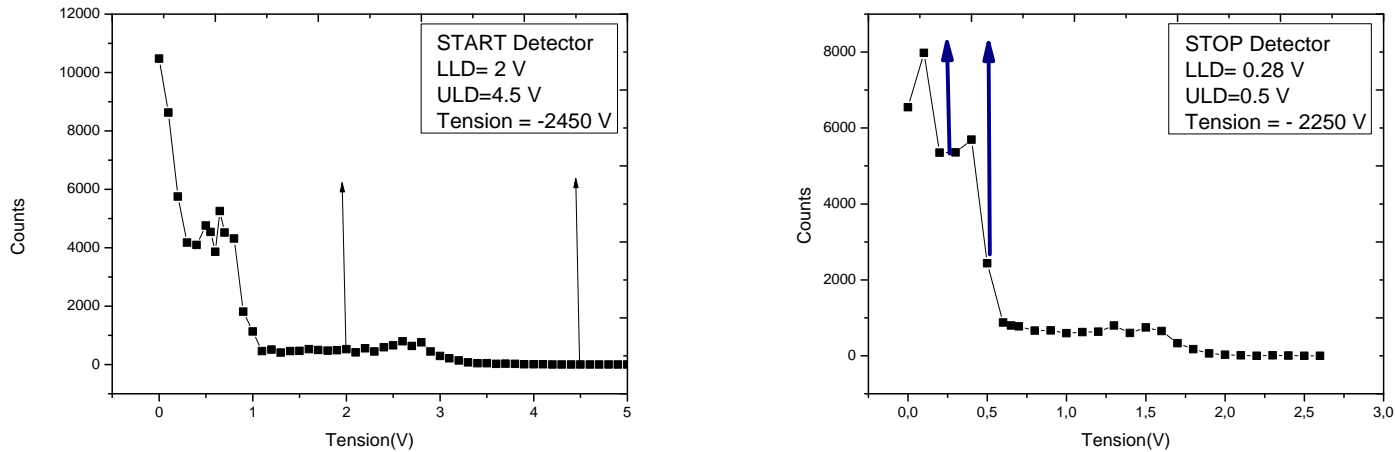


Figure 4.3.3: Energy spectra of start and stop detectors(EJ228)

4.4 CR39 irradiation :

In the project of our thesis we used a CR39 samples manufactured by Pershore Mouldings LTD (UK) with a thickness of $500\mu m$ as demonstrated in Fig."4.4.1". We have prepared three series. The irradiation was carried out in pairs of samples. In one series, the irradiation of CR39 samples was assumed with different fluences of alpha particles where the source used was the ^{239}Pu . We mentionne to that series by the label : $CR39(\neq \Phi)$. For the second series, the irradiation was a function of alpha particle energy using the ^{241}Am source and we indice that series by the label $CR39(\neq E)$. The third series, which also utilised the ^{241}Am source, four samples of CR39 pairs irradiated by following energies (5.48, 4.11, 2.74, 2.28MeV). We call that series, $CR39(\neq E^*)$.

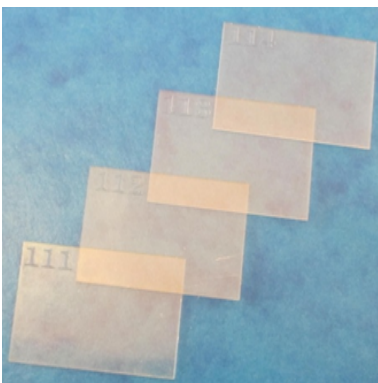


Figure 4.4.1: Unirradiated CR39

4.4.1 The series of different Flunce $CR39(\neq \Phi)$:

The irradiations have been performed using a ^{239}Pu , alpha particles radioactive source ($5.1MeV$) with a collimator of $1cm$ to have an energy of $4.1MeV$ as demonstrated in the Fig"4.4.2". For practical purposes, the irradiations of six pairs of CR39 have been realized with the duration of 1, 2, 3, 5, 7 and 14 days to obtain the following fluencies; 2.6×10^8 , 5.27×10^8 , 7.91×10^8 , 1.3×10^9 , 1.84×10^9 and $3.6 \times 10^9 \alpha/cm^2$.



Figure 4.4.2: Irradiation procedure

4.4.2 The series of different Energy $CR39(\neq E)$:

The irradiation was carried out using the radioactive americium ^{241}Am source which is indicated in the Fig."4.4.3", which emits alpha particles with an energy of $5.5MeV$, during $t = 45$ minutes. The activity of the source used is $5\mu Ci$. In practice, we want the pairs to be irradiated with energies ($4.5MeV$, $3.6MeV$, $2.5MeV$ and $1.6MeV$). In order to achieve these energy values, collimators are used during irradiation, these are wooden devices, placed between the source and the sample. These devices ensure that the samples are only irradiated with certain values. Knowing that the range of alpha particles Using SRIM in the air is $24\mu m$: we can conclude that

$$d = R_{5.5MeV} - R_x \quad (4.4.1)$$

Where d is the length of the collimator, $R_{5.5MeV}$ is the maximum range of alpha in the air R_x presents the energy range we want ($4.5, 3.6, 2.5$ and 1.6). So, thanks to this relationship we conclude the length of the collimators necessary for each irradiation. The values of : d , flux and fluences for the different energies are mentioned in the Table"4.2".

Energy(MeV)	d(cm)	Flux = $\varphi = \frac{A_c}{4\pi d^2}$ ($\alpha/s.cm^2$)	Fluence $\Phi = \varphi.t$ (α/cm^2)
4.5	1	1.47×10^4	3.97×10^7
3.6	2	3682.3248	9.94×10^6
2.5	2.5	2356.6878	6.36×10^6
1.6	3	1636.58	4.41×10^6

Table 4.2: The flux and the fluences of the second serie

The figure” 4.4.4’ demonstrated the fluence variation curve of alpha particles as a function of irradiation distance.



Figure 4.4.3: ^{22}Na radioactive source + ^{241}Am source+CR39 samples

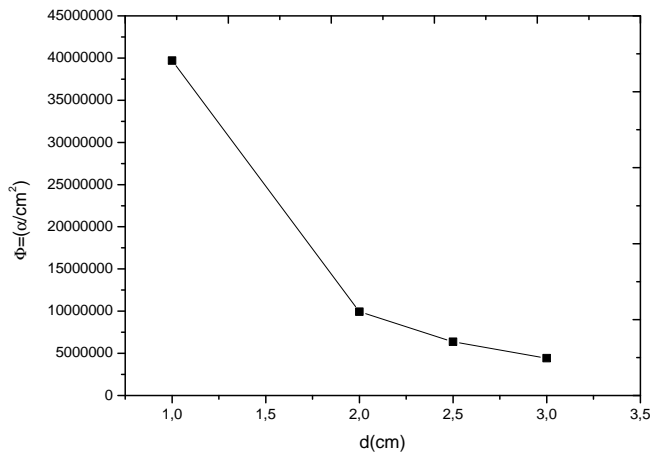


Figure 4.4.4: The fluence variation of alpha particles as a function of irradiation distance

4.4.3 The series of different Energy CR39($\neq E^*$)

In the third series, which involved the ^{241}Am source, four pairs of CR39 samples were exposed to radiation for a total of two hours at energies of (5.48, 4.11, 2.74, 2.28MeV). We call that series, CR39($\neq E^*$). A vacuum chamber was used for the irradiation procedure, and an oscilloscope

was linked to it for recording and reading the energy signals. Fig' [4.4.5](#)' indicates from left to right the vacuum chamber and the irradiation set-up.



Figure 4.4.5: Vacuum chamber+ Irradiation set-up of the third series $CR39(\neq E^*)$

4.4.4 Induced-Alpha damages in CR39

SRIM software (Stop and Range of Ions in Matter) calculates the damage distribution and range of ions ($10eV - 2GeV/amu$) into matter. The rate of energy loss per unit path length is defined by stopping power, represented as (dE/dx) . It includes two types of ion energy loss: nuclear stopping power $(dE/dx)_n$, which is in charge of energy transfer to target nuclei, causing atomic displacements or phonon energy dissipation depending on the energy threshold, and electronic stopping power $(dE/dx)_e$, which involves energy transfer to target electrons causing ionization. The precise calculation of electronic stopping power is still a major focus of experimental and theoretical research. Numerous strategies have been investigated, including analytical formulations for screened Coulomb potentials and universal scattering formulas. The Ziegler, Biersack and Littmark (ZBL) potential is one such universal scattering potential that has been created to explain nuclear scattering and estimate nuclear stopping power over a broad energy spectrum. The TRIM (Transport and Range of Ions in Matter) module of SRIM simulates the distribution of induced damage caused to target atoms by an intense incident ion as it traverses the sample until it comes to rest. Multiple particle histories are tracked within a target during the simulation process of TRIM. These histories have predetermined initial conditions and involve nuclear collision-induced directional changes. Nuclear and electronic losses cause energy to decrease, and histories come to an end when energy falls below a predetermined threshold or when particles escape the target. The "Ion Distribution and Quick Damage Calculation" option is offered for quick damage assessment. Using the Kinchin-Pease formalism, it provides quick statistical damage estimates that take into account the final ion

distribution, ionization energy loss, and energy transfer to various atoms.

Hence, we can estimate the range of alpha particles inside CR39. It gives for $E_\alpha = 4.1\text{MeV}$ the range $21.6\mu\text{m}$ and for 4.5MeV a range of $24\mu\text{m}$ where the Bragg curve peak found within 0.9MeV provide the maximal value of Linear Energy Transfer (LET) as it is demonstrated in Fig. 4.4.6. Figure 4.4.7 demonstrates the ion ranges, the energy transferred by recoils, the phonons energy and ionization energy for $E = 4.5\text{MeV}$. Figure 4.4.8 is showing the 3D distribution of $E = 4.1\text{MeV}$.

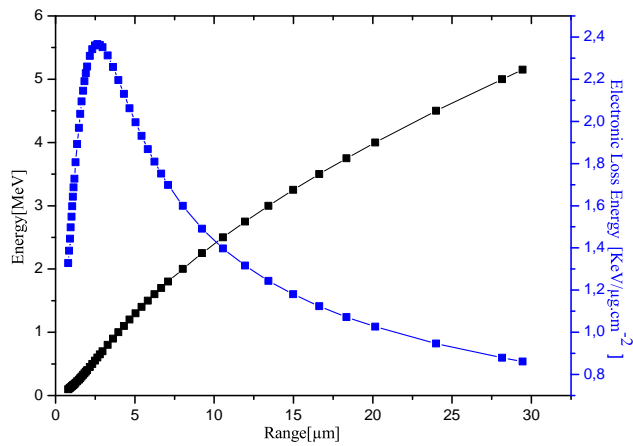


Figure 4.4.6: Bragg Curve and Alpha Energy Versus Range

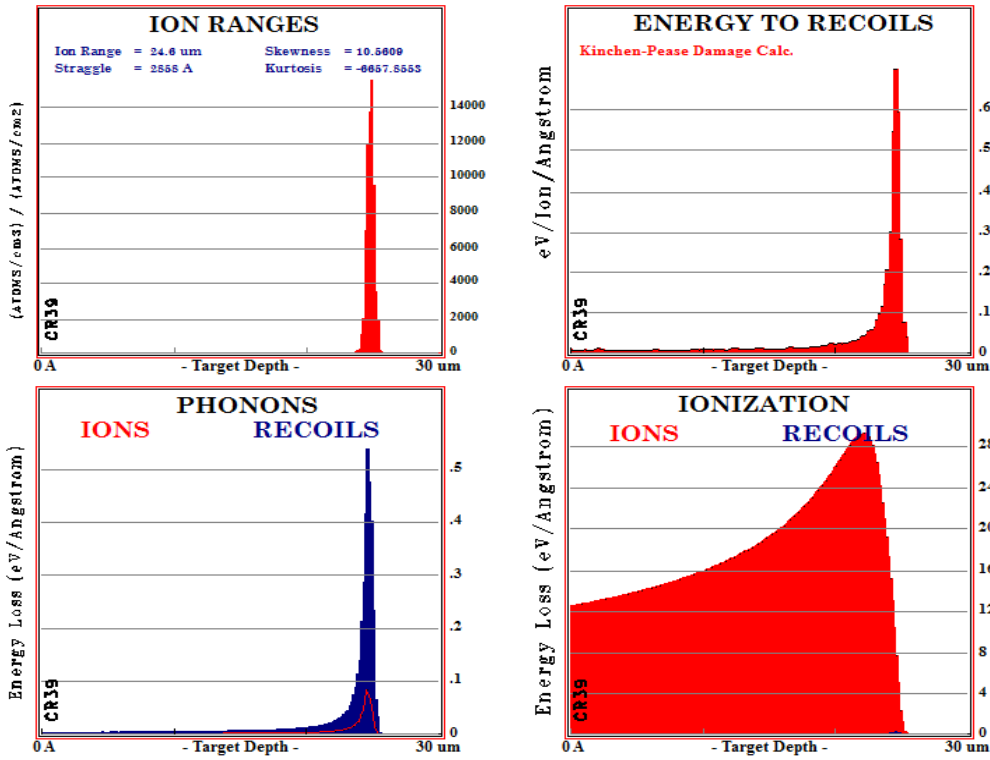


Figure 4.4.7: TRIM simulation plots for $E_\alpha = 4.5\text{MeV}$

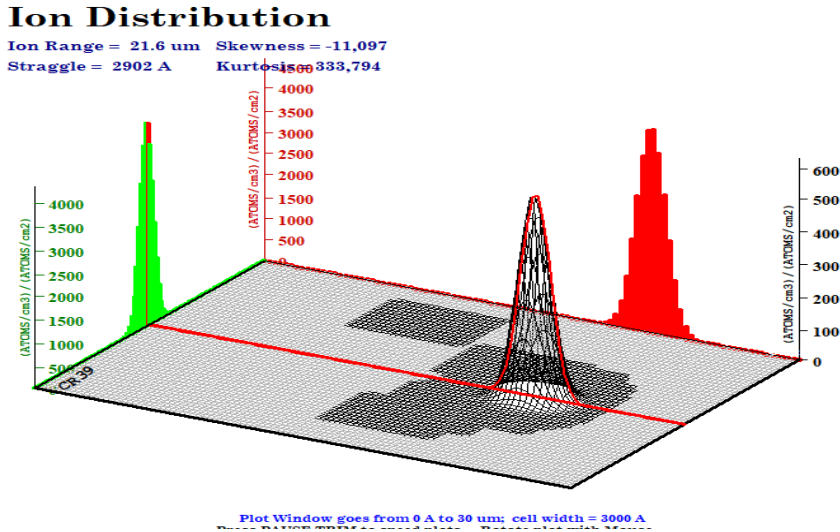


Figure 4.4.8: 3D plot of alpha range distribution for $E = 4.1\text{MeV}$

Moreover, we simulated the dose distribution surrounding the track of alpha particles in CR39 using the formalism of Waligorski demonstrated in *Chapter 3*. This distribution is the result of approaching the doses deposited as it is inside cylinder around the particle's trajectory. During the simulation we were changed the value of the radii from 1 to 10 nm for each fluence. We concluded that the dose distribution gets its outermost radial limit which is called, the track core radii, at 5 nm. As demonstrated in Fig. 4.4.9.

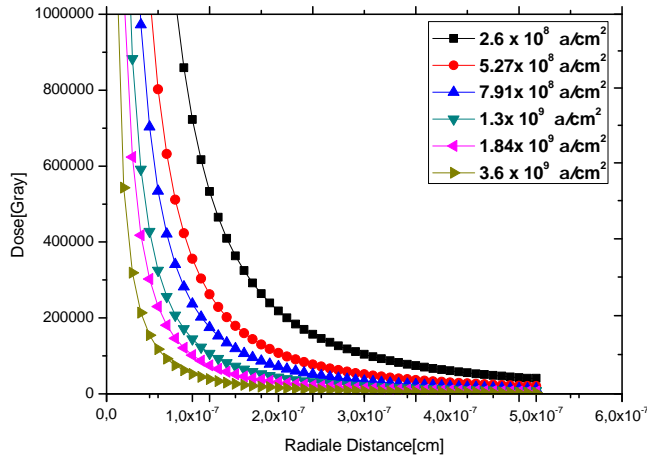


Figure 4.4.9: Radial Dose Distribution Versus Radial Distance

4.4.5 Implantation profile of energetic positron in CR39

In order to estimate the energetic positron profile, we use the relation of Brandt and Paulin 1997 , monted in the formula”[1.2.1](#)”

where z : CR39 thikness in μm . The energetic positron range in CR39 is shown in Fig”[4.4.10](#)”.

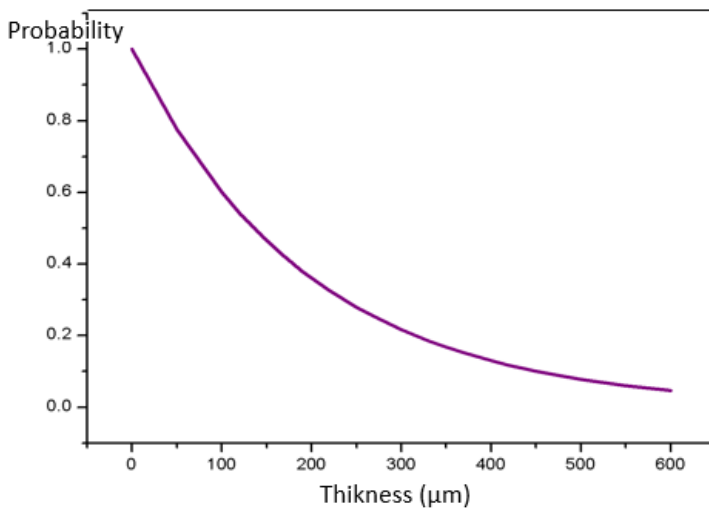


Figure 4.4.10: Positron depth in CR39

4.5 Characterization of $CR39(\neq E)$ series using EJ228 detector based PALS set-up.

4.5.1 Measurements and results discussion

By putting in the form of a sandwich, a film of CR39+ the radioactive source (^{22}Na) + the second film of CR39, in an aluminum cover, the stages of this preparation are indicated in Fig"4.5.1'.

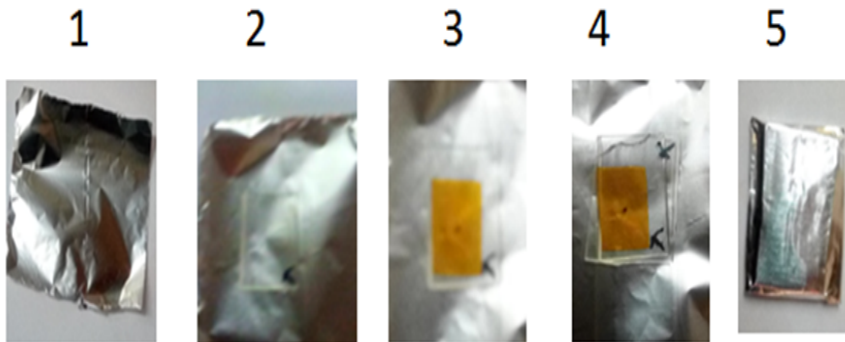


Figure 4.5.1: Sample preparation

After that, we detach it at the focus of one of the detectors. Then we launch the PALS spectrum acquisition which will accumulate 2×10^6 counts. After checking the lifetime in the bulk, we do the measurements for irradiated samples.

The LT9.2 program is used to fit PALS spectra[186]. We employed a single 250ps Gaussian component as the resolution function while fitting lifetime spectra. We considered the use of a two-component source correction. τ_{1s} , or 385ps, the primary source component, was associated with foil annihilations made of kapton. The second source component, $\tau_{NaCl} = 2.14ns$, was assumed to represent the result of annihilations involving the $NaCl$ crystallites. The source contributed 31.28 of the spectrum. The ratio of background to signal was 0.44 percent. Figure" 4.5.2'and Fig" 4.5.3' show the lifetime spectra of CR39 samples.

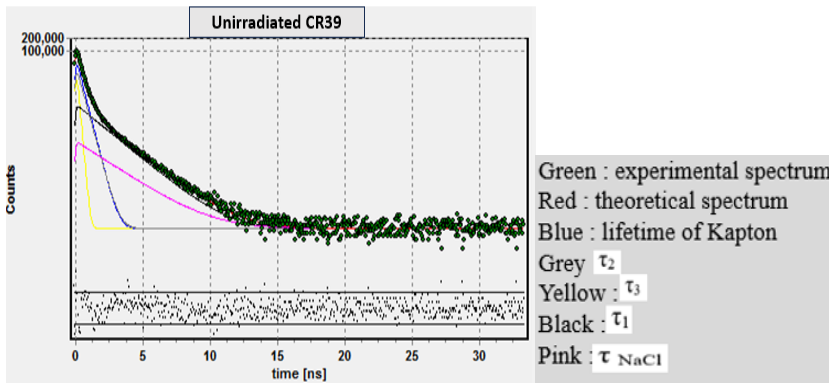


Figure 4.5.2: PALS of unirradiated CR39

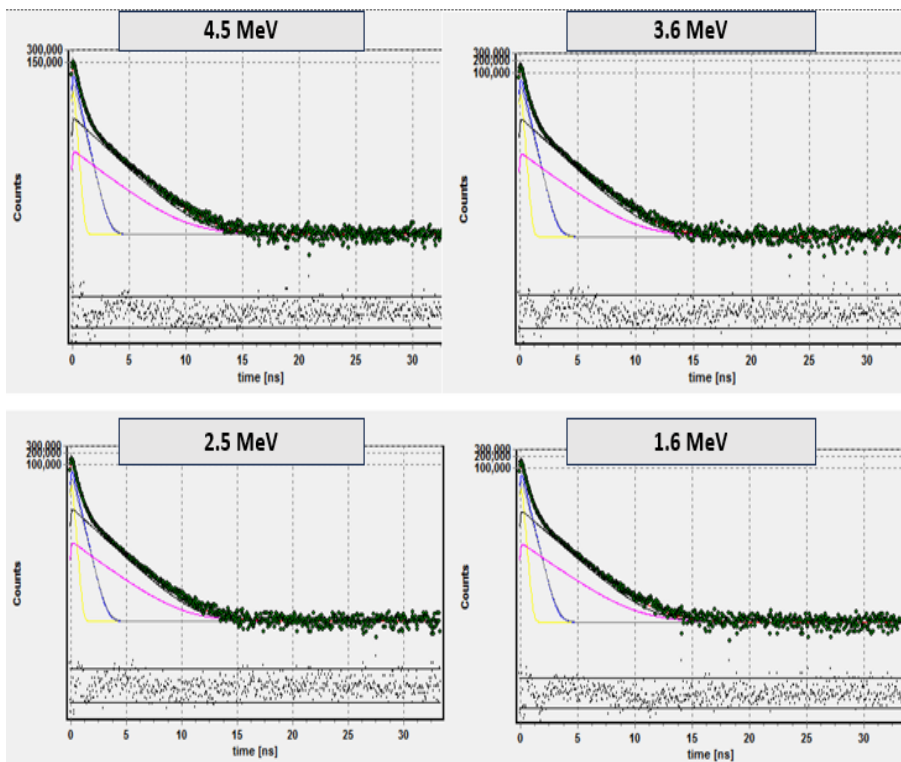


Figure 4.5.3: PALS spectra of irradiated CR39 with different alpha energies

Spectra analysis

After the plot shown in Fig"4.5.4", we identified that the orthopositronium (o-Ps) lifetime value is essentially constant for all samples. The values of I_3 also behave similarly to the o-Ps lifetime component, as seen in Table"4.3". All of these findings suggest that after irradiation, the free volume characteristics did not noticeably change. Two interpretations could be made of this observation. The first hypothesizes that the PALS method may not be sensitive enough to pick up on the tiny alterations brought on by irradiation, though this explanation might not be totally correct. The second argument centers on the fluence of irradiation. It is probable that the fluence applied has little effect on the CR39 material's structural integrity . May be the second recommendation in favor of the second. Therefore, we draw the conclusion that the

lack of detectable changes in the measurements is probably due to the alpha particles' minimal impact at the study's fluence value.

E(MeV)	τ_3	$I_3(\%)$
0	1.719 ± 0.071	22.88 ± 0.25
1.6	1.726 ± 0.068	23.07 ± 0.23
2.5	1.713 ± 0.065	23.02 ± 0.32
3.6	1.722 ± 0.066	22.89 ± 0.3
4.5	1.754 ± 0.068	20.79 ± 0.26

Table 4.3: o-Ps lifetimes and their intensity evolution

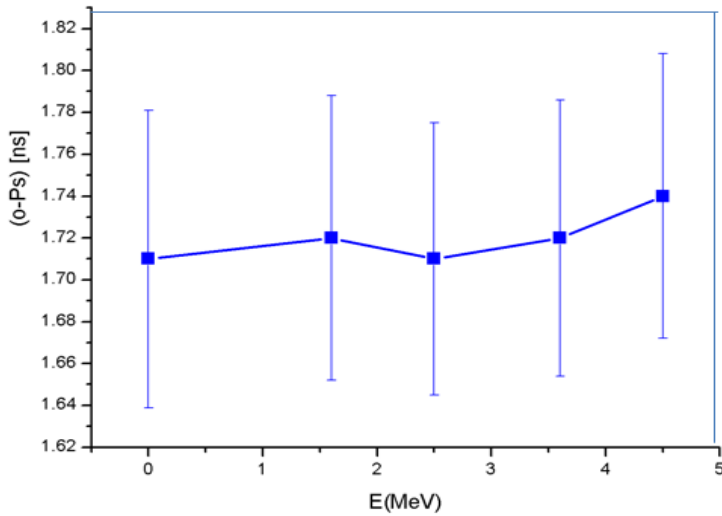


Figure 4.5.4: The variation of lifetime of $o - Ps$ as a function of alpha energy

4.6 Characterization of $CR39(\neq \Phi)$ series using (BC418+Burle885) detector based PALS-setup

4.6.1 Measurements and results discussion

We put the pair of CR39 in sandwich form with the ^{22}Na source, then we detach it at the focus of one of the detectors as we are used to do. Then we launch the PALS spectrums acquisition which will accumulate 2×10^6 counts. PALS spectra are fitted with the program LT9.2[186]. When fitting lifetime spectra, we used a single 270ps Gaussian component as the resolution function. Utilizing a two-component source correction, it was given some thought. The initial source component, τ_{1s} , or 380ps, was connected to annihilations of kapton foil. The second source component, τ_{NaCl} , with is equivalent to 2.07ns, was thought to be the outcome of annihilations involving the $NaCl$ crystallites. 33.07% of the spectrum was provided by the

source. The background to signal ratio was 0.27% . The lifetime spectra of CR39 samples are provided in Fig"4.6.1"and in Fig"4.6.2".

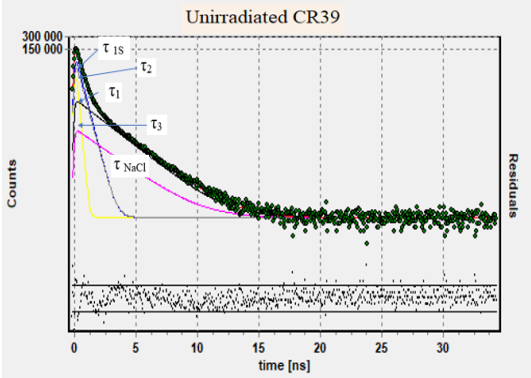


Figure 4.6.1: Lifetime of unirradiated CR39

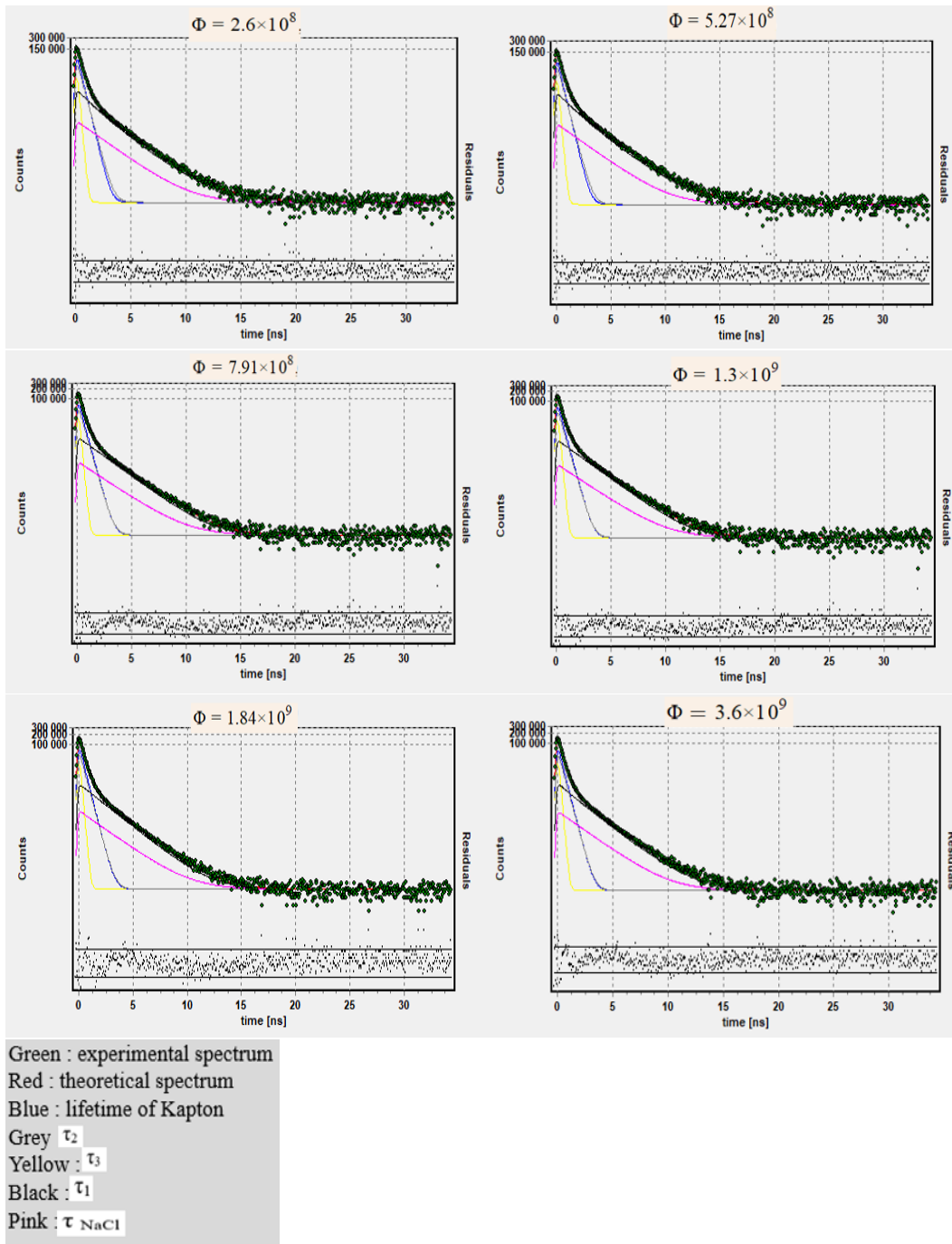


Figure 4.6.2: Lifetime Spectra of CR39 samples

Spectra analysis

After fitting the spectra, we obtain the values of τ_1 , τ_2 , and τ_3 , which are indicative of the lifetimes of $p - Ps$, free positrons, and $o - Ps$ in relation to their intensities and are shown in Table 4.4. The τ_3 has a long magnitude that results from the annihilation of the positron of $o - Ps$ state with an electron media during the pick-off process [187, 188]. Using the Tao-Eldrup model [62, 189], the free volume radius r_h have been calculated.

$$\lambda_{o-Ps} = 1/\tau_{(o-Ps)} = 2ns^{(-1)}[1 - r_h/(r_h + \delta_r) + 1/2\pi \sin((2\pi r_h)/(r_h + \delta_r))]. \quad (4.6.1)$$

$\delta_r = 0.166nm$ [190]. The free volumes are almost spheres. The volumes of free volumes, V of matching radius r_h are determined using the following equation : $V = \frac{4\pi}{3}r_h^3$. The table "4.4" lists the values of r_h , V and F_V which presents the fraction of free volumes. The formula used to determine F_V is :

$$F_V = CV_h I_3 \quad (4.6.2)$$

where, $C = 0.0018$ [169].

Fluence(α/cm^2)	$\tau_1(ns)$	$I_1(\%)$	$\tau_2(ns)$	$I_2(\%)$	$\tau_3(ns)$	$I_3(\%)$	$r_h(A^\circ)$	$V(A^\circ^3)$	$F_V(\%)$	$\sigma(ns)$
0	0.150	17.42 ± 0.20	0.360	60.98 ± 0.11	1.802 ± 0.008	21.60 ± 0.13	2.668	78.79	3.06	-
2.6×10^8	0.148	17.85 ± 0.20	0.360	59.85 ± 0.20	1.796 ± 0.008	22.31 ± 0.16	2.665	79.11	3.17	0.51
5.27×10^8	0.125	17.61 ± 0.13	0.360	60.11 ± 0.10	1.809 ± 0.009	22.28 ± 0.11	2.668	78.79	3.15	0.10
7.91×10^8	0.125	13.12 ± 0.07	0.342	62.68 ± 0.07	1.723 ± 0.009	24.19 ± 0.06	2.550	63.31	3.01	0.20
1.3×10^9	0.125	12.56 ± 0.10	0.342	65.16 ± 0.10	1.775 ± 0.007	22.29 ± 0.10	2.668	78.79	3.16	0.20
1.84×10^9	0.125	13.32 ± 0.07	0.342	62.20 ± 0.07	1.784 ± 0.006	21.90 ± 0.11	2.650	77.78	3.06	0.20
3.6×10^9	0.150	17.26 ± 0.30	0.360	61.05 ± 0.30	1.802 ± 0.007	21.70 ± 0.15	2.631	76.04	2.97	0.41

Table 4.4: Positron annihilation lifetime data for alpha irradiated CR39

According to the examination of the spectra, the non-exponential character of the long-lived component τ_3 can be attributed to a lifetime distribution carried by a size and shape distribution of free volume holes. By include a dispersion , σ , in the value of τ_3 , LT 9.2 allows for the analysis of continuous lifetime distributions. The dispersion that is mentioned for the irradiated samples in the table "4.4". According to [165], the standard deviation caused the logarithmic Gaussian distribution of each channel's $\alpha_i(\lambda)$ takes the following form :

$$\alpha_i(\lambda)\lambda d\lambda = \frac{1}{\sigma_i(2\pi)^{1/2}} \exp \left[-\frac{(\ln(\lambda) - \lambda_{i0}\ln(\lambda))^2}{2\sigma_i^2} \right] \quad (4.6.3)$$

where

$$\lambda = 1/\tau_3 \quad (4.6.4)$$

This means that the following formula [161] might be used to simulate the free volume radius distribution, $f(R)$, as shown in Fig. "4.6.3":

$$f(R) = 2\Delta R \{ \cos [2\pi R / (R + \Delta R)] - 1 \} \alpha(\lambda) / (R + \Delta R)^2 \quad (4.6.5)$$

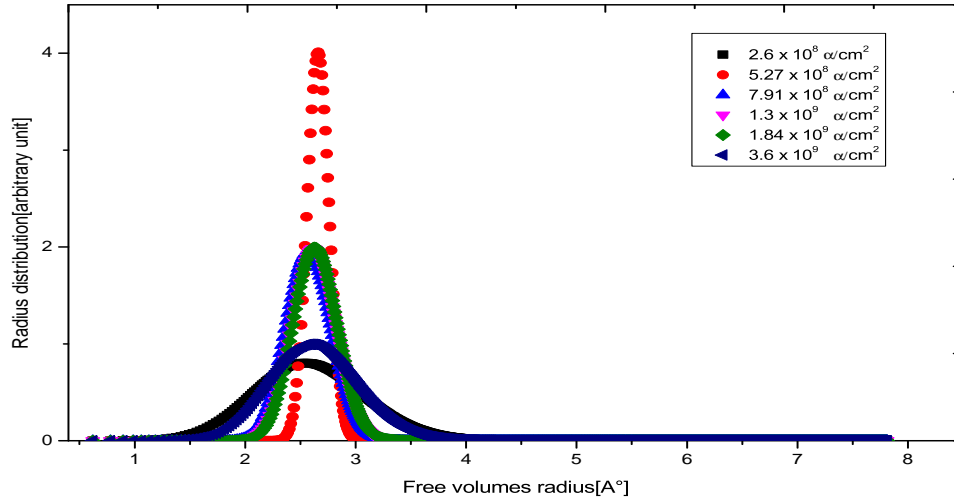


Figure 4.6.3: Free Volume Radius Distribution

The variations of τ_3 and r_h were shown in Fig"4.6.4" against alpha particle fluencies.

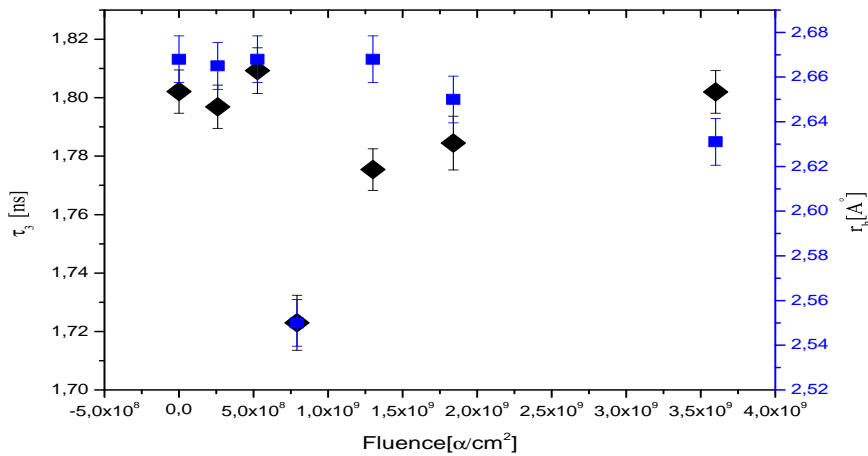


Figure 4.6.4: Variation of τ_3 and free volume radius, r_h Versus Fluence

There is a reduction between the unirradiated sample and the third fluence value, from $1.8025 \pm 9.4 \times 10^{-3} ns$ to $1.7231 \pm 9.4 \times 10^{-3} ns$. There is subsequently an increase until the fourth fluence value, when τ_3 gets the value of $1.7772 \pm 9.4 \times 10^{-3} ns$, following which it stabilizes. The change in free volume radius and the concentration of the long-lived component in the network structure are virtually invariably associated with one another [24].

The free volume radius' profile variation exhibits the same traits as τ_3 . Between the unirra-

diated sample and the third fluence value, the radius decreases from $2.668A^\circ$ to $2.550A^\circ$, and then increases to the fourth fluence value, when it is given the value of $2.668A^\circ$. In addition, the long-lived component's intensity is rising from 21.6 to 24.19 in the same range as the free volume radius is contracting. τ_3 or the free volume radius could be used to express the impacts of alpha particles. The cross-linking yield will rise when there is a high probability of overlap between the generated radicals. Consequently, there may be a drop in τ_3 , the long-lived component. In the event that the randomly dispersed deposited energy separates the damaged regions spatially. Due to the increased likelihood of bond scission, we see an increase in the free volume radius [166].

4.6.2 Comparison between the F_V derived from PALS and a computed F'_V using the Waligorski Calculation method :

The Waligorski calculation [191] [192] was used to determine the radial distribution of alpha doses around their trajectory as like indicated in Fig "4.4.9" provides a clear illustration of how the distribution of these doses varied for each irradiated sample. This distribution results from approaching the doses that are deposited as they are contained inside the cylinder that surrounds the particle's trajectory and creates the track core. For each fluence, we adjusted the value of the radii from 1 to 10 nm during the simulation. We came to the conclusion that the dose distribution's outermost radial limit, known as the track core radii, occurs at $5nm$. Chemical bonds in the track core have broken, causing free volumes to develop. Additionally, it might contain chain ends and new compounds created by cross-linking or bond scission. The track core is spread inside a cylindre with a radius of $r = 5nm$ and a length that corresponds to the range of alpha particles, $R_p = 22\mu m$, according to the simulation that was actually carried out.

We prepare the following calculation to determine the accuracy of this model: If we assume that all of the free volumes are confined within a cylinder with radius r and length l in the context of the model. The range of alpha particles, R_p , is equal to the length of the cylinder. The radius is the same as the radius of the entire free volume. The free volume radius of each sample might be multiplied by the related free volume fraction F_V to get the total free volume radius. The following formula is used to get the volume of the cylindre containing all of the free volumes, V_{FV} , $V_{FV} = \pi(r_h F_V) 2R_p$: The track core volume is given by $V_{TC} = \pi(5) 2R_p$. By dividing V_{FV} by V_{TC} , we arrive at the amount F'_V , which agrees with F_V by (78-89)%. The values of rF_V and F'_V are shown in the table" 4.5". In fact, there is a good deal of

agreement between the resulting F'_V values and the free volume fractions obtained using PALS, demonstrating that there is a reasonable agreement between the distribution of radial damages and the results of PALS.

$Fluence(\alpha/cm^2)$	$F_V(PAS)(\%)$	$rF_V(A^\circ)$	$F'_V = \frac{V_{FV}}{V_{TC}}(\%)$
2.6×10^8	3.17	8.44	2.84
5.27×10^8	3.15	8.4	2.82
7.91×10^8	3.01	7.67	2.35
1.3×10^9	3.16	8.43	2.84
1.84×10^9	3.06	8.1	2.62
3.6×10^9	2.97	7.81	2.43

Table 4.5: F_V the fraction of free volumes for irradiated samples. rF_V the total free volumes radius. F'_V the new calculated free volumes fraction

4.7 DBS Experiments :

In the scope of our thesis, The HP-Ge (High-Purity Germanium) Coaxial Detector System with an excellent resolution of $1.6keV$ for $1.33MeV$ gamma rays from ^{60}Co was used to establish the DBS spectrometer. This main objectif of the spectrometer was to find the Doppler broadening spectra connected to the $511keV$ photon gamma annihilation process. The longitudinal momentum density component can be qualitatively described using DBS. This is done by measuring the Full Width at Half Maximum ($FWHM$) of the photon gamma line produced by the annihilation of positrons with an energy of $511keV$ [24]. This measurement offers important insights into the electron density momentum distribution at the annihilation sites because the positrons in this situation are already thermalized. This characterization is well-known and is based on shape (S , the shape parameter), wings (W , the wing parameter) as described in **Chapter 2**. This section describes the study's calibration steps for the DBS setup and how to prepare it for characterizing irradiated samples. Calibration is a crucial step in order to ensure the accuracy and dependability of the DBS measurements when determining out the electron momentum distribution.

4.7.1 DBS set-up and calibration

Using a constant calibration material like silicon, the calibration procedure for the experiment appears to carry out consistently. The following process are assumed to calibrate the setup. After making sure the assembly, as depicted in Fig."4.7.1", we went on to polarize the detector by utilizing a bias supply module and delivering a voltage of $+1700V$. Then, we placed the

sample in the prepared sandwich form in front of the detector's entryway. A fixed spacing of 7cm must exist between the sample and the detector. After this polarization, we made the necessary corrections as shown in the table [4.6](#) at the level of the amplifier. These adjustments are critical to fine-tune the detector and amplifier settings for optimal performance. Then, we run the spectrum acquisition for 20min. The two 511keV pic obtained from the adjustments shown in the table are figured in Fig [4.7.2](#).

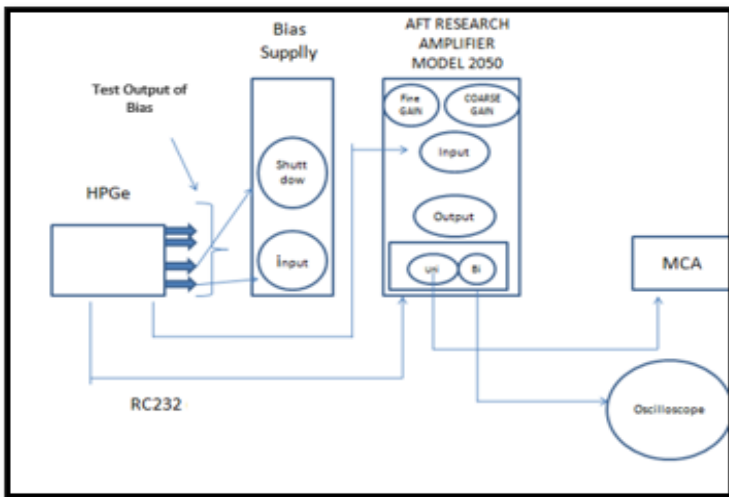


Figure 4.7.1: DBS set-up

Fine Gain	Coarse Gain	Channel _(max)
15	50	3100
8	100	3280

Table 4.6: Regularities parameters

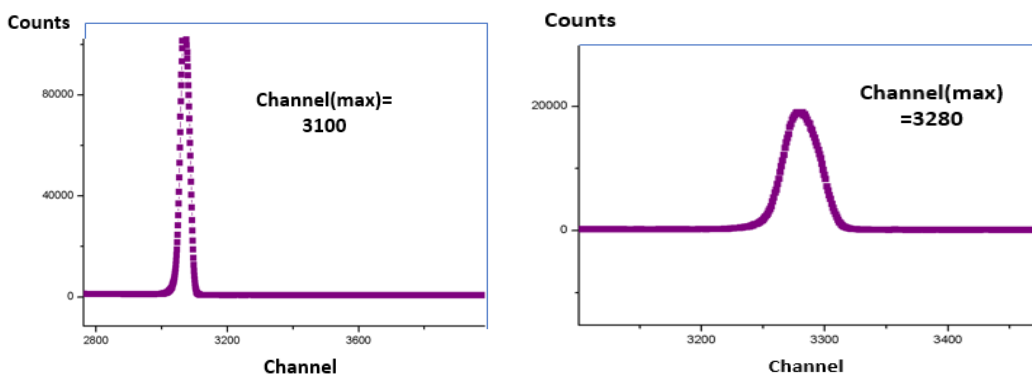


Figure 4.7.2: Spectrum of DBS calibration

The calibration of the spectrometer involves analyzing the parameter S (shape parameter) which is crucial for understanding the characteristics of the Doppler broadening spectrum. The *SP.1.1* software calculates these parameters based on the values of dS and dW determined in the spectrum as it is explained in *Chapter 2* and shown in the Fig."4.7.3". To achieve a specific value of 0.5 for the S parameter, we make adjustments to the experimental setup. Here are the required tasks.

- Starting S value is established.
- Adjust experimental parameters like detector settings or sample preparation.
- Compile data using the modified settings.
- Review the updated S value in light of the fresh information.
- Repeat steps b through d up until S gets close to 0.5

Keep the changes and how they impact the S value. It may take time and careful fine-tuning of the experimental setup to achieve the desired value of S .

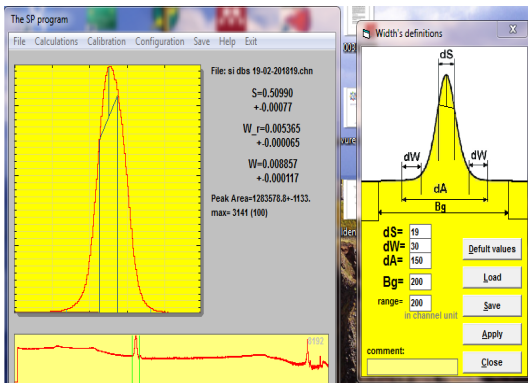


Figure 4.7.3: DBS(Si) spectrum

4.8 DBS Characterization of CR39($\neq E$)

We prepare the film1(CR39)+source+film2(CR39) sample in sandwich form. Then, we place it 10cm away from the HPGe detector, and launch the acquisition set. We vary the values in the configuration as they appear clear in the simulation figure, provided that the parameter S never takes the value of 0.5, it is an upper limit for this parameter. The DBS spectra are fitted by *SP.1.1* and shown in Fig"4.8.1"

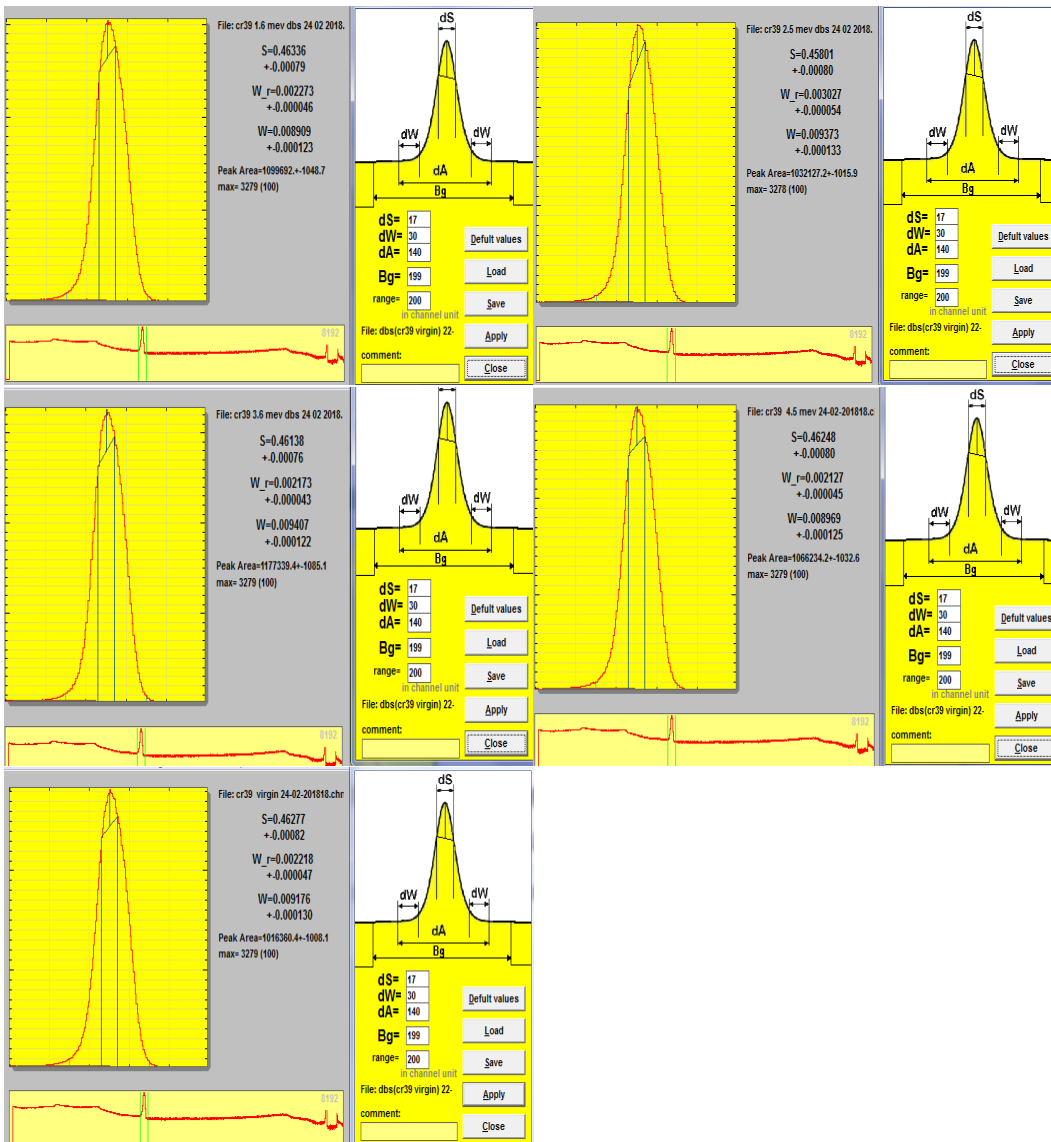


Figure 4.8.1: DBS spectra of irradiated CR39

Figure “4.8.2” displayed superposition of DBS(CR39) 511 KeV pics for different alpha particles energy.

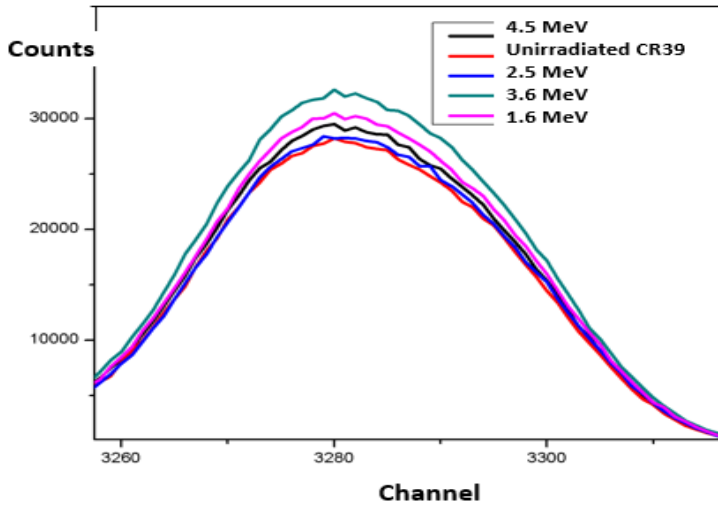


Figure 4.8.2: DBS(CR39) spectra superposition

Figure 4.8.3 displayed the S parameter variations against alpha particles energies.

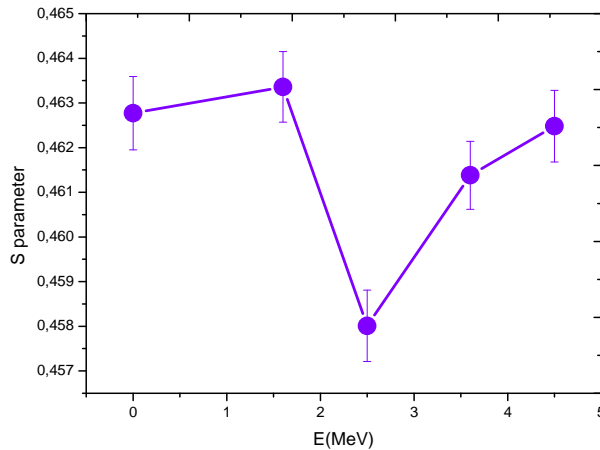


Figure 4.8.3: The S parameter variation curve as a function of alpha particle energy

Spectra analysis

The calibration verified that $S_{bulk} = 0.4855$ by taking $dS = 18$ channel, For the spectrum : We noticed that the parameter value S increases in the energy interval $[0-1.6 \text{ MeV}]$ from the value 0.4855 to 0.48618 . Then, the parameter decreased in the interval $[1.6 - 2.5 \text{ MeV}]$ from 0.48618 to 0.48397 . Afterwards, we note an increase in the range $[2.5, 4.5 \text{ MeV}]$ where the parameter S reaches its maximum value, 0.48622 . The physical phenomena which cause the variation of the parameter S are the scission and crosslinking of molecular chains. However, the parameter S expresses the fraction of positrons which annihilate with the valence electrons, which leads to their increase coinciding with the existence of defects, for our case (Free Volumes). Therefore,

the increase in S results in the phenomenon of scission of molecular chains. On the other hand, the decrease in the S value is in fact equivalent to the lack of valence electrons, the fact which suggests that the chains will crosslink. Reduction of S , cross-linking of molecular chains takes place.

4.9 DBS Characterization of $CR39(\neq \Phi)$

After assuming the DBS calibration silicon as in the precedent experiment. We do measuring the DB for all samples of series $CR39(\neq \Phi)$. The DBS spectra are fitted with SP.1.1 as usual. Then we plot the variation of S and W . The variation of S as it is shown in Fig."4.9.1" has a fluency against the alpha irradiation fluences, reaching a minimum value of 0.46781 at a fluence of 7.91×10^8 . Conversely, the parameter W exhibits an inverse fluency trend in the same range, peaking at a maximum value of 0.0013 for the same fluence.

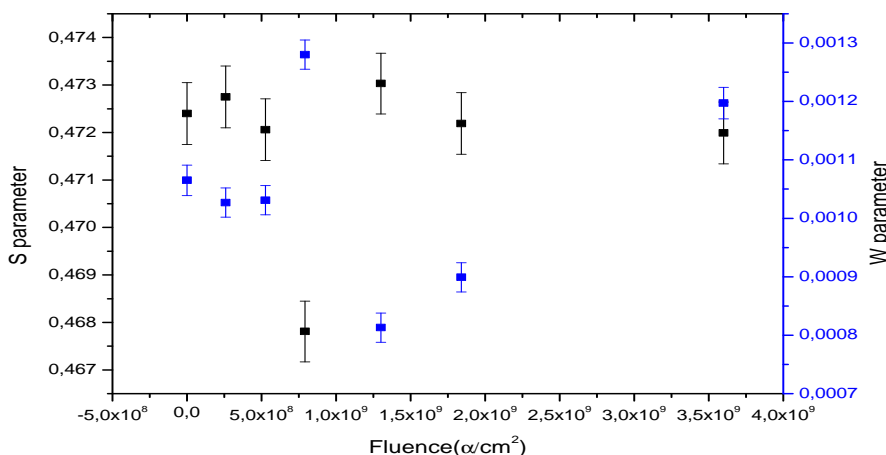


Figure 4.9.1: Variation of the S and W parameters Versus the Fluence

The S-parameter's increasing trend implies that the size of free volumes in the system has significantly increased. This phenomenon may be caused by the expansion that takes place both within and between the molecular chains, most likely as a result of an increase in the bond-scission cross-section. On the other hand, the observed drop in this parameter may point to a decline in the quantity or size of free volumes in the system. The cross-linking procedure seems to be closely related to the decline in these free volumes. It's important to note that S typically describes low-density areas, whereas W primarily describes high-density areas. While concurrently showing the sensitivity of W in low-density zones, the inverse relationship between

both parameters emphasizes the crucial function of S in capturing changes within those areas.

4.10 Etched CR39($\neq \Phi$) characterization by (BC418+Burle885) detector based PALS-setup and DBS :

By employing the PAS technique, we can characterize the latent tracks via the parameter of free volume radius or S-parameter without an obligated need to reveal the latent tracks in somehow get visualized under the microscope. Alternatively, We conducted an experiment where assuming the etching of samples for 5 minutes, then PALS and DBS measurements were carried out. Moreover a visualisation under the Optical Microscopy(LEICA DM5500B) has been made.

4.10.1 Etching experiment :

A *KOH* (potassium hydroxide) solution was used to perform a chemical etching operation for 5 minutes. The etching procedure is depicted in the Fig”4.10.1”. To perform chemical etching, the samples were submerged in a thermal bath that contained a basic solution. To ensure their homogeneity during the etching process, the solution was constantly stirred. According to [170][171], the concentration and temperature values were tuned to be $C = 6.25N$ and $T = 70 \pm 2^\circ C$. As the temperature and concentration increase, the etching rate increases exponentially. This behavior shows how sensitive the etching process is to changes in temperature and concentration, which can greatly affect how quickly material is removed[172] [173]. The detectors were thoroughly washed in distilled water following the etching process, dried to stop the etching process, and to get clean from the components of the basic solution. The PALS and DBS measurements have been performed in the same conditions for the etched samples.



Figure 4.10.1: Etching experiment

4.10.2 Effects of Etching in S , W parameters and positronium lifetime/free volume radius

We provide a thorough study of the profile variations in S , W parameters and positronium lifetime/free volume radius for both the etched and non-etched samples. The profile variation of τ_3 is shown in Fig. 4.10.2, which sheds light on its behavior under etching. Figure 4.10.3 explores the free volume radius and provides details on how it changed. Fig. 4.10.4 and Fig. 4.10.5 also shows a thorough view of the S and W parameters respectively. It illustrates how they change in response to etching. Together, these measurements offer a clear and insightful comparison between the etched and non-etched samples, enabling us to understand how the etching process affects these parameters.

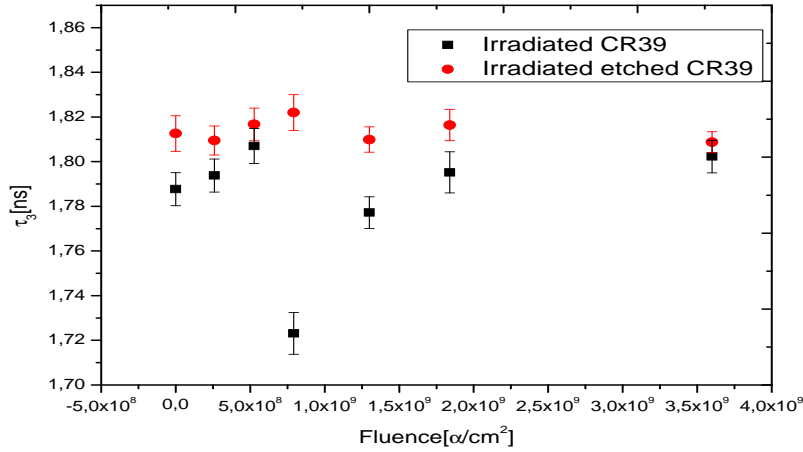


Figure 4.10.2: Variation of τ_3 Versus Fluence for etched and no-etched samples

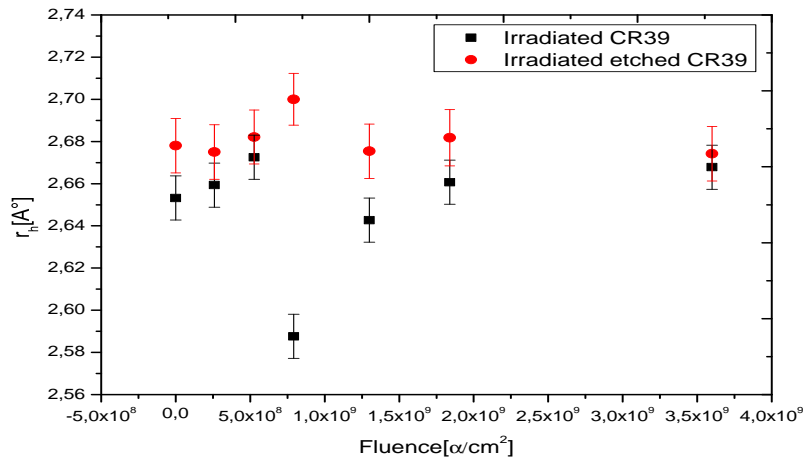


Figure 4.10.3: Variation of free volume-radius versus fluence for etched and no-etched samples

In the Fig."4.10.4", we note that there is a noticeable rise in S parameter for the etched samples. In contrast, Fig."4.10.2" and Fig."4.10.3" show a more light increase in their respective variables. A remarkable inverse relationship with fluences emerges when the variation of the W-parameter in the etched samples is examined; this relationship is noticeably different from the pattern seen in the non-etched samples (see Fig."4.10.5"). These findings highlight the particular impacts of etching on the parameters under investigation.

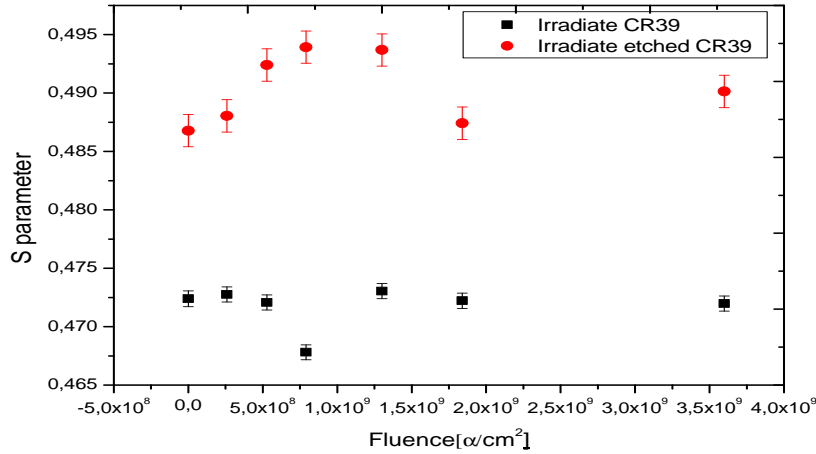


Figure 4.10.4: Variation of S-parameter Versus fluence for etched and no-etched Samples

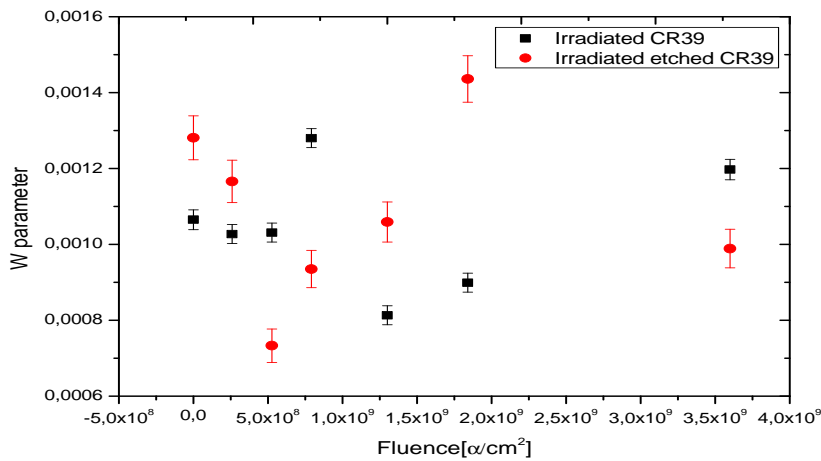


Figure 4.10.5: Variation of W-parameter Versus fluence for etched and no-etched Samples

We stress the difference between the S-parameter and the long-lived component of τ_3 , emphasizing that S demonstrates a greater sensitivity to changes in electron density than τ_3 . The observable changes in the annihilation parameters in the etched samples highlight how sensitively the PAS technique can track the birth tracks. This sensitivity is made even more clear when compared to the optical microscopy (LEICA DM5500B) limitations, as seen in Fig. 4.10.6. In contrast to optical microscopy, which normally requires at least an hour of etching time to visualize the tracks [177] [193], PAS enables their detection in less time, as shown above. We suggest that, if we use incremental etching steps over a wider time range, PAS's sensitivity in recognizing birth tracks may be used to potentially deduce a link between

the free volume radius and the diameter of etched tracks. This exciting direction may provide important information about track evolution and characterization.

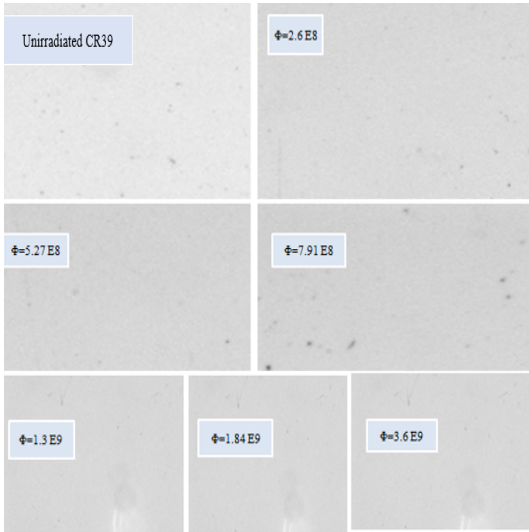


Figure 4.10.6: Etched samples under optical microscopy

4.11 CR39($\neq E^*$) series characterization by VEDBS

In this section, we attempted to highlight the significant outcomes of the internship in the Physics Department of MARMARA UNIVERSITY's Faculty of Arts and Sciences. The internship was carried out between October 15 and November 14, 2018, and it was expertly supervised by Professor Dr. Ugur Yashi. Our primary focus while working under his guidance was to get a thorough understanding of beam positron spectroscopy. Our main objective was to become proficient in using a challenging positron beam system. This increased our level of expertise in the sector by requiring us to work directly with complex instrumentation and experimental setups. Moreover, we analyzed the sample series of CR39($\neq E^*$).

4.11.1 Beam positron depth in CR39

Using the formula of the mean depth represented in **Chapter 1**, the mean depth of slow positrons in CR39 is estimated using the equation $d = \frac{A}{n \cdot \rho}$ where "d" is the density of CR39 which is equal to 1.32 gm/cm^3 . $A = 4 \mu\text{g.cm}^{-2} \cdot \text{KeV}^{-n}$ et $n=1.6$. It's crucial to remember that the precise values of 'A' and 'n' in this function depend on the subject matter being examined. With the aid of MATLAB, we created a program to simplify this analysis. With the aid of this program, we can systematically evaluate how the mean depth changes as a function of the energy of slow positrons. In the Fig **4.11.1** it's showing the mean depth as a function of

positron energy using this MATLAB application. The link between positron energy and its related mean depth is clearly illustrated in this graph.

Calculation code of positron mean depth

```
E=[0.2:0.2:23] A=input('A') n=input('n') d=input('d') y=0.01*(A/d)*E.^n z = y
```

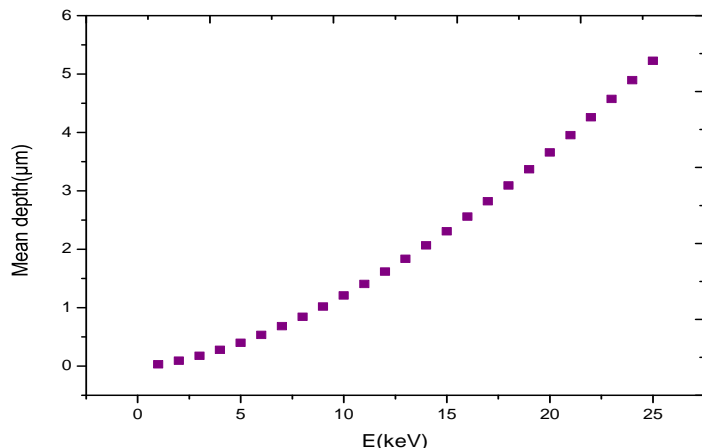


Figure 4.11.1: The variation of the mean depth of slow positrons as a function of their energy

4.11.2 VEDBS set-up :

In order to have an experience with the positron beam, we begin by launching the main, secondary, and pushed vacuum until we attain a normal vacuum of 10^{-9} mbar. Once the system has reached its empty vacuum, the following step is to activate the cryogenic system in the enclosure housing the RGM-1 radioactive source until a temperature of $6^{\circ}K$ is reached (this operation takes 24 hours to reach and stabilize this temperature). When the RGM-1 reaches a temperature of $6^{\circ}K$, we begin by infusing neon gas (purity 99.999%) at a very slow flow rate of 2 *SCCM* to promote healthy neon crystal formation. After the moderator has grown, we turn on the Helmholtz coils at the reaction chamber as well as the guidance system (solenoid) along the tube between RGM-1 and TS-1. An HV module linked to the accelerator is used to apply the negative high voltage. We used an HPGE detector of the Canberra type paired with an ORTEC 672 amplifier and a Maestro acquisition board to detect the positron spectrum.

A Beam calibration is required prior to doing a VEDBS experience and entails gathering Doppler enlargement spectra for various acceleration energies ranging from $0.1keV$ to $25keV$. The SP8 program was used to analyze the spectra. The S and W parameters may now be

calculated thanks to this. For the sample of Silicon, it is well known that the parameter S is 0.5 for energies beyond 10keV . Figure 4.11.2 shows the evolution of parameter S as a function of the incident energy of the positron beam.

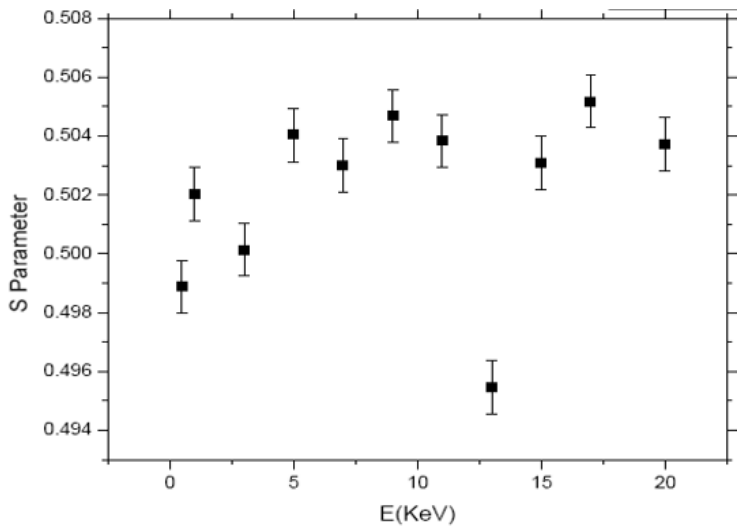


Figure 4.11.2: S variation of VEDBS(Si) spectra Vs positron beam energies

It is obvious that the parameter is rising in a monotone as the positron's energy rises. This outcome is predicted because the positron will quickly become trapped when it penetrates deeper due to the valence electrons' high electrical density. We are scanning the bulk because the parameter S is nearly constant starting at 10keV . As a result, the calibration is excellent for all energies, and the system is prepared for experiments on other material.

4.11.3 Measurements and discussion

After the system had been calibrated, CR39 samples, designated as $CR39(\neq E^*)$, were sequentially introduced into the source chamber (TS1). We next subjected these samples to a range of voltages ($0.5 - 0.8 - 1 - 3 - 5 - 7 - 9 - 11 - 13 - 15 - 17 - 20 - 23\text{V}$). Using the Maestro CARD MCA, we captured and preserved the energy spectrum for each applied voltage. We used a gain conversion factor of 16,000. The count rate were about 1000 counts per second, which is crucial to notice. This made it possible for us to collect the data precisely. With the obtained spectra at hand, we concentrated our investigation on determining the S parameter. The SP16 program was utilized to calculate the S parameter. We have depicted the variation of the S parameter with respect to positron beam energy for several CR39 samples in Fig. 4.11.3. This graphical representation gives a clear picture of how the S parameter changes as a function of energy and provides important information about how the CR39 samples behave.

Spectra analysis

VEDBS spectra were analyzed using the SP16 version, which allows for the collection of 16,000 channels. The fitted value of S_{bulk} for the unirradiated sample was found to be 0.4748, which was used as CR39's reference. We are plotting the S _ values against positron _ beam _ energies for each samples as it is mentionned in the Fig"4.11.3". When the S plots from different samples were compared, we mark that the S plots remained rather constant. Notably, the average value of the S parameter are consistently lower than the reference bulk value. The only instance where this trend deviates from the average is for the samples irradiated with the energy of 4.11MeV. It is clear that the damages caused by alpha particles in CR39 samples cannot be clearly monitored using VEDBS. Upon reflection, the two probable causes of this insensitivity are identified. First, the 500 μm thickness of the CR39 samples might have made more difficult for slow positron beam to sufficiently probe the hole electronic density. Second, it is thought that the applied fluence of alpha particles less than $10^7 \text{ alpha}/\text{cm}^2$ is insufficient for significant observations. Even when DBS is used to characterize this series, no appreciable differences are found. The lack of significant variations in the DBS characterisation emphasizes even more how difficult it is to find and keep track of structural changes brought on by alpha particles in that samples.

Taking these factors into account, it has been decided to repeat the experiment with a higher acquired fluence ($> 10^8$) in order to obtain more reliable and insightful findings.

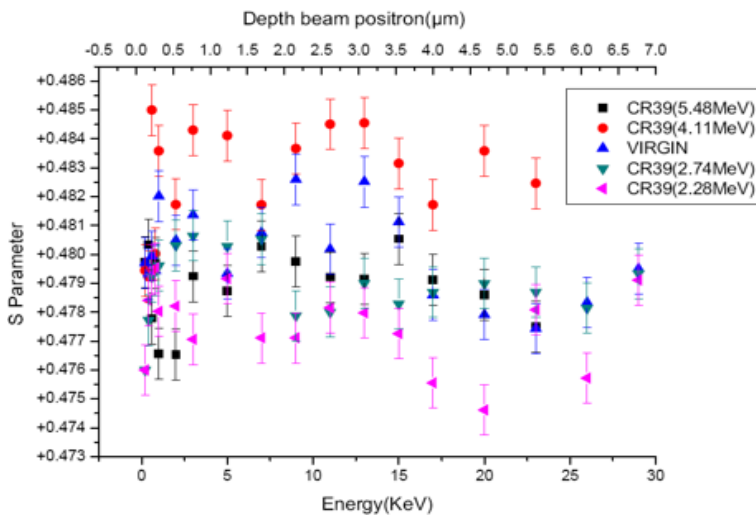


Figure 4.11.3: S variation of VEDBS (CR39) spectra Vs positron beam energies

4.12 Positron Lifetime calculation using DFT

In the context of this investigation, which is explained in *Chapter* 1, work is currently being done to develop a script that runs on Python. This script is intended to make the DFT technique easier to use when calculating the lifetime of annihilated ortho-Positronium ($o - Ps$). The fact that these simulations are done especially for un-irradiated CR39 is significant. Following Schmitz et al.'s model [66], a Buckingham potential has been used, as was previously indicated. Based on their model, which is represented by

equation "1.2.34", the potential that the positron of $o - Ps$ experiences inside the monomer of CR39 ($C_{12}H_{18}O_7$), which is referred to as $V_{pos-CR39}$, is developed as like shown in equ "4.12.1".

$$V_{pos-CR39}(r) = V_{\Sigma H}(r) + V_{\Sigma C}(r) + V_{\Sigma O}(r) \quad (4.12.1)$$

Where :

$$V_{\Sigma H}(r) = 18 \times (9800 \times \exp(-r/0.35) - 19.87/r^6) \quad (4.12.2)$$

$$V_{\Sigma C}(r) = 12 \times (41500 \times \exp(-r/0.15) - 16.1/r^6) \quad (4.12.3)$$

$$V_{\Sigma O}(r) = 7 \times (326739 \times \exp(-r/1.6) - 15/r^6) \quad (4.12.4)$$

We are using a computer methodology in which the process is started by solving a single-particle Schrödinger equation for the superposition potential. The positronic density is then obtained by effectively implementing a real-space DFT loop. By utilizing the computing power of Python packages like "eig" and "sparse," it is possible to diagonalize significant matrices from basic principles in an efficient manner. Because the DFT-based procedure is iterative, the density of $o - Ps$ may be determined by making repeated iterations, demonstrating the solid computational methodology used in the study. For the purpose of determining the lifetime of $o - Ps$, the electronic density must be derived. The functional form of the density, which is given by the density as the sum of densities from individual atoms expressed as mentioned

here.

$$\rho_{el}(r) = \sum_{atoms} N_i \exp(-|r - R_i|/a_i) \quad (4.12.5)$$

A well-defined formula expressed by the , equ^{4.12.5} is used to formulate the electronic density around a CR39 monomer, offering a methodical way to verify the *o-Ps* lifetime. For a monomer of CR39 ($C_{12}H_{18}O_7$) , the formula^{4.12.5} could be re-written like follows :

$$\rho_{el}(r') = \rho_{\Sigma H}(r') + \rho_{\Sigma C}(r') + \rho_{\Sigma O}(r') \quad (4.12.6)$$

Where :

$$\rho_{\Sigma H}(r') = 18(0.03 \exp(-r'/1.05)) \quad (4.12.7)$$

and

$$\rho_{\Sigma C}(r') = 12(0.5 \exp(-r'/0.52)) \quad (4.12.8)$$

,

$$\rho_{\Sigma O}(r') = 7(0.51 \exp(-r'/0.72)) \quad (4.12.9)$$

We use the formula^{1.2.37} in the last step of our study to calculate the *o-Ps* lifetime in unirradiated CR39. This formula captures the essential parameters controlling the positron annihilation process and makes it possible to determine the *o-Ps* lifetime. We obtain a *o-Ps* lifetime value of 1.71 nanoseconds by using this equation. The found provides a quantitative measure of the time taken for *o-Ps* to undergo annihilation in un-irradiated CR39, and represents the greatest achievement of our computational and theoretical efforts.

Conclusion

The main conclusions drawn from the thesis are covered in detail in this chapter. Important findings are the enhancement of time resolution in fast-fast type Positron Annihilation Lifetime Spectroscopy experiments and the optimization of both DBS and VEDBS configurations. The 50 counts per second (cps) count rate and the incredible time resolution of 0.270 picoseconds are the most noteworthy achievements in our PALS experiments. Tests that enabled the 511 KeV peak in silicon to be calibrated until the S parameter was equal to 0.5 demonstrated a noteworthy outcome within the DBS system. This result emphasizes the DBS system's accuracy and calibration, which increases its usefulness for spectroscopic research.

Once the experimental sets were optimized, we investigated the latent tracks that were created on CR39 as a result of alpha particle irradiation. Our main goal was to identify variations in the material's free volumes. Three separate series of samples, each exposed to radiation at a different fluence (and/or energy), were used in this investigation. PALS and DBS methods were used to do a thorough characterization of the first two series, designated as $CR39(\neq E)$ and $CR39(\neq \Phi)$. The series of $CR39(\neq E^*)$ have been characterized by VEDBS. Furthermore, a particular pre-processing step was performed on the $CR39(\neq \Phi)$ series. Following radiation, this series underwent a five-minute etching procedure. We then used PALS and DBS to perform additional analysis in order to obtain more understanding. The primary characterization method for the $CR39(\neq E)$ series is DBS, which yields useful characteristics information for the polymer. However, PALS does not show as much success in gathering appropriate information for this specific series. The characterization of the $CR39(\neq \Phi)$ series, on the other hand, is more rigorous. The growth of free volumes within the polymer can be effectively observed using both the DBS and PALS approaches. This combined approach enhances the understanding of structural changes induced during the irradiation process. The birth tracks that emerged five minutes after etching were subjected to a second analysis using PALS and DBS. The values of PAS, LT of o-Ps, free volume radius, and S-parameter have all demonstrated a distinct difference. Crucially, the study emphasizes the significant advantages of PAS over optical microscopy when examining birth tracks. PAS exhibits exceptional sensitivity, exposing details that are missed by conventional optical techniques, highlighting PAS's special ability to detect microscopic changes in structure in CR39.

To verify the results obtained from PALS, theoretical computations of the radial dosage distribution were carried out in conjunction with experimental studies. As part of the validation process, the calculated free volumes fraction, F'_V , using the Waligorski Calculation, was carefully compared to the experimentally determined free volumes fraction F_V from PALS. One of the most important steps in verifying the precision and dependability of the PALS results was this comparative analysis. The investigation also included theoretical calculations using Density Functional Theory (DFT) of the $o - Ps$ lifetime. This computational component added even more value to the study, offering a thorough comprehension that combines theoretical and experimental knowledge about the complex behavior of positrons in the CR39 polymer.

Our future research trajectory will be shaped by the interesting results of our current inves-

tigation, which will clearly emphasize examining the lifetime of $o - Ps$ in irradiated samples. The difficulties in understanding the positron potential in this project provide an interesting component, making this field worthy of more investigation and study. Future research projects that are being suggested will investigate the intricacies of positron behavior in irradiated samples in greater detail in an effort to gain new knowledge and improve our comprehension of this complex phenomenon.

General Conclusion

The techniques of Positron Annihilation Spectroscopy (PAS) have become a standard tool for the characterization of polymers. This developing journey highlights the tremendous adaptability shown in scientific investigation, beginning with early theoretical predictions and discoveries and continuing with continued technique improvements.

The goals of this thesis project can be divided into two main sections: The main objective is to set up two separate spectroscopic chains: Doppler Broadening Spectroscopy (DBS) and Positron Annihilation Lifetime Spectroscopy (PALS), and at the same time, become able in Variational Energy Doppler Broadening Spectroscopy (VEDBS). The secondary goal is to investigate the effects of alpha irradiation on CR39 polymers. This complementary-spectroscopy methods of PAS aims to reveal the complex structural alterations caused by alpha particles via combining the use of PALS and DBS techniques. By doing this, it hopes to offer a thorough grasp of the chemical mechanisms underlying the CR39's response to radiation.

The work's dramatic theme revolves around the search for optimum circumstances for the best resolution required for characterizing polymers. Time resolution as well as the PALS counts rate. Assessing the optimal temporal resolution is the true success of carrying out such a setup about the PALS technique. The temporal resolution and counts rate were the main factors used in each experiment to evaluate the spectrometer's quality. The best temporal resolution of 0.270 ps at a count rate of 50 cps was attained. Adding to that, experiments showing that the 511KeV pic in silicon could be calibrated up to 0.5, S parameter have been realized for the DBS setup. Furthermore, a thorough explanation and demonstration of the VEDBS system setup have been provided.

CR39 is an amorphous polymer designated as a solid-state nuclear track detector (SSNTD). It serves a vital role in trap and hold charged particles, which emphasizes its remarkable capacity in alpha particles detection. In the second section of the thesis, latent tracks from alpha particle

irradiation of CR39 were carefully investigated. In that phase, an array of extensive experiments were conducted. The study employed PALS, DBS, and VEDBS, each contributing a distinct viewpoint.

PALS proved to be a successful tool during the entirety of the investigation. It proved to be able to accurately capture variations in the angstrom size of latent tracks brought on by alpha radiation. The high sensitivity of PALS demonstrated its uniqueness as a characterization technique of radiation damage. By including the DBS approach into the experimental series, it is possible that significant insights into the features of irradiation effects were gained, leading to a more thorough comprehension of the free volumes variation on CR39. VEDBS was inaccurate in our case of study for the reason of fluence or samples thickness.

The main objective of the study was to clarify CR39's complex reaction to alpha particle irradiation. Using a variety of these PAS methods, the research sought to offer a comprehensive and multidimensional picture of the structural changes that alpha particles cause in CR39.

The detailed analysis's conclusion yields the following significant conclusions:

- The behavior of the free volume radius for the series of $CR39(\neq \Phi)$ closely matches the S-parameter acquired via DBS. Strong correlations like this one demonstrate how well the two methods complement one another and improve our understanding of structural changes as a whole.
- There is a good agreement between theoretical calculations and PALS data for the fraction of free volume concentration, as predicted by the Waligorski model. This alignment is most noticeable in the $CR39(\neq \Phi)$ series, where the alpha particle fluence is greater than 10^8 , confirming the validity of both theoretical and experimental methods.
- PALS shows to be a flexible instrument, capable of recording angstrom size changes related to birth tracks following the etching process in addition to evaluating the total free volume concentration. This adaptability emphasizes how PALS can be used as a reliable technique to describe the evolution of birth tracks.
- Despite unconvincing results from VEDBS for the series $CR39(\neq E^*)$, due to sample thickness or insufficient alpha particle fluences, the DFT-based modeling for $o - Ps$ lifetime computation emerges as a promising and dependable technique for future investigations, the o-Ps behavior in the CR39 polymer is complicated, and this modeling approach pro-

vides a solid foundation for understanding it.

These strong results provide the groundwork for further investigations, one of which will be to investigate the lifetime of $o - Ps$ in irradiated polymers. The difficulties in comprehending positron potential that have arisen during this endeavor highlight how fascinating this field is and how much more research and investigation it deserves.

The study then emphasizes how important PALS is for describing how alpha radiation affects CR39. It is a unique and effective technique for assessing radiation damage because of its capacity to precisely quantify changes in the size of latent tracks at the angstrom level. The enhanced sensitivity of PALS is especially noticeable when it comes to identifying and evaluating different kinds of alterations brought about by alpha particles, which makes a major contribution to the overall comprehension of CR39's responses to radiation.

Bibliography

- [1] Carl D Anderson. The apparent existence of easily deflectable positives. *Science*, 76(1967):238–239, 1932.
- [2] J. Gebauer, S. Eichler, R. Krause-Rehberg, and H.P. Zeindl. Experiments to determine the mean depth scale of positrons in silicon: slow positron beam measurements on MBE-grown silicon layers on silicon oxide. *Applied Surface Science*, 116:247–250, may 1997.
- [3] T. Saitoh and Y. Kawada. Emission probability of the weak positron branch in the decay of ^{22}Na to the ground state of ^{22}Ne . *Nuclear Instruments and Methods in Physics Research Section A: Accelerators, Spectrometers, Detectors and Associated Equipment*, 369(2-3):503–505, feb 1996.
- [4] Glenn F Knoll. *Radiation Detection and Measurement 4th Edition*. 8/2010.
- [5] A. P. Mills and E. M. Gullikson. Solid neon moderator for producing slow positrons. *Applied Physics Letters*, 49(17):1121–1123, 1986.
- [6] RK Bull and SA Durrani. Solid state nuclear track detectors, principles, method and applications, 1987.
- [7] Price P.B. Walker R.M Fleischer, R.L. *Nuclear Tracks in Solids: Principles and Applications*. University of California Press, Berkeley., 1975.
- [8] David Roilo. *Gas transport properties and free volume structure of polymer nanocomposite membranes*. PhD thesis, UNIVERSITY OF TRENTO Department of Physics, 2016-2017.
- [9] Y. C. Jean, J. David Van Horn, Wei-Song Hung, and Kuier-Rarn Lee. Perspective of positron annihilation spectroscopy in polymers. *Macromolecules*, 46(18):7133–7145, aug 2013.

- [10] Günter Dlubek, Hellen M. Fretwell, and Norbert Meyendorf. Positron annihilation: A new method for studying subnanometer-size local free volumes in polymers, apr 2000.
- [11] Yu K.N. . Nikezic, D. Formation and growth of tracks in nuclear track materials. *Mater. Sci. Eng. R Rep*, 46:51–123, 2004.
- [12] E. Schrödinger. An undulatory theory of the mechanics of atoms and molecules. *Phys. Rev.*, 28:1049–1070, Dec 1926.
- [13] P. A. M. Dirac. The fundamental equations of quantum mechanics. *Proceedings of the Royal Society of London A: Mathematical, Physical and Engineering Sciences*, 109(752):642–653, 1925.
- [14] P. A. M. Dirac. On the annihilation of electrons and protons. *Mathematical Proceedings of the Cambridge Philosophical Society*, 26(3):361–375, 1930.
- [15] P. A. M. Dirac. Note on exchange phenomena in the thomas atom. *Mathematical Proceedings of the Cambridge Philosophical Society*, 26(3):376–385, 1930.
- [16] Carl D. Anderson. The positive electron. *Phys. Rev.*, 43:491–494, Mar 1933.
- [17] Martin Deutsch. Evidence for the formation of positronium in gases. *Phys. Rev.*, 82:455–456, May 1951.
- [18] M. Charlton and J. W. Humberston. *Positron Physics*. Cambridge University Press, dec 2000.
- [19] Martin Deutsch. Three-quantum decay of positronium. *Phys. Rev.*, 83:866–867, Aug 1951.
- [20] Arthur Rich. Recent experimental advances in positronium research. *Rev. Mod. Phys.*, 53:127–165, Jan 1981.
- [21] Günter Dlubek, Duncan Kilburn, Vladimir Bondarenko, Jürgen Pionteck, Reinhard Krause-Rehberg, and M. Ashraf Alam. Positron annihilation: a unique method for studying polymers. *Macromolecular Symposia*, 210(1):11–20, 2004.
- [22] Ole E Mogensen. Positron annihilation in chemistry. 2012.

- [23] J. Nico, D. Gidley, A. Rich, and P. Zitzewitz. Precision measurement of the orthopositronium decay rate using the vacuum technique. *Physical Review Letters*, 65(11):1344–1347, sep 1990.
- [24] Alfredo Dupasquier and AP Mills Jr. *Positron spectroscopy of solids*, volume 125. IOS press, 1995.
- [25] S. DeBenedetti, C. E. Cowan, and W. R. Konneker. Angular distribution of annihilation radiation. *Phys. Rev.*, 76:440–440, Aug 1949.
- [26] J. W. M. Dumond, D. A. Lind, and B. B. Watson. Precision measurement of the wavelength and spectral profile of the annihilation radiation from Cu^{64} with the two-meter focusing curved crystal spectrometer. *Phys. Rev.*, 75:1226–1239, Apr 1949.
- [27] Pekka Hautojärvi, editor. *Positrons in Solids*. Springer Berlin Heidelberg, 1979.
- [28] P. E. Mallon & D. M. Schrader Y. C. Jean, editor. *Principles and Applications of POSITRON and POSITRONIUM CHEMISTRY*. World Scientific Publishing Co. Pte. Ltd. 5 Toh Tuck Link, Singapore 596224, 2003.
- [29] M. J. Puska and R. M. Nieminen. Theory of positrons in solids and on solid surfaces. *Reviews of Modern Physics*, 66(3):841–897, jul 1994.
- [30] M. J. Puska, C. Corbel, and R. M. Nieminen. Positron trapping in semiconductors. *Phys. Rev. B*, 41:9980–9993, May 1990.
- [31] J. P. Carbotte. Theory of positron annihilation in real metals. *Phys. Rev.*, 144:309–318, Apr 1966.
- [32] J. P. Carbotte and A. Salvadori. Positron annihilation in real metals. ii. calculation of core enhancement factors. *Phys. Rev.*, 162:290–300, Oct 1967.
- [33] A. Vehanen, K. Saarinen, P. Hautojärvi, and H. Huomo. Profiling multilayer structures with monoenergetic positrons. *Phys. Rev. B*, 35:4606–4610, Apr 1987.
- [34] Werner Brandt and Robert Paulin. Positron implantation-profile effects in solids. *Physical Review B*, 15(5):2511–2518, mar 1977.
- [35] M. Mourino, H. Löbl, and R. Paulin. Profiles and absorption coefficients of positrons implanted in solids from radioactive sources. *Physics Letters A*, 71(1):106–108, apr 1979.

- [36] Allen P. Mills and Robert J. Wilson. Transmission of 1 - 6-keV positrons through thin metal films. *Phys. Rev. A*, 26:490–500, Jul 1982.
- [37] S. Valkealahti and R. M. Nieminen. Monte-carlo calculations of keV electron and positron slowing down in solids. *Applied Physics A Solids and Surfaces*, 32(2):95–106, oct 1983.
- [38] Shi-Juan Huang, Zi-Wen Pan, Jian-Dang Liu, Rong-Dian Han, and Bang-Jiao Ye. Simulation of positron backscattering and implantation profiles using geant4 code. *Chinese Physics B*, 24(10):107803, sep 2015.
- [39] Vinita J. Ghosh and G. C. Aers. Positron stopping in elemental systems: Monte carlo calculations and scaling properties. *Physical Review B*, 51(1):45–59, jan 1995.
- [40] T.C. Leung, P.J. Simpson, A. Atkinson, I.V. Mitchell, and Peter J. Schultz. Measurement of oxide thickness using a variable-energy positron beam. *Applied Surface Science*, 85:292–294, jan 1995.
- [41] John Algers, Peter Sperr, Werner Egger, Gottfried Kögel, and Frans H. J. Maurer. Median implantation depth and implantation profile of 3–18 keV positrons in amorphous polymers. *Phys. Rev. B*, 67:125404, Mar 2003.
- [42] S. Eichler, C. Hübner, and R. Krause-Rehberg. A monte-carlo simulation of positron diffusion in solids. *Applied Surface Science*, 116:155–161, may 1997.
- [43] M. J. Puska, S. Mäkinen, M. Manninen, and R. M. Nieminen. Screening of positrons in semiconductors and insulators. *Physical Review B*, 39(11):7666–7679, apr 1989.
- [44] M Tuomisaari, R H Howell, and T McMullen. Positronium formation and diffusion in the rare-gas solids. *Journal of Physics B: Atomic, Molecular and Optical Physics*, 24(6):1455–1466, mar 1991.
- [45] E. Soininen, J. Mäkinen, D. Beyer, and P. Hautojärvi. High-temperature positron diffusion in si, GaAs, and ge. *Physical Review B*, 46(20):13104–13118, nov 1992.
- [46] Alfredo Dupasquier, Allen P Mills, and Roberto S Brusa. *Physics with Many Positrons: Proceedings of the International School of Physics " Enrico Fermi", Course CLXXIV, Varenna on Lake Como, Villa Monastero, 7-17 July 2009*, volume 174. IOS Press, 2010.

- [47] P G Coleman, L Albrecht, K O Jensen, and A B Walker. Positron backscattering from elemental solids. *Journal of Physics: Condensed Matter*, 4(50):10311–10322, dec 1992.
- [48] G. R. Massoumi, W. N. Lennard, Peter J. Schultz, A. B. Walker, and Kjeld O. Jensen. Experimental and monte-carlo studies of electron and positron backscattering. In *AIP Conference Proceedings*. AIP, 1994.
- [49] J Makinen, S Palko, J Martikainen, and P Hautajarvi. Positron backscattering probabilities from solid surfaces at 2-30 keV. *Journal of Physics: Condensed Matter*, 4(36):L503–L508, sep 1992.
- [50] M. M. Madani and R. D. Granata. Positron backscattering in polymer/metal systems. *Journal of Applied Physics*, 80(5):2555–2560, sep 1996.
- [51] S. Kahana. Positron annihilation in metals. *Physical Review*, 129(4):1622–1628, feb 1963.
- [52] S. Kahana. Positron annihilation in metals. *Physical Review*, 117(1):123–128, jan 1960.
- [53] P. Hohenberg and W. Kohn. Inhomogeneous electron gas. *Physical Review*, 136(3B):B864–B871, nov 1964.
- [54] W. Kohn and L. J. Sham. Self-consistent equations including exchange and correlation effects. *Physical Review*, 140(4A):A1133–A1138, nov 1965.
- [55] N. D. Drummond, P. López Ríos, R. J. Needs, and C. J. Pickard. Quantum monte carlo study of a positron in an electron gas. *Physical Review Letters*, 107(20):207402, nov 2011.
- [56] K. A. Simula, J.E. Muff, I. Makkonen, and N.D. Drummond. Quantum monte carlo study of positron lifetimes in solids. *Physical Review Letters*, 129(16):166403, oct 2022.
- [57] E. Boronski and R. M. Nieminen. Electron-positron density-functional theory. *Phys. Rev. B*, 34:3820–3831, Sep 1986.
- [58] J Arponen and E Pajanne. Electron liquid in collective description. III. positron annihilation. *Annals of Physics*, 121(1-2):343–389, sep 1979.
- [59] J Arponen and E Pajanne. Angular correlation in positron annihilation. *Journal of Physics F: Metal Physics*, 9(12):2359–2376, dec 1979.
- [60] Lauri J. Lantto. Variational theory of multicomponent quantum fluids: An application to positron-electron plasmas at $t=0/i$. *Physical Review B*, 36(10):5160–5170, oct 1987.

- [61] J M Campillo Robles, E Ogando, and F Plazaola. Positron lifetime calculation for the elements of the periodic table. *Journal of Physics: Condensed Matter*, 19(17):176222, apr 2007.
- [62] S. J. Tao. Positronium annihilation in molecular substances. *Chemical Physics*, 56(11):5499, jun 1972.
- [63] M. Eldrup, D. Lightbody, and J.N. Sherwood. The temperature dependence of positron lifetimes in solid pivalic acid. *Chemical Physics*, 63(1):51 – 58, 1981.
- [64] A Zubiaga, M M Ervasti, I Makkonen, A Harju, F Tuomisto, and M J Puska. Modeling positronium beyond the single particle approximation. *Journal of Physics B: Atomic, Molecular and Optical Physics*, 49(6):064005, mar 2016.
- [65] LO Roellig. Positron annihilation in liquids and condensed gases. In *Positron Annihilation*, pages 127–141. Elsevier, 1967.
- [66] Heiko Schmitz and Florian Müller-Plathe. Calculation of the lifetime of positronium in polymers via molecular dynamics simulations. *The Journal of Chemical Physics*, 112(2):1040–1045, jan 2000.
- [67] Julia Wiktor, Gérald Jomard, and Marc Torrent. Two-component density functional theory within the projector augmented-wave approach: Accurate and self-consistent computations of positron lifetimes and momentum distributions. *Physical Review B*, 92(12):125113, sep 2015.
- [68] I. Makkonen, M. Hakala, and M. J. Puska. Modeling the momentum distributions of annihilating electron-positron pairs in solids. *Physical Review B*, 73(3):035103, jan 2006.
- [69] Christian Rauch, Ilja Makkonen, and Filip Tuomisto. Identifying vacancy complexes in compound semiconductors with positron annihilation spectroscopy: A case study of InN. *Physical Review B*, 84(12):125201, sep 2011.
- [70] S Daniuk, G Kontrym-Sznajd, A Rubaszek, H Stachowiak, J Mayers, P A Walters, and R N West. Selective enhancement of different electron populations by electron-positron attraction: application to zinc. *Journal of Physics F: Metal Physics*, 17(6):1365–1378, jun 1987.

- [71] A. Zubiaga, F. Tuomisto, and M. J. Puska. Matter-positronium interaction: A study of the he-atom-positronium system. *Physical Review A*, 85(5):052707, may 2012.
- [72] Wenshuai Zhang, Jiandang Liu, Jie Zhang, Shijuan Huang, Jun Li, and Bangjiao Ye. Assessment of several calculation methods for positron lifetime. In *JJAP Conference Proceedings 2nd Japan-China Joint Workshop on Positron Science (JWPS2013)*, pages 011001–011001. The Japan Society of Applied Physics, 2014.
- [73] Qimen Xu, Abhiraj Sharma, and Phanish Suryanarayana. M-SPARC: Matlab-simulation package for ab-initio real-space calculations. *SoftwareX*, 11:100423, jan 2020.
- [74] R. Krause-Rehberg, N. van der Walt, L. Büttner, and F. Börner. A ^{22}Na positron source for use in UHV. *Nuclear Instruments and Methods in Physics Research Section B: Beam Interactions with Materials and Atoms*, 221:165–167, jul 2004.
- [75] D. W. Gidley, A. Rich, P. W. Zitzewitz, and D. A. L. Paul. New experimental value for the orthopositronium decay rate. *Physical Review Letters*, 40(12):737–740, mar 1978.
- [76] Rong Xie. *Positron reemission microscopy with high flux positron beams*. Brandeis University, 1997.
- [77] PG Coleman. The generation and transport of positron beams. In *Positron beams and their applications*, pages 11–40. World Scientific, 2000.
- [78] H.M. Weng, Y.F. Hu, C.D. Beling, and S. Fung. An apparatus used to make ^{22}Na sources for use in low-energy positron beams. *Applied Surface Science*, 116:98–103, may 1997.
- [79] D.T. Britton, M. Härting, M.R.B. Teemane, S. Mills, F.M. Nortier, and T.N. Van der Walt. A southern african positron beam. *Applied Surface Science*, 116:53–58, may 1997.
- [80] William H Cherry. *Secondary electron emission produced from surfaces by positron bombardment*. Princeton University, 1958.
- [81] D. G. Costello, D. E. Groce, D. F. Herring, and J. Wm. McGowan. Evidence for the negative work function associated with positrons in gold. *Phys. Rev. B*, 5:1433–1436, Feb 1972.
- [82] KF Canter, GR Brandes, TN Horsky, PH Lippel, and AP Mills Jr. Atomic physics with positrons. *Humberston JW and Armour EAG, eds*, 1987.

- [83] R. E. Bell and R. L. Graham. Time distribution of positron annihilation in liquids and solids. *Physical Review*, 90(4):644–654, may 1953.
- [84] Stephan Berko and A. Joseph Zuchelli. Free-radical quenching of positron lifetimes. *Physical Review*, 102(3):724–728, may 1956.
- [85] Roger B. Gregory and Yongkang Zhu. Analysis of positron annihilation lifetime data by numerical laplace inversion with the program CONTIN. *Nuclear Instruments and Methods in Physics Research Section A: Accelerators, Spectrometers, Detectors and Associated Equipment*, 290(1):172–182, may 1990.
- [86] A. Shukla, M. Peter, and L. Hoffmann. Analysis of positron lifetime spectra using quantified maximum entropy and a general linear filter. *Nuclear Instruments and Methods in Physics Research Section A: Accelerators, Spectrometers, Detectors and Associated Equipment*, 335(1-2):310–317, oct 1993.
- [87] Peter Kirkegaard and Morten Eldrup. Positronfit: A versatile program for analysing positron lifetime spectra. Technical report, Danish Atomic Energy Commission Research Establishment, Risoe, 1972.
- [88] Peter Kirkegaard, Morten Eldrup, Ole E Mogensen, and Niels J Pedersen. Program system for analysing positron lifetime spectra and angular correlation curves. *Computer Physics Communications*, 23(3):307–335, 1981.
- [89] J. V. Olsen, P. Kirkegaard, N. J. Pedersen, and M. Eldrup. PALSfit: A new program for the evaluation of positron lifetime spectra. *physica status solidi c*, 4(10):4004–4006, sep 2007.
- [90] Carlos Pascual-Izarra, Aurelia W. Dong, Steven J. Pas, Anita J. Hill, Ben J. Boyd, and Calum J. Drummond. Advanced fitting algorithms for analysing positron annihilation lifetime spectra. *Nuclear Instruments and Methods in Physics Research Section A: Accelerators, Spectrometers, Detectors and Associated Equipment*, 603(3):456–466, may 2009.
- [91] Roel Snieder. The role of nonlinearity in inverse problems. *Inverse Problems*, 14(3):387–404, jun 1998.

- [92] António R. C. Paiva, Jian-Wu Xu, and José C. Príncipe. Kernel principal components are maximum entropy projections. In *Independent Component Analysis and Blind Signal Separation*, pages 846–853. Springer Berlin Heidelberg, 2006.
- [93] J Kansy. Microcomputer program for analysis of positron annihilation lifetime spectra. *Nuclear Instruments and Methods in Physics Research Section A: Accelerators, Spectrometers, Detectors and Associated Equipment*, 374(2):235 – 244, 1996.
- [94] Danny Petschke and Torsten E.M. Staab. A supervised machine learning approach using naive gaussian bayes classification for shape-sensitive detector pulse discrimination in positron annihilation lifetime spectroscopy (PALS). *Nuclear Instruments and Methods in Physics Research Section A: Accelerators, Spectrometers, Detectors and Associated Equipment*, 947:162742, dec 2019.
- [95] H. P. Hotz, J. M. Mathiesen, and J. P. Hurley. Measurement of positron annihilation line shapes with a ge(li) detector. *Phys. Rev.*, 170:351–355, Jun 1968.
- [96] I.K. MacKenzie, J.A. Eady, and R.R. Gingerich. The interaction between positrons and dislocations in copper and in an aluminum alloy. *Physics Letters A*, 33(5):279 – 280, 1970.
- [97] Jerzy Dryzek. Influence of the positron implantation profile on the study of the defect depth distribution by the positron annihilation technique. *Journal of Applied Physics*, 133(5):055104, feb 2023.
- [98] Leon Madansky and Franco Rasetti. An attempt to detect thermal energy positrons. *Phys. Rev.*, 79:397–397, Jul 1950.
- [99] Allen P. Mills. Observation of the positronium negative ion. *Phys. Rev. Lett.*, 46:717–720, Mar 1981.
- [100] Peter J. Schultz and K. G. Lynn. Interaction of positron beams with surfaces, thin films, and interfaces. *Rev. Mod. Phys.*, 60:701–779, Jul 1988.
- [101] B. Y. Tong. Negative work function of thermal positrons in metals. *Phys. Rev. B*, 5:1436–1439, Feb 1972.
- [102] C. H. Hodges and M. J. Stott. Work functions for positrons in metals. *Phys. Rev. B*, 7:73–79, Jan 1973.

- [103] Howard Weisberg and Stephan Berko. Positron lifetimes in metals. *Physical Review*, 154(2):249–257, feb 1967.
- [104] Filip Tuomisto and Ilja Makkonen. Defect identification in semiconductors with positron annihilation: Experiment and theory. *Reviews of Modern Physics*, 85(4):1583–1631, nov 2013.
- [105] P. Horodek, J. Dryzek, and V.A. Skuratov. Positron annihilation study of defects in copper irradiated with swift xe 26 ions. *Vacuum*, 138:15–21, apr 2017.
- [106] R.M. Walker R.L. Fleischer, P.B. Price. *Nuclear Tracks in Solids*. University of California Press, 1975.
- [107] R L Fleischer, P B Price, and R M Walker. Solid-state track detectors: Applications to nuclear science and geophysics. *Annual Review of Nuclear Science*, 15(1):1–28, 1965.
- [108] B.G. Cartwright, E.K. Shirk, and P.B. Price. A nuclear-track-recording polymer of unique sensitivity and resolution. *Nuclear Instruments and Methods*, 153(2):457 – 460, 1978.
- [109] R.M. Cassou and E.V. Benton. Properties and applications of cr-39 polymeric nuclear track detector. *Nuclear Track Detection*, 2(3):173 – 179, 1978.
- [110] H. B. Schlegel G. E. Scuseria M. A. Robb J. R. Cheeseman G. Scalmani V. Barone B. Mennucci G. A. Petersson H. Nakatsuji M. Caricato X. Li H. P. Hratchian A. F. Izmaylov J. Bloino G. Zheng J. L. Sonnenberg M. Hada M. Ehara K. Toyota R. Fukuda J. Hasegawa M. Ishida T. Nakajima Y. Honda O. Kitao H. Nakai T. Vreven J. A. Montgomery Jr. J. E. Peralta F. Ogliaro M. Bearpark J. J. Heyd E. Brothers K. N. Kudin V. N. Staroverov R. Kobayashi J. Normand K. Raghavachari A. Rendell J. C. Burant S. S. Iyengar J. Tomasi M. Cossi N. Rega J. M. Millam M. Klene J. E. Knox J. B. Cross V. Bakken C. Adamo J. Jaramillo R. Gomperts R. E. Stratmann O. Yazyev A. J. Austin R. Cammi C. Pomelli J. W. Ochterski R. L. Martin K. Morokuma V. G. Zakrzewski G. A. Voth P. Salvador J. J. Dannenberg S. Dapprich A. D. Daniels O. Farkas J. B. Foresman J. V. Ortiz J. Cioslowski M. J. Frisch, G. W. Trucks and Inc. Wallingford CT D. J. Fox, Gaussian. Gaussian 09, revision a.02. 2009.

- [111] Nabila Aissiou, Moussa Bounoughaz, and Amel Djeddi. Lignin-phenylhydrazone as a corrosion inhibitor of API x52 carbon steel in 3.5% NaCl and 0.1 mol/l HCl medium. *Chemical Research in Chinese Universities*, 37(3):718–728, mar 2021.
- [112] Michel Fromm, Satoshi Kodaira, Tamon Kusumoto, Rémi Barillon, and Tomoya Yamauchi. Role of intermediate species in the formation of ion tracks in padc: A review. *Polymer Degradation and Stability*, 161:213 – 224, 2019.
- [113] Rajesh Kumar, Santa Rajguru, D. Das, and Rajendra Prasad. Shi induced modification in cr-39 polycarbonate by positron annihilation lifetime studies. *Radiation Measurements*, 36(1):151 – 154, 2003. Proceedings of the 21st International Conference on Nuclear Tracks in Solids.
- [114] ABDESLAM SEGHOOR. *Dosimetrie et spectrometrie des neutrons. Recherche des conditions optimales pour le dosage du bore et application a la boroneutrotherapie*. PhD thesis, 1993. Thèse de doctorat dirigée par Sens, Jean-Claude Physique. Sciences médicales Université Louis Pasteur (Strasbourg) (1971-2008) 1993.
- [115] J. J. Butts and Robert Katz. Theory of rbe for heavy ion bombardment of dry enzymes and viruses. *Radiation Research*, 30(4):855–871, 1967.
- [116] Robert Katz and E. J. Kobetich. Particle tracks in emulsion. *Physical Review*, 186(2):344–351, oct 1969.
- [117] R. Katz and E. J. Kobetich. Formation of particle tracks. *Radiation Effects*, 3(2):169–174, jan 1970.
- [118] Robert Katz. Track structure theory in radiobiology and in radiation detection. *Nuclear Track Detection*, 2(1):1–28, mar 1978.
- [119] Hermann Dertinger and Horst Jung. The action of radiation on enzymes: The example of ribonuclease. In *Molecular Radiation Biology*, pages 115–133. Springer US, 1970.
- [120] Gunter G. Weber. Delta-function model for interaction of two-electron atoms and ions. *The Journal of Chemical Physics*, 40(6):1762–1768, mar 1964.
- [121] J. Fain, M. Monnin, M. Montret, and J. Fain. Spatial energy distribution around heavy-ion path. *Radiation Research*, 57(3):379, mar 1974.

- [122] Lounis Épse. Mokrani Zohra. *Contribution À L'étude Du Mécanisme De Formation Des Traces Nucléaires Dans Un Détecteur Solide De Type Organique (cr-39) Application À La Spectrométrie Et À La Dosimétrie Des Rayonnements*. PhD thesis, USTHB, Alger, 2006.
- [123] M.P.R. Waligórski, R.N. Hamm, and R. Katz. The radial distribution of dose around the path of a heavy ion in liquid water. *International Journal of Radiation Applications and Instrumentation. Part D. Nuclear Tracks and Radiation Measurements*, 11(6):309 – 319, 1986.
- [124] R. Katz and F.A. Cucinotta. Tracks to therapy. *Radiation Measurements*, 31(1-6):379–388, jun 1999.
- [125] J Kiefer and H Straaten. A model of ion track structure based on classical collision dynamics (radiobiology application). *Physics in Medicine and Biology*, 31(11):1201–1209, nov 1986.
- [126] Francis A Cucinotta, Robert Katz, John W Wilson, and Rajendra R Dubey. Heavy ion track-structure calculations for radial dose in arbitrary materials. Technical report, 1995.
- [127] F. A. Cucinotta, Hooshang Nikjoo, and Dudley T. Goodhead. Applications of amorphous track models in radiation biology. *Radiation and Environmental Biophysics*, 38(2):81–92, jul 1999.
- [128] J. Chen and A.M. Kellerer. Calculation of radial dose distributions for heavy ions by a new analytical approach. *Radiation Protection Dosimetry*, 70(1):55–58, apr 1997.
- [129] E.M. Awad, I. El Masady, Y.S. Rammah, and M. Abu-Shady. Simulating the radial dose distribution for charged particles in water medium by a semi-empirical model: An analytical approach. *Applied Radiation and Isotopes*, 142:135–142, dec 2018.
- [130] T. Tabata, R. Ito, and S. Okabe. Generalized semiempirical equations for the extrapolated range of electrons. *Nuclear Instruments and Methods*, 103(1):85–91, aug 1972.
- [131] Reimar Spohr. *Ion tracks and microtechnology: principles and applications*. Reimar Spohr, 1990.

- [132] Z. Lounis-Mokrani, A. Badreddine, D. Mebhah, D. Imatoukene, M. Fromm, and M. Allab. Determination of the proton latent track dimensions in CR-39 detectors using small angle neutron scattering. *Radiation Measurements*, 43:S41–S47, aug 2008.
- [133] Shi-Lun Guo, Bao-Liu Chen, and S.A. Durrani. Solid-state nuclear track detectors. In *Handbook of Radioactivity Analysis*, pages 307–407. Elsevier, 2020.
- [134] Jian Wang, Yahong Zhou, and Lei Jiang. Bio-inspired track-etched polymeric nanochannels: Steady-state biosensors for detection of analytes. *ACS Nano*, 15(12):18974–19013, nov 2021.
- [135] E. Dartyge, J. P. Duraud, Y. Langevin, and M. Maurette. New model of nuclear particle tracks in dielectric minerals. *Physical Review B*, 23(10):5213–5229, may 1981.
- [136] Xing-Fen Jiang, Jian-Rong Zhou, Hong Luo, Liang Xiao, Xiao-Juan Zhou, Hong Xu, Yuan-Guang Xia, Xiao-Guang Wu, Lin Zhu, Wen-Qing Yang, Gui-An Yang, Bei-Ju Guan, Hong-Yu Zhang, Yu-Bin Zhao, Zhi-Jia Sun, and Yuan-Bo Chen. A large area ^3He tube array detector with vacuum operation capacity for the SANS instrument at the CSNS. *Nuclear Science and Techniques*, 33(7), jul 2022.
- [137] T. Yamauchi, N. Yasuda, T. Asuka, K. Izumi, T. Masutani, K. Oda, and R. Barillon. Track core size estimation for heavy ions in CR-39 by AFM and UV methods. *Nuclear Instruments and Methods in Physics Research Section B: Beam Interactions with Materials and Atoms*, 236(1-4):318–322, jul 2005.
- [138] A.F. Saad, E.M. Sedqy, and R.M. Ahmed. Effect of UVC radiation on the optical properties of thermally treated CR-39 polymer films: A new approach for the use of CR-39 as an optical dosimeter. *Radiation Physics and Chemistry*, 179:109253, feb 2021.
- [139] T. Yamauchi, R. Barillon, E. Balanzat, T. Asuka, K. Izumi, T. Masutani, and K. Oda. Yields of formation and scissions at ether bonds along nuclear tracks in CR-39. *Radiation Measurements*, 40(2-6):224–228, nov 2005.
- [140] T. Yamauchi, S. Watanabe, A. Seto, K. Oda, N. Yasuda, and R. Barillon. Loss of carbonate ester bonds along Fe^{2+} ion tracks in thin CR-39 films. *Radiation Measurements*, 43:S106–S110, aug 2008.

- [141] M. Fromm. Light mev-ions etching studies in a plastic track detector. *Radiation Measurements*, 40(2):160 – 169, 2005. Proceedings of the 22nd International Conference on Nuclear Tracks in Solids.
- [142] G. Immè, D. Morelli, M. Aranzulla, R. Catalano, and G. Mangano. Nuclear track detector characterization for alpha-particle spectroscopy. *Radiation Measurements*, 50:253–257, mar 2013.
- [143] Aqmur Alassi and Ahmed Alobaidy. The impact of the normality of two types of chemical solutions on the etching rates of nuclear track detector CR-39. *Kirkuk University Journal-Scientific Studies*, 0(0):0–0, may 2023.
- [144] Mostafa Fawzy Eissa. Optical properties of cr-39 track etch detectors irradiated by alpha particles with different energies. *Journal of Materials Science and Engineering*, 5(1):26, 2011.
- [145] Emad N Saad, MF Eissa, Emad A Badawi, and MAK El-Fayoumi. Investigation of the physical properties of polymeric materials induced by alpha radiation. *Int. J. Advan. Res*, 12:694–702, 2014.
- [146] M F Zaki, Y H Elshaer, and Doaa H Taha. STUDYING THE STRUCTURAL, OPTICAL, CHEMICAL AND ELECTROCHEMICAL ETCHING CHANGES OF CR-39 FOR DOSEMETRIC APPLICATIONS. *Radiation Protection Dosimetry*, 177(3):272–279, apr 2017.
- [147] G Dlubek, D Kilburn, V Bondarenko, J Pionteck, R Krause-Rehberg, and MA Alam. Characterisation of free volume in amorphous materials by pals in relation to relaxation phenomena. *24th Arbeitskreistagung ‘Nichtkristalline Strukturen’ of DGK*, pages 203–210, 2003.
- [148] Shinian Cheng, Zaneta Wojnarowska, Małgorzata Musiał, Sławomir Kolodziej, Eric Drockenmuller, and Marian Paluch. Studies on ion dynamics of polymerized ionic liquids through the free volume theory. *Polymer*, 212:123286, jan 2021.
- [149] Paramjit Singh and Rajesh Kumar. Radiation physics and chemistry of polymeric materials. In *Radiation Effects in Polymeric Materials*, pages 35–68. Springer International Publishing, 2019.

- [150] Jyoti Sharma, Kshitij Tewari, and Raj Kumar Arya. Diffusion in polymeric systems—a review on free volume theory. *Progress in Organic Coatings*, 111:83–92, oct 2017.
- [151] Joanne Budzien, John D. McCoy, and Douglas B. Adolf. Solute mobility and packing fraction: A new look at the doolittle equation for the polymer glass transition. *The Journal of Chemical Physics*, 119(17):9269–9273, oct 2003.
- [152] D. Bamford, A. Reiche, G. Dlubek, F. Alloin, J.-Y. Sanchez, and M. A. Alam. Ionic conductivity, glass transition, and local free volume in poly(ethylene oxide) electrolytes: single and mixed ion conductors. *The Journal of Chemical Physics*, 118(20):9420–9432, may 2003.
- [153] Hiroshi Fujita. Notes on free volume theories. *Polymer Journal*, 23(12):1499–1506, dec 1991.
- [154] Robert Simha and Thomas Somcynsky. On the statistical thermodynamics of spherical and chain molecule fluids. *Macromolecules*, 2(4):342–350, jul 1969.
- [155] Victor Petrovich Shantarovich. Positron annihilation and permeation of amorphous polymers. *Journal of Membrane Science and Research*, 8(3), 2022.
- [156] Jingjing Kong, Junjie Liu, Peiyu Jia, Ning Qi, Zhiquan Chen, Shan Xu, and Nanwen Li. Synergistic effect of thermal crosslinking and thermal rearrangement on free volume and gas separation properties of 6fda based polyimide membranes studied by positron annihilation. *Journal of Membrane Science*, 645:120163, mar 2022.
- [157] Pranav Utpalla, S.K. Sharma, K. Sudarshan, M. Sahu, and P.K. Pujari. Investigation of the free volume characteristics of PEO based solid state polymer electrolyte by means of positron annihilation spectroscopy. *Solid State Ionics*, 339:114990, oct 2019.
- [158] F.A. Selim. Positron annihilation spectroscopy of defects in nuclear and irradiated materials- a review. *Materials Characterization*, 174:110952, apr 2021.
- [159] Tetsuya Hirade, Frans H.J. Maurer, and Morten Eldrup. Positronium formation at low temperatures: the role of trapped electrons. *Radiation Physics and Chemistry*, 58(5-6):465–471, jun 2000.

- [160] Z. Yu, U. Yahsi, J. D. McGervey, A. M. Jamieson, and R. Simha. Molecular weight-dependence of free volume in polystyrene studied by positron annihilation measurements. *Journal of Polymer Science Part B: Polymer Physics*, 32(16):2637–2644, dec 1994.
- [161] Anna Nyczyk-Malinowska, Ewa Dryzek, Magdalena Hasik, and Jerzy Dryzek. Various types of polysiloxanes studied by positron annihilation lifetime spectroscopy. *Journal of Molecular Structure*, 1065-1066:254–261, may 2014.
- [162] G. Dlubek and N. Meyendorf. Positron annihilation spectroscopy (PAS). In *Nondestructive Materials Characterization*, pages 374–411. Springer Berlin Heidelberg, 2004.
- [163] Günter Dlubek, Hellen M. Fretwell, and Norbert Meyendorf. Positron annihilation: A new method for studying subnanometer-size local free volumes in polymers. In *Metal Matrix Composites and Metallic Foams*, pages 241–246. Wiley-VCH Verlag GmbH & Co. KGaA, dec 2005.
- [164] G. Dlubek, J. Stejny, Th. Lüpke, D. Bamford, K. Petters, Ch. Hübner, M. A. Alam, and M. J. Hill. Free-volume variation in polyethylenes of different crystallinities: Positron lifetime, density, and x-ray studies. *Journal of Polymer Science Part B: Polymer Physics*, 40(1):65–81, nov 2001.
- [165] Z. Lounis-Mokrani, A. Guittoum, D. Imatoukene, M. Aitziane, A. Badreddine, and M. Mebhah. Characterisation of proton irradiated CR-39 detector using positron annihilation lifetime spectroscopy. *Radiation Measurements*, 50:26–30, mar 2013.
- [166] Rajesh Kumar, Santa Rajguru, D. Das, and Rajendra Prasad. SHI induced modification in CR-39 polycarbonate by positron annihilation lifetime studies. *Radiation Measurements*, 36(1-6):151–154, jun 2003.
- [167] Rajesh Kumar, S.A. Ali, A.K. Mahur, D. Das, A.H. Naqvi, H.S. Virk, and Rajendra Prasad. Free volume study of 70mev carbon induced modification in polymers through positron annihilation. *Nuclear Instruments and Methods in Physics Research Section B: Beam Interactions with Materials and Atoms*, 244(1):257–260, mar 2006.
- [168] Rajesh Kumar, Udayan De, P.M.G. Nambissan, M. Maitra, S. Asad Ali, T.R. Middy, S. Tarafdar, F. Singh, D.K. Avasthi, and Rajendra Prasad. Positron lifetime studies of

- the dose dependence of nanohole free volumes in ion-irradiated conducting poly-(ethylene-oxide)-salt polymers. *Nuclear Instruments and Methods in Physics Research Section B: Beam Interactions with Materials and Atoms*, 266(8):1783–1787, apr 2008.
- [169] Rajesh Kumar, Paramjit Singh, S. K. Gupta, R. Gupta, M. K. Jaiswal, M. Prasad, A. Roychowdhury, R. P. Chauhan, and D. Das. Radiation induced nano-scale free volume modifications in amorphous polymeric material: a study using positron annihilation lifetime spectroscopy. *Journal of Radioanalytical and Nuclear Chemistry*, 314(3):1659–1666, nov 2017.
- [170] H. Elazhar, A.C. Chami, M. Abdesselam, N. Arbor, D. Muller, A. Nasreddine, M. Roumie, Z. El Bitar, and A. Nourreddine. Light particle spectroscopy using CR-39 detectors: An experimental and simulation study. *Nuclear Instruments and Methods in Physics Research Section B: Beam Interactions with Materials and Atoms*, 448:52–56, jun 2019.
- [171] M.A. Al-Jubbori, M. Fromm, and E.M. Awad. Strong etching formulation (time and rate) for PADC with deep depth bulk etch rate study. *Nuclear Instruments and Methods in Physics Research Section A: Accelerators, Spectrometers, Detectors and Associated Equipment*, 1005:165402, jul 2021.
- [172] A.A. Azooz and M.A. Al-Jubbori. Interrelated temperature dependence of bulk etch rate and track length saturation time in CR-39 detector. *Nuclear Instruments and Methods in Physics Research Section B: Beam Interactions with Materials and Atoms*, 316:171–175, dec 2013.
- [173] Ayman M. Abdalla, Tayseer I. Al-Naggar, Rayah H. Alhandhal, and Hasan B. Albargi. Registration of alpha particles using CR-39 nuclear detector. *Nuclear Instruments and Methods in Physics Research Section A: Accelerators, Spectrometers, Detectors and Associated Equipment*, 1042:167419, nov 2022.
- [174] D. Nikezić. Three dimensional analytical determination of the track parameters. *Radiation Measurements*, 32(4):277 – 282, 2000.
- [175] D Nikezic and K.N Yu. Three-dimensional analytical determination of the track parameters: over-etched tracks. *Radiation Measurements*, 37(1):39 – 45, 2003.

- [176] D. Hermsdorf and M. Hunger. Determination of track etch rates from wall profiles of particle tracks etched in direct and reversed direction in PADC CR-39 SSNTDs. *Radiation Measurements*, 44(9-10):766–774, oct 2009.
- [177] Z. Lounis, S. Djeflal, K. Morsli, and M. Allab. Track etch parameters in CR-39 detectors for proton and alpha particles of different energies. *Nuclear Instruments and Methods in Physics Research Section B: Beam Interactions with Materials and Atoms*, 179(4):543–550, sep 2001.
- [178] Nada Farhan Kadhim, Ali A. Ridha, Manar Dheyaa Salim, M.Y. Hanfi, and Mostafa Y.A. Mostafa. Development of alpha tracks measurement with thermal oven as an etching technique for SSNTDs. *Materials Today: Proceedings*, 44:2903–2908, 2021.
- [179] HAS Aly. Alpha track shape analysis for different sources 239pu, 210po and 241am using cr-39 ssntd. *Life Science Journal*, 10(2), 2013.
- [180] M. F. Zaki and H El-Shaer. Particularization of alpha contamination using cr-39 track detectors. *Radiat. Effects Defects Solids*, 163(10):827 – 833, 2008.
- [181] M. El Ghazaly and Nabil M. Hassan. Characterization of saturation of CR-39 detector at high alpha-particle fluence. *Nuclear Engineering and Technology*, 50(3):432–438, apr 2018.
- [182] P. Mozzo, F. Trotti, A. Temporin, M. Lanciai, F. Predicatori, F. Righetti, and A. Tacconi. -spectroscopy on cr-39 track detectors for the dosimetry of radon daughters. *Environment International*, 22:595 – 600, 1996. The Natural Radiation Environment VI.
- [183] Mahasin Gazi, Saheli Chowdhury, Arindam Kumar Naskar, Argha Deb, and Dipak Ghosh. Alpha radioactivity in human blood and its possible correlation to ailment pattern. *Journal of Radioanalytical and Nuclear Chemistry*, 331(3):1225–1236, feb 2022.
- [184] J.M. Stajic, V.M. Markovic, B. Milenkovic, N. Stevanovic, and D. Nikezic. Distribution of alpha particle tracks on CR-39 detector in radon diffusion chamber. *Radiation Physics and Chemistry*, 181:109340, apr 2021.
- [185] Abdalsattar Kareem Hashim, Abbas R. Hatif, Naser M. Ahmed, I.A. Wadi, and Amer A. Al Qaaod. Comparison study of CR-39 and CN-85 detectors to evaluate the alpha ra-

- dioactivity of some samples of drinks in iraq. *Applied Radiation and Isotopes*, 167:109410, jan 2021.
- [186] J Kansy and D Giebel. Study of defect structure with new software for numerical analysis of PAL spectra. *Journal of Physics: Conference Series*, 265:012030, jan 2011.
- [187] C. A. Furtado, G. Goulart Silva, J. C. Machado, M. A. Pimenta, and R. A. Silva. Study of correlations between microstructure and conductivity in a thermoplastic polyurethane electrolyte. *The Journal of Physical Chemistry B*, 103(34):7102–7110, aug 1999.
- [188] Izabela Irska, Sandra Paszkiewicz, Daria Pawlikowska, Jerzy Dryzek, Amelia Linares, Aurora Nogales, Tiberio A. Ezquerro, and Elżbieta Piesowicz. Relaxation behaviour and free volume of bio-based poly(trimethylene terephthalate)-block-poly(caprolactone) copolymers as revealed by broadband dielectric and positron annihilation lifetime spectroscopies. *Polymer*, 229:123949, aug 2021.
- [189] M. Eldrup, D. Lightbody, and J.N. Sherwood. The temperature dependence of positron lifetimes in solid pivalic acid. *Chemical Physics*, 63(1-2):51–58, dec 1981.
- [190] J. Bohlen, J. Wolff, and R. Kirchheim. Determination of free-volume and hole number density in polycarbonates by positron lifetime spectroscopy. *Macromolecules*, 32(11):3766–3773, 1999.
- [191] M.P.R. Waligórski, R.N. Hamm, and R. Katz. The radial distribution of dose around the path of a heavy ion in liquid water. *International Journal of Radiation Applications and Instrumentation. Part D. Nuclear Tracks and Radiation Measurements*, 11(6):309–319, jan 1986.
- [192] J.L. Wormald and A.I. Hawari. Modeling fission spikes in nuclear fuel using a multigroup model of electronic energy transport. *Journal of Nuclear Materials*, 566:153797, aug 2022.
- [193] Gavin Gillmore, David Wertheim, and Simon Crust. Effects of etching time on alpha tracks in solid state nuclear track detectors. *Science of The Total Environment*, 575:905–909, jan 2017.

Appendix: Publication and communication

Publication

- S. Limam A. Guittoum Z. Lounis-Mokrani M. Hemous, N. Bendjedda. Studying Alpha Irradiated CR39 Using Positron Annihilation Spectroscopy. (2023). Acta Physica Polonica A ISSN 1898-794X , 144(3), 163. <https://doi.org/10.12693/APhysPolA.144.163>

Communications

- S. Limam, A. Guittoum , Z. Mokrani, M. Izzerouken, U. Yahsi. N. Bendjedda , Positron annihilation spectroscopy in CR39 irradiated with alpha particles, IMRR2019 (16-18/12/2019) CRND, Algiers
- S. Limam, A. Guittoum ,R. Krause-Rehberg. Z. Mokrani, M. Izzerouken, U. Yahsi. , Positron annihilation lifetime spectroscopy in neutrons irradiated CR39 polymer, IC-CAP2021 (26-28/09//2021), Blida university
- S. Limam, A. Guittoum , Z. Mokrani, M. Hemous, , Positron annihilation spectroscopy in alpha irradiated CR39, ICRAA'3, CRNA- Algiers (11/2022)